TUDelft

Delft University of Technology

Interacting light fields in monolayer ws2 and plasmonic systems

Noordam, M.L.

DOI
10.4233/uuid:e6aed08e-2388-413a-9f90-8d94fedd5225

Publication date
2023

Document Version
Final published version

Important note
To cite this publication, please use the final published version (if applicable).
Please check the document version above.

INTERACTING LIGHT FIELDS IN MONOLAYER WS$_2$ AND PLASMONIC SYSTEMS

INTERACTING LIGHT FIELDS IN MONOLAYER WS$_2$ AND PLASMONIC SYSTEMS

Proefschrift

ter verkrijging van de graad van doctor
aan de Technische Universiteit Delft,
op gezag van de Rector Magnificus prof. dr. ir. T.H.J.J. van der Hagen,
voorzitter van het College voor Promoties,
in het openbaar te verdedigen op woensdag 26 april 2023 om 10:00 uur

door

Marcus Lambertus NOORDAM

Master of Science in Applied Physics,
Technische Universiteit Delft, Nederland
geboren te Amsterdam, Nederland.

Dit proefschrift is goedgekeurd door de

  promotor: Prof. dr. L. Kuipers
  promotor: Prof. dr. ir. H.S.J. van der Zant

Samenstelling promotiecommissie:

Rector Magnificus,	voorzitter
Prof. dr. L. Kuipers,	Technische Universiteit Delft, promotor
Prof. dr. ir. H.S.J. van der Zant,	Technische Universiteit Delft, promotor

Onafhankelijke leden:

Prof. dr. P.G. Steeneken,	Technische Universiteit Delft
Dr. S.C. Conesa Boj,	Technische Universiteit Delft
Prof. dr. L.D.A. Siebbeles,	Technische Universiteit Delft
Prof. dr. R. Grange,	ETH Zurich, Switzerland
Dr. P. Kraus	ARCNL, Amsterdam

To all my teachers

CONTENTS

SUMMARY

In this thesis, we explore the interaction between multiple optical light fields. Although these light fields can interfere with each other in a vacuum, actual interaction can only occur in a medium. This interaction can be amplified in materials with nanoscale dimensions such as a monolayer of WS_2 and metallic nanostructures. The shapes of these materials have characteristic length scales smaller than the wavelength of light and influence the interaction between light and matter. There are three main reasons why studying light field interactions in nanoscale materials is interesting. First, by investigating the interaction between different light waves we have a tool to probe the light behavior in, e.g., a monolayer WS_2 or metallic nanostructures. Secondly, by studying the interaction of multiple light waves we can probe the characteristics of the light waves themselves. Finally, the interaction of light waves can be utilized in novel applications such as frequency conversion and photonic nanocircuitry. This thesis is divided into four parts which will be discussed in the following sections.

The first part of this thesis introduces the relevant scientific theory and experimental methods. We start in **chapter 1** by introducing three key concepts relevant to understanding the experiments described in this thesis: surface plasmon polaritons (SPPs), nonlinear optics, and transition metal dichalcogenides materials. Surface plasmon polaritons are a specific type of electromagnetic wave that exits at the interface between a metallic surface and a dielectric. These waves can propagate along the surface of a metallic nanostructure and strongly enhance the electrical near field around the interface. The field enhancement of SPPs can be used to amplify nonlinear optical phenomena which originate from strong light fields that interact with themselves and/or with other light waves. The interaction between light fields may lead to the generation of light with different frequencies than those of the fundamental fields. TMDC materials, including WS_2, are semiconductor crystals in which the stacked unit cell layers are loosely connected by van der Waals forces. Using exfoliation techniques these materials can be thinned down to flakes with a thickness of only one atomic unit cell consisting of three atoms, called monolayers. Despite their atomic thickness these monolayers exhibit strong light-matter interaction and show fascinating optical behavior.

The two experimental setups used in this thesis are described in **chapter 2**, together with a description of the sample fabrication techniques. In the first experimental setup, we use a nonlinear spectroscopy microscope in which we illuminate the nanostructures with two intense ultrashort laser pulses of different frequencies. One laser pulse has a free-space central wavelength of around 1200 nm and the other laser pulse of around 775 nm. The generated nonlinear signals are filtered from the reflected light and measured using a spectrometer. The second experimental setup is a near-field microscope. Here, we map the electric near-field of plasmonic waves by collecting the light waves with an aperture-based probe brought in close proximity to the metallic surface.

The second part of this thesis includes a discussion of two experiments on the in-

teraction of ultrashort laser pulses in a monolayer of WS_2. In **chapter 3** we study the optical response of a monolayer WS_2 upon excitation with two ultrashort laser pulses with different frequencies. Not only do we observe multiple (non)degenerate nonlinear signals, but we also distinguish a photoluminescence signal generated in the monolayer of WS_2. The photoluminescence signal originates from the radiative decay of bound electron-hole pairs in monolayer WS_2, called excitons. Because the photon energies of the fundamental laser pulses are smaller than the bandgap energy, the excitons are solely excited by nonlinear processes. We observe photoluminescence generated from degenerated as well as nondegenerate nonlinear processes and study the power dependency of the different nonlinear processes.

In **chapter 4** we characterize two ultrashort light pulses with different frequencies by using their mutual nondegenerate nonlinear interaction in a monolayer WS_2. By recording the nonlinear spectra as a function of an induced time delay between the laser pulses, we are able to extract the frequency-resolved optical gating (FROG) traces of the four-wave mixing (FWM) and sum-frequency generation (SFG) nonlinear processes. From these FROG traces we calculate the intensity and phase profiles of both ultrashort pulses.

The third part of this thesis presents investigations of light interaction in metallic nanostructures that show plasmonic behavior. In **chapter 5** we design a plasmonic grating in a thin gold layer to amplify the nondegenerate FWM signal. By combining two grating structures that are resonant to the different fundamental frequencies of the two ultrashort laser pulses we can amplify the FWM signal by more than 3 orders of magnitude compared to a plane gold film.

In **chapter 6** we study plasmonic propagating modes in metallic two-wire transmission line (TWTL) systems. The basis for these systems is formed by two parallel thin metallic wires close together and exhibits two plasmonic eigenmodes: a symmetric mode and an anti-symmetric mode. By selectively exciting the two modes using orthogonally polarized continuous wave laser light at the telecom frequency (1550 nm) we experimentally map the near-field of the modes with a near-field microscope. We can identify the spatial profiles and symmetries of the two plasmonic modes. Furthermore, we study the plasmonic propagation through system elements such as an antenna, a mode filter, and a mode shifter design.

Finally, in the fourth part of this thesis, we present concluding thoughts together with an outlook towards new research directions and applications in **chapter 7**.

SAMENVATTING

In dit proefschrift onderzoeken we de interactie tussen meerdere optische lichtvelden. Hoewel deze lichtvelden in een vacuüm met elkaar kunnen interfereren, kan daadwerkelijke interactie alleen in een medium plaatsvinden. Deze interactie kan worden versterkt in materialen met afmetingen op nanoschaal, zoals een monolaag van WS_2 en metalen nanostructuren. De vormen van deze materialen hebben karakteristieke lengteschalen die kleiner zijn dan de golflengte van licht en beïnvloeden de interactie tussen licht en materie. Er zijn drie belangrijke redenen waarom het bestuderen van lichtveldinteracties in materialen op nanoschaal interessant is. Ten eerste hebben we door de interactie tussen verschillende lichtgolven te bestuderen een hulpmiddel om het lichtgedrag in bijvoorbeeld een monolaag van WS2 of metalen nanostructuren te onderzoeken. Ten tweede kunnen we door de interactie van meerdere lichtgolven te bestuderen de kenmerken van de lichtgolven zelf onderzoeken. Ten slotte kan de interactie van lichtgolven worden gebruikt in nieuwe toepassingen zoals frequentieconversie en fotonische nanoschakelingen. Dit proefschrift is opgedeeld in vier delen die in de volgende paragrafen worden besproken.

Het eerste deel van dit proefschrift introduceert de relevante wetenschappelijke theorie en experimentele methoden. We beginnen in **hoofdstuk 1** met de introductie van drie belangrijke concepten die relevant zijn voor het begrijpen van de experimenten die worden beschreven in dit proefschrift: oppervlakte-plasmonpolaritonen (SPP's), niet-lineaire optica en overgangsmetaal dichalcogenides (TMDC) materialen. Een oppervlakte plasmonpolariton is een specifiek type elektromagnetische golf die bestaat op het grensvlak tussen een metalen oppervlak en een diëlektricum. Deze golven kunnen zich voortbewegen langs het oppervlak van een metalen nanostructuur en het elektrische nabije veld rond het oppervlak versterken. De veldversterking van oppervlakte-plasmon polaritonen kan worden gebruikt om niet-lineaire optische signalen te vergroten die voortkomen uit lichtvelden die interageren met zichzelf en/of met andere lichtgolven. De interactie tussen lichtvelden kan leiden tot het genereren van licht met andere frequenties dan die van de fundamentele velden. TMDC materialen, waaronder WS_2, zijn halfgeleiderkristallen waarin de gestapelde eenheidscellagen losjes zijn verbonden door van der Waals krachten. Met behulp van exfoliatietechnieken kunnen deze materialen worden verdund tot laagjes met een dikte van één eenheidscel bestaande uit drie atomen, monolagen genoemd. Ondanks hun atomaire dikte vertonen deze monolagen een sterke interactie tussen licht en materie en vertonen ze fascinerend optisch gedrag.

De twee experimentele opstellingen die in dit proefschrift worden gebruikt, worden beschreven in **hoofdstuk 2**, samen met een beschrijving van de technieken voor de fabricage van de nanostructuren. In de eerste experimentele opstelling gebruiken we een niet-lineaire spectroscopie microscoop waarin we de nanostructuren belichten met twee intense ultrakorte laserpulsen van verschillende frequenties. De eerste laserpuls heeft een centrale golflengte in de vrije ruimte van ongeveer 1200 nm en de tweede

laserpuls van ongeveer 775 nm in de vrije ruimte. De gegenereerde niet-lineaire signalen worden uit het gereflecteerde licht gefilterd en gemeten met een spectrometer. De tweede experimentele opstelling is een nabije-veld microscoop. Hier brengen we het elektrische nabije veld van plasmonische golven in kaart door de licht op te vangen met een optische sonde die in de nabijheid van het metalen oppervlak wordt gebracht.

Het tweede deel van dit proefschrift omvat een bespreking van twee experimenten over de interactie van ultrakorte laserpulsen in een monolaag van WS_2. In **hoofdstuk 3** bestuderen we de optische respons van een monolaag van WS_2 na excitatie met twee ultrakorte laserpulsen met verschillende frequenties. We nemen niet alleen meerdere (niet) ontaarde niet-lineaire signalen waar, maar we onderscheiden ook een fotoluminescentie gegenereerd in de monolaag van WS_2. De fotoluminescentie is afkomstig van emissie bij het verval van excitonen. Excitonen zijn gebonden paren van elektronen en elektrongaten in een monolaag van WS_2. De fotonenenergieën van de fundamentele laserpulsen zijn kleiner dan de bandgap-energie waardoor de excitonen uitsluitend opgewekt kunnen worden door niet-lineaire optische processen. We observeren fotoluminescentie gegenereerd door zowel ontaarde als niet-ontaarde niet-lineaire processen en bestuderen de vermogensafhankelijkheid van de verschillende niet-lineaire processen.

In **hoofdstuk 4** karakteriseren we twee ultrakorte lichtpulsen met verschillende frequenties door gebruik te maken van hun wederzijdse niet-ontaarde niet-lineaire interacties in een monolaag van WS_2. Door niet-lineaire spectra te meten als een functie van een geïnduceerde vertraging tussen de laserpulsen, zijn we in staat om de frequency-resolved optical gating (FROG) sporen van vier-golfmenging (FWM) en som-frequentie generatie (SFG) te extraheren. Uit deze FROG-sporen berekenen we de intensiteits- en faseprofielen van beide ultrakorte pulsen.

Het derde deel van dit proefschrift presenteert onderzoek naar lichtinteractie in metalen nanostructuren die plasmonisch gedrag vertonen. In **hoofdstuk 5** ontwerpen we een plasmonen tralie in een dunne goudlaag om het niet-ontaarde FWM-signaal te versterken. Door twee traliestructuren te combineren die resoneren met de verschillende fundamentele frequenties van de twee ultrakorte laserpulsen, kunnen we het FWM-signaal met meer dan 3 ordes van grootte versterken in vergelijking met een vlakke goudfilm.

In **hoofdstuk 6** bestuderen we plasmonische toestanden in metalen tweedraads transmissielijnsystemen (TWTL). De basis voor deze systemen wordt gevormd door twee parallelle dunne metalen draden dicht bij elkaar. Dit systeem vertoont twee plasmonische toestanden: een symmetrische toestand en een antisymmetrische toestand. In dit onderzoek exciteren we selectief twee plasmonische modi behulp van orthogonaal gepolariseerd continu laserlicht met telecomfrequentie (1550 nm). Vervolgens brengen we experimenteel het nabije veld van de plasmonische toestanden in kaart met een nabije-veld microscoop. Zo kunnen we de ruimtelijke profielen en symmetrie van de twee plasmonische toestanden identificeren. Verder bestuderen we de plasmonische voortbeweging door systeemelementen zoals een antenne, een toestandsfilter en een ontwerp van een toestandswisselaar.

Tot slot presenteren we in het vierde deel van dit proefschrift samen met de conclusies een vooruitblik op nieuwe onderzoeksrichtingen en toepassingen in **hoofdstuk 8**.

I

INTRODUCTION AND EXPERIMENTAL

1

INTRODUCTION

The interaction between light and matter at the nanoscale is a truly fascinating topic. Fabricating structures with nanoscale dimensions can dramatically change light-matter interactions of these structures due to the due to the finite wavelength of visible light waves. The study of light-matter interaction at the nanoscale is often referred to as nano-optics. The nano-optics experiments explored in this thesis are related to three key concepts: plasmonics, nonlinear surface optics, and transition metal dichalcogenide materials. Here, we will discuss each topic in detail to give a framework for the rest of this thesis.

1

1.1. LIGHT AND MATTER AT THE NANOSCALE

Humans have been fascinated by the interaction between light and matter for centuries. Among the many expressions of this fascination are the story of the burning-glass technology designed by Archimedes where an array of mirrors can be used to burn wooden ships and the lightsaber, a fictional device appearing in Star Wars with a light-matter interaction so strong it can be used in sword fighting combat. The painting "Three Spheres II" by M. C. Escher is another famous, but less violent, example. In this work of art, Escher sketched three spheres made of transparent material, reflecting material, and diffusive material. This painting magnificently illustrates the remarkable interactions that can occur between light and matter. Even though these spheres can have exactly the same shape, size, and weight they demonstrate a completely different relationship with light. At first sight, it might seem that Escher's work gives a complete demonstration of every form of light-matter interaction. Yet, there is a collection of other light-matter interactions that appear at the nanoscale. The study of light-matter interactions at the nanoscale is often referred to as nano optics.

To understand why light behaves differently at the nanoscale, we need to use the fact that light is an electromagnetic wave oscillating in space and time with a certain frequency and wavelength. Now for light in the visible spectrum, its wavelength ranges from 400 nm to 700 nm. If light interacts with matter that is structured in dimensions that are smaller or comparable to its wavelength it can exhibit counter-intuitive behavior. A real-world example of nano-optical light matter interaction can be observed from another sphere namely a soap bubble. Although a soap bubble consists mostly of air and water, it can reflect light with a color gradient pattern. This phenomenon is clearly distinct from the three spheres of Escher and is caused by the small thickness of the soap bubble. The soap bubble illustrates that materials with a simple light behavior in their bulk form can demonstrate a completely different behavior if they are shaped in smaller dimensions.

Another example of nano optics appears when we scale down a metallic sphere to nanoscale dimensions. Where a normal metallic sphere acts as a mirror, metallic nanoparticles with a diameter of approximately 50 nm can experience a plasmonic resonance. This resonance causes the nanoparticle to scatter one particular color depending on the size of the nanoparticles. This nanoscale behavior is used to give stained glass its beautiful colors.

The study of the behavior of light in bulk materials has already led to an enormous amount of technological inventions, ranging from eyeglasses to telescopes. The study of the behavior of light with materials shaped in nanoscale dimensions, often called nano optics, opens up new possibilities to a second wave of technological advancements. In this thesis, we study different nano-optical phenomena using materials with nanoscale dimensions. The results of the experiments can be best understood using three key concepts in nano optics: plasmonics, surface nonlinear optics, and the optical properties of the two-dimensional transition metal dichalcogenides (TMDC) materials.

In the remainder of this chapter, we individually introduce these three key concepts in sections 1.2 (plasmonics), 1.3 (surface nonlinear optics), and 1.4 (TMDC materials). In section 1.5 we give an outline of the thesis and link the key concepts to the individual chapters.

1.2. SURFACE PLASMON POLARITONS

Surface plasmon polaritons (SPPs) are surface waves propagating along a metal-dielectric interface, where the charge density oscillations in the metal are connected to the light mode in the dielectric. Plasmonic modes only exits at optical and infrared frequencies due to the requirement of a large real negative dielectric constant in the metal. SPPs are confined to the metal-dielectric interface, meaning that the electric field exponentially decays in the direction perpendicular to the interface. The strong electric field confinement near the interface makes SPPs an interesting topic in different scientific fields including bio-imaging [1], nonlinear optics, [2] and plasmonic nanocircuitry [3]. In chapter 5 we use plasmonics to enhance nonlinear optical effects and in chapter 6 we investigate plasmonic modes in a two-wire system using a near-field optical microscope.

In this section, we give a brief overview of the derivation of plasmonic modes from Maxwell's equation, for a complete overview of this derivation see for example the work by Novotny and Hecht [4]. Next, we discuss the plasmonic properties at a gold-air and gold-glass interface followed by a discussion on the coupling from free-space light and plasmonic waveguide structures.

1.2.1. BOUNDARY SOLUTION OF MAXWELL'S EQUATION

SPPs can be derived as eigenmode solutions from Maxwell's equations at the boundary between a metallic and a dielectric material with complex dielectric constants ϵ_m and ϵ_d, respectively. Figure 1.1 illustrates a plasmonic mode at a metal-dielectric interface defined along the z-direction where the plasmon propagates along the y-direction. At the boundary, the wavevector in the y-direction needs to be conserved leading to:

$$k_y^2 + k_{m,z}^2 = \epsilon_m k^2, \quad \text{and} \quad k_y^2 + k_{d,z}^2 = \epsilon_d k^2. \tag{1.1}$$

Here the total wavevector is $k^2 = \frac{\omega^2}{c^2}$. Secondly, requiring the continuity of the electric field and the fact that both sides are free of sources, leads to

$$\epsilon_m k_{d,z} = \epsilon_d k_{m,z}. \tag{1.2}$$

Combining eq. 1.1 and eq. 1.2 gives:

$$k_y^2 = \frac{\epsilon_m \epsilon_d}{\epsilon_m + \epsilon_d} k^2, \tag{1.3}$$

$$k_{m,z}^2 = \frac{\epsilon_m^2}{\epsilon_m + \epsilon_d} k^2 \quad \text{and} \quad k_{d,z}^2 = \frac{\epsilon_d^2}{\epsilon_m + \epsilon_d} k^2. \tag{1.4}$$

A bound plasmonic mode propagating in the y-direction requires a real k_y value and a purely imaginary k_z. From eq. 1.3 and eq. 1.4 follows that this is the case for a positive real value of ϵ_d and a negative real value of ϵ_m with an absolute value is larger than ϵ_d.

A negative real value of ϵ_m means that the free electrons in the metal oscillate out of phase with the incoming electric field. This behavior is predicted at visible and infrared frequencies for most metals by the Drude model that can estimate the complex ϵ from a plasma frequency of the metal. Gold and silver experience a particularly high negative

1

Re(ϵ) and together with the fact that their $|\text{Im}(\epsilon)|$ is much smaller than the $|\text{Re}(\epsilon)|$ makes them the most commonly used metals for plasmonic experiments.

The plasmonic experiments in this thesis are performed using air and glass as dielectric materials. We use gold as the metallic material in this thesis because it can be relatively easily structured using nanofabrication processes together with the fact that it does not experience metal oxidation.
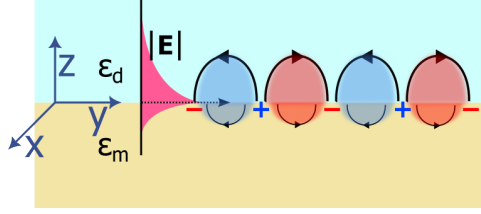

Figure 1.1: Illustration of a plasmonic mode on the boundary between a metal and a dielectric material with dielectric constants ϵ_m and ϵ_d respectively. The interface is defined in the z-direction and the plasmon propagates in the y-direction. The plus and minus signs indicate the local charge density in the metal and the curved arrows indicate the direction of the local electric field. The pink exponential curves illustrate the exponential decay of the amplitude of the electric field along the z-direction with a peak intensity at the interface.

1.2.2. PLASMONIC PROPERTIES

The SPP modes can have different characteristics, depending on the materials of the interface and the frequency of the SPP. From the complex wavevector derived in eq. 1.3 and eq. 1.4 we can calculate different plasmonic proprieties. For these calculations, we use the complex dielectric constants of gold from Johnson et al. [5], air (n=1), and glass (n=1.5). In fig. 1.2 the calculated plasmonic properties are plotted as a function of the free-space wavelength in a vacuum. The effective plasmonic wavelength, $\lambda_\text{eff} = \frac{2\pi}{\text{Re}(k_y)}$ is plotted in fig.1.2(a) for a plasmon at a gold/air and a gold/glass interface. We also draw the light line of free-space light propagating in air and glass with straight dashed lines. From fig.1.2 it can be observed that λ_eff is smaller than the wavelength of free-space light propagating in the dielectric material. This corresponds to a higher plasmonic wavevector, indicating a confined plasmonic mode over the whole frequency range. The discrepancy between λ_eff and the light lines becomes larger for smaller free-space wavelengths until roughly 500 nm where the interband transitions in the gold appear and $|\text{Im}(\epsilon_\text{m})|$ becomes comparable to $|\text{Re}(\epsilon_\text{m})|$.

In fig. 1.2(b) the 1/e propagation lengths of the plasmonic intensity, $\frac{1}{2\text{Im}(k_y)}$, are plotted for both interfaces. This plot shows that the propagation length strongly decreases for lower frequencies. The propagation length drops down from 320(93) um at the air(glass) interface at a free-space wavelength of 1610 nm to 7.1(1.7) um at 617 nm, which is only a few oscillations. The very short propagating length at visible frequencies is a strong limitation for the design of plasmonic devices and experiments.

The mode intensity decay lengths in the z-direction, $\frac{1}{2\text{Im}(k_z)}$, are plotted in fig. 1.2(c). From we plot the decay length of the electric field into the gold as well as the decay length into the glass and air. From fig. 1.2(c) it can be observed that the plasmonic mode intensity penetrates much more into the dielectric materials than into the gold. For higher

free-space wavelengths the plasmonic mode intensity is mostly located in the dielectric
with decay lengths of more than a micrometer. At lower free-space wavelengths, the de-
cay length into the dielectrics decreases and becomes comparable with the decay length
into the gold which slightly increases for shorter wavelengths.
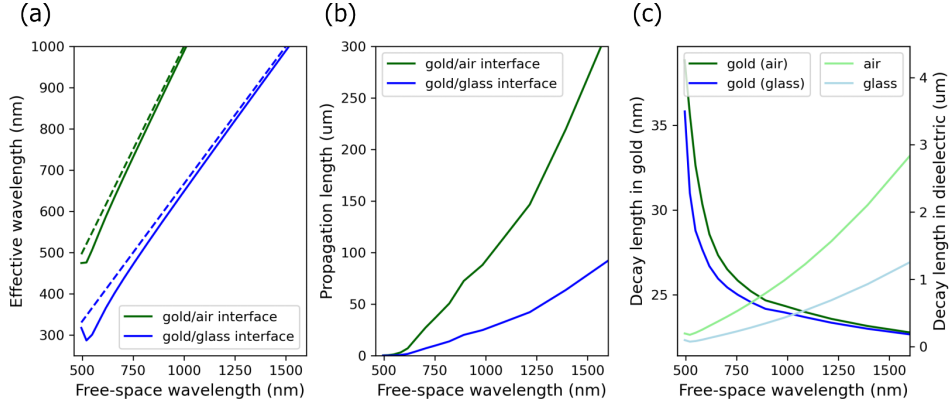
Figure 1.2: Plasmonic properties as a function of the free-space wavelength in vacuum. (a) The plasmonic
effective wavelength is plotted for the gold/air interface (green) and the gold/glass interface (blue). The light
lines of air (green) and glass (blue) are plotted as dashed lines. (b) Propagation lengths in the y-direction for
the gold/air interface in green and the gold/glass interface in blue. (c) Decay lengths of the electric field in the
z-direction from the interface into the gold and dielectric materials. The decay lengths into the gold are plotted
on the left y-axis in green for the gold/air interface and in blue for the gold/glass interface. The decay lengths
into the dielectrics are plotted on the right y-axis in light green for air and in light blue for glass.

1.2.3. COUPLING

The plasmonic mode is confined to the metal/dielectric interface and free-space light
can not directly couple to plasmons. Therefore, a few examples of plasmonic effects can
be found in everyday life. However, using nanoscale engineering it is possible to couple
free-space light modes into plasmonic modes. The two main approaches to couple to
plasmons use either nanoscale layer or nanoscale metallic structuring.

First, we discuss two similar coupling techniques using nanoscale layers, called the
Otto [6] and Kretschmann [7] configuration. Both techniques rely on the coupling to a
plasmonic mode via the evanescent field from a light wave in another dielectric that has
a higher refractive index than the dielectric of the plasmon interface. In the Otto con-
figuration the evanescent field at the interface between two dielectrics couples through
a thin layer of dielectric, e.g. air, to a plasmon at the metal-dielectric interface. In the
Kretschmann configuration the field couples from a metal-dielectric interface through
a thin layer of metal to a plasmon at the other side of the metal at the metal-dielectric
interface.

Recent advances in nanofabrication techniques have made it possible to couple to
plasmon modes using nanoscale metallic structuring. The first coupling mechanism we
use in this thesis (chapter 5) involves a metallic grating structure with nanoscale dimen-
sions. With this technique the wavevector mismatch is solved by adding a reciprocal

1

lattice vector to the y-component of the free-space wavevector following:

$$k_{\text{SPP}} = k_0 \sin(\theta) + \frac{m * 2\pi}{\Lambda_g}.$$ (1.5)

Here $k_0 \sin(\theta)$ is the y-component of the free-space wavevector with θ as the angle of the incident beam. m is an integer and Λ_g is the grating period. If the angle of the incident beam matches the correct grating period, plasmons get excited across the grating interface.

Finally, we discuss the optical antenna used in chapter 6. Similar to radio frequency (RF) antennas, optical antennas use sub-wavelength structures with resonant behavior to transform free-space light waves into strongly localized fields. These localized modes can subsequently couple to propagating plasmonic waveguide modes. But although their function is similar to RF antennas, optical antennas follow different design principles because the dimensions of the metal approach the electronic penetration depth. Furthermore, plasmonic modes that only exist at optical and infrared frequencies have to be taken into account [8]. Although there are many different types of optical antennas, often studied designs are dimer particles and bowtie-shaped antennas where the electric near-field is localized in between two metal elements. In chapter 6 we use a split ring antenna to couple focused laser light into propagating plasmonic modes.

1.2.4. PLASMONIC WAVEGUIDE STRUCTURES

So far we discussed plasmons propagating at a plane surface, but in the next section we turn our attention to plasmonic waveguide systems. Plasmonic waveguides are restricted in the x and z directions perpendicular to the propagation direction. These plasmonic waveguides can be used to guide plasmonic waves confined in sub-diffraction-limited dimensions.

Here, we discuss three types of plasmonic waveguides made from gold on a glass surface: a single nanowire, a two-wire transmission line (TWTL), and a slot waveguide, schematically depicted in fig. 1.3(a-c). These structures can be made using nanofabrication techniques such as ion-beam etching or e-beam lithography processes, see also section 2.2.2. The plasmonic waveguides can support plasmonic modes that depend on geometrical parameters such as the height of the metal, h, the width of the nanowire, w, and the gap between wires, g, as well as on the complex dielectric constants of the glass, air, and metal. In fig. 1.3(d-f) we display the local electric field of the simulated eigenmodes of the three plasmonic waveguides using a commercially available eigenmode solver (Lumerical MODE). In this simulation, we use $h = 50$ nm and $w = g = 100$ nm. Furthermore, for gold we use the complex dielectric constant from Palik [9] and we use a refractive index of 1 and 1.5 for air and glass, respectively.

The single nanowire waveguide only supports one plasmonic mode, similar to the radial polarized Sommerfeld mode in a round nanowire [10]. The local electric field of the plasmonic mode in the single nanowire is plotted in fig.1.3(d). It can be observed that the x-component of the electric field is mostly located at the sides of the nanowire while the z-component is mostly located at the top and bottom of the nanowire.

For the TWTL, the eigenmodes of the single nanowires hybridize and two new plasmonic modes can be found. They are often called the symmetric and anti-symmetric

modes regarding the symmetry of the local charge distribution in the wires [11–14]. In fig.1.3(e) we plot the local electric field of the anti-symmetric mode. Here, it can be observed that the field is mostly located in between the nanowires where the x-component of the field is still mostly located at the sides and the z-component at the top and bottom of the wires. Furthermore, the real part of the electric field is symmetric for the x-component of the electric field while it is anti-symmetric for the y- and z-component. In chapter 6 we will discuss the symmetric and anti-symmetric modes of the TWTL system in more detail.

Finally, for the slot waveguide there exits also a symmetric and anti-symmetric mode and we display the field of the anti-symmetric mode in fig.1.3(f). This mode experiences similar field symmetries and intensity patterns as the anti-symmetric mode of the TWTL system, see also [15, 16].
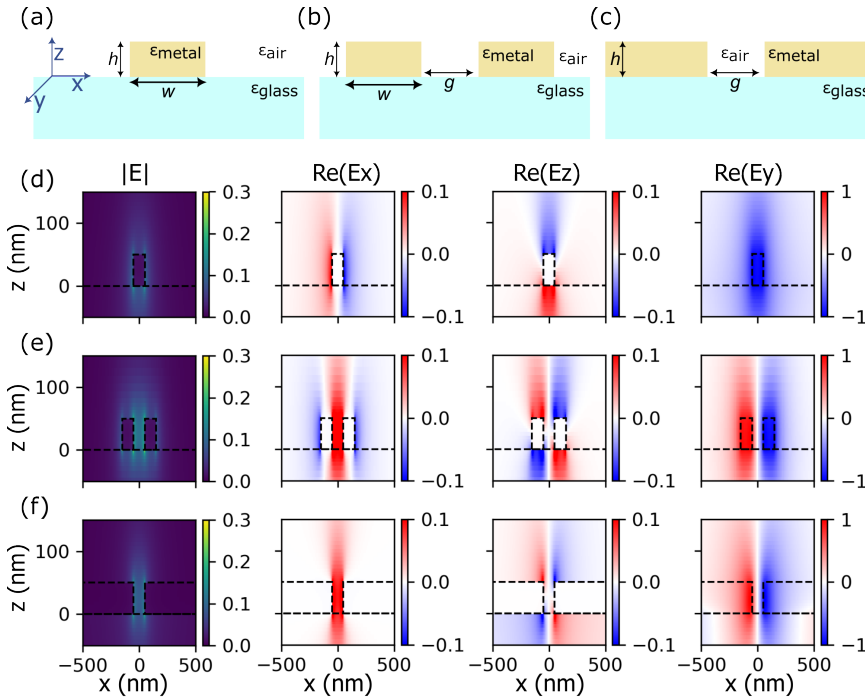
Figure 1.3: Eigenmode simulations of three types of plasmonic waveguides made from gold. (a-c) Schematic illustrations of the single nanowire waveguide (a), two-wire transmission line (b), and slot waveguide (c). The waveguides are characterized by the geometrical parameters: the height of the metal, h, the width of the nanowire, w, and the gap between wires, g. (d-f) Total absolute value and real parts of the x-,y- and z-component of the local electric field of the simulated eigenmodes of the single nanowire (d), the anti-symmetric mode of the two-wire transition line (e), and the anti-symmetric mode of the slot waveguide (f) normalized by the maximum value of the individual components. A free-space wavelength of 1550 nm is used together with the geometric parameters: h = 50 nm, w = 100 nm, and g = 100 nm. The outline of the metallic structure and the glass is marked by a black dotted line.

1

1.3. NONLINEAR OPTICS

The first nonlinear optical parametric process was experimentally demonstrated in 1961 [17] shortly after the invention of the first operating laser in 1960 [18]. The experimental realization of a light source producing high intensities of coherent light made it possible to experimentally study nonlinear optical phenomena. Since the first observation of nonlinear signals, there has been a lot of scientific progress in the understanding of nonlinear phenomena [19]. This resulted in many applications from frequency conversion applications, further described in chapter 5, to ultrashort pulse characterization see chapter 4. In the remainder of this section we give an introduction to nonlinear optics as the basis for chapters 3, 4 and 5. We start with a brief overview of how nonlinear optics appear in Maxwell's equation, then we discuss the different nonlinear processes explored in this thesis and finally we discuss nonlinear surface optics.

1.3.1. HIGHER-ORDER TERMS IN MAXWELL'S EQUATIONS

Like the linear behavior of light-matter interaction, also nonlinear processes can be well described by Maxwell's equations. When an electric field $\mathbf{E}$ propagates through a medium it generates macroscopic bound charges in the material that leads to a field displacement generated by the initial electric field. The total field displacement can be defined as:

$$\mathbf{D} \equiv \epsilon_0 \mathbf{E} + \mathbf{P}. \tag{1.6}$$

Here, ϵ_0 is the vacuum permittivity and $\mathbf{P}$ is the macroscopic polarization density. The macroscopic polarization response of a medium, $\mathbf{P}$, can be given by a Taylor approximation in terms of $\mathbf{E}$,

$$\mathbf{P} = \epsilon_0 \left[\chi^{(1)} \mathbf{E} + \chi^{(2)} \mathbf{EE} + \chi^{(3)} \mathbf{EEE} + ... \right], \tag{1.7}$$

where $\chi^{(m)}$ is the mth-order susceptibility, which is a tensor of rank m+1. The first term in equation 1.7 expresses the linear response of the electric field which describes for example the reflection and transmission of light interacting with a medium. The higher-order terms describe the nonlinear response of the field in a medium. They account for a variety of different nonlinear optical processes causing frequency conversion of the initial electric field [19, 20]. The nonlinear processes can be separated into parametric and non-parametric processes, where for the parametric processes the total energy does not change while for the non-parametric processes there is a net energy transfer. In this thesis, we focus on the parametric nonlinear processes that can be seen as instantaneous since there is no energy transfer in the system.

1.3.2. NONLINEAR PARAMETRIC PROCESSES

In this thesis we study four different nonlinear parametric processes. The macroscopic polarization terms describing these nonlinear processes are given in table 1.1. These nonlinear optical parametric processes can be divided into two subcategories: degenerate and nondegenerate nonlinear processes. Second-harmonic generation (SHG) and third-harmonic generation (THG) originate from incoming light with a single frequency and are therefore called degenerate nonlinear processes. For sum-frequency generation (SFG) and four-wave mixing (FWM), two different incoming light frequencies mix

Nonlinear optical process	Macroscopic polarization
Second-harmonic generation (SHG)	$\mathbf{P}(2\omega_1) = \chi^{(2)}_{\mathrm{SHG}}\mathbf{E}(\omega_1)\mathbf{E}(\omega_1)$
Third-harmonic generation (THG)	$\mathbf{P}(3\omega_1) = \chi^{(3)}_{\mathrm{THG}}\mathbf{E}(\omega_1)\mathbf{E}(\omega_1)\mathbf{E}(\omega_1)$
Sum-frequency generation (SFG)	$\mathbf{P}(\omega_1 + \omega_2) = \chi^{(2)}_{\mathrm{SFG}}\mathbf{E}(\omega_1)\mathbf{E}(\omega_2)$
Four-wave mixing (FWM)	$\mathbf{P}(2\omega_1 - \omega_2) = \chi^{(3)}_{\mathrm{FWM}}\mathbf{E}(\omega_1)\mathbf{E}(\omega_1)\mathbf{E}(\omega_2)$

Table 1.1: Macroscopic polarization of the nonlinear processes used in this thesis.

to form a new light frequency and can therefore be called nondegenerate nonlinear processes.

The photon energy is proportional to the frequency of the light by the Planck relation: $E = \hbar\omega$, where $\hbar$ is the Planck constant divided by 2π. Therefore, another way to illustrate these nonlinear processes is by drawing their energy diagrams, as displayed in fig. 1.4.
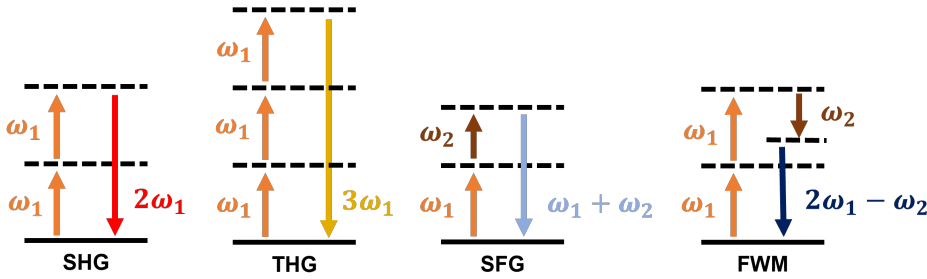
Figure 1.4: Energy diagrams of the following nonlinear optical parametric processes: second-harmonic generation (SHG), third-harmonic generation (THG), sum-frequency generation (SFG) and four-wave mixing (FWM). The length of the arrows illustrate the photon energy for the different frequencies involved in the nonlinear processes. The black solid lines are the ground states of the processes and the dashed lines indicted virtual intermediate states.

Figure 1.4 illustrates that two incident light beams with two separate frequencies can lead to multiple nonlinear signals with a range of different frequencies. In this thesis we use two beams with near-infrared frequencies corresponding to a wavelength of 775 nm and of around 1200 nm, further described in chapter 2. We can detect signals in the visible spectrum that allows us to effectively detect five types of nonlinear signals with wavelengths: 389 nm ($\mathrm{SHG_{775}}$), 400 nm ($\mathrm{THG_{1200}}$), 471 nm (SFG), 572 nm (FWM), and 600 nm ($\mathrm{SHG_{1200}}$). These nonlinear signals have different intensities depending on their corresponding nonlinear susceptibility and the intensities of the initial beams.

High intensities of the initial beams are achieved by focusing ultrashort laser pulses from a high-intensity laser source. The nonlinear susceptibilities are properties of the medium depending on their atomic structure. Interesting examples are materials that have centrosymmetric atomic structures since their second-order nonlinear susceptibility is zero. If a material is centrosymmetric around a certain axis, i.e. the x-axis, the

macroscopic polarization changes sign if the sign of the applied electric field changes,

$$P_x(\mathbf{E}) = -P_x(\textbf{-E}). \tag{1.8}$$

From substituting the second-order term from eq. 1.7 into eq. 1.8,

$$\chi^{(2)}(\mathbf{E})^2 = -\chi^{(2)}(\textbf{-E})^2, \tag{1.9}$$

it follows that $\chi^{(2)}_{xji}$ (with $j, i = x, y, z$) are zero. This type of behavior is found in many centrosymmetric materials including flat gold films or even layers of MoS$_2$ [21, 22].

1.3.3. SURFACE NONLINEAR OPTICS

Next to the power of the pump beam and the nonlinear susceptibilities, there is another important restraint for nonlinear processes, often referred to as the phase matching requirement. In order to have an efficient generation of nonlinear signals, the generated nonlinear light field should constructively interfere with the fundamental applied fields. To illustrate this requirement we discuss SHG generation of a fundamental light beam with frequency ω_1 propagating through a nonlinear medium in the x-direction. The fundamental field oscillates in time and space can be written as:

$$\mathbf{E}(x, t) = \mathbf{E}_0 e^{i(kx - \omega_1 t)} + \mathbf{E}_0 e^{-i(kx - \omega_1 t)}. \tag{1.10}$$

Here $k = \frac{n(\omega)\omega}{c}$ is the wavenumber of the field. Now, substituting eq. 1.10 in the SHG macroscopic polarization from table 1.1 gives:

$$\mathbf{P}_{\text{SHG}}(x, t) = \chi^{(2)}_{\text{SHG}}[\mathbf{E}_0 e^{i(2kx - \omega_2 t)} + \mathbf{E}_0 e^{-i(2kx - \omega_2 t)}]. \tag{1.11}$$

To obtain constructive interference between the fundamental and SHG fields $2k(\omega_2)$ should be equal to $k(\omega_1)$ leading to:

$$\frac{2n(\omega_1)\omega_1}{c} = \frac{n(\omega_2)\omega_2}{c}. \tag{1.12}$$

Since $\omega_2 = 2\omega_1$, this leads to:

$$n(\omega_1) = n(\omega_2). \tag{1.13}$$

In conclusion, for phase-matching of SHG as well as other nonlinear processes the nonlinear medium should have a linear dispersion curve. However, most materials experience chromatic dispersion that limits the nonlinear generation. The phase-matching requirement can be overcome using birefringent crystals. Depending on the crystal temperature, the refractive index of the cross-polarized components can be matched for the fundamental frequency and a single nonlinear frequency.

In this thesis, we follow another approach to overcome the phase-matching condition by studying nonlinear surface processes. This approach is not limited to the generation of a single nonlinear process but the multiple processes described in section 1.3.2 can be simultaneously generated. In the regime of surface nonlinear optics we consider the wavelength of the nonlinear process, λ_{NL}, to be much smaller than the interaction length of the nonlinear process l_{NL}:

$$\lambda_{\text{NL}} << l_{\text{NL}}. \tag{1.14}$$

The surface nonlinear optics regime can be realized using a monolayer of WS_2, a flat gold surface, or plasmonic modes. For a monolayer of WS_2 on a glass substrate the nonlinear susceptibilities of glass and air are much smaller than the nonlinear susceptibility of WS_2. Furthermore, the effective thickness of WS_2 is on the order of a nanometer. Therefore, the nonlinear interaction length is also approximately a nanometer and equation 1.14 applies. For nonlinear interactions on a gold surface, the gold has a much larger nonlinear interaction strength than the air. However, light does not propagate through gold and the nonlinear interaction length is on the order of penetration depth in gold, which is roughly 15 nm. Plasmonic modes can increase the generation of nonlinear processes because of the enhanced local electric fields near the surface. For plasmonic modes on a gold surface, the nonlinear interaction length corresponds to the penetration depth of the plasmon in the gold as plotted in fig. 1.2(c).

The relaxation of the phase-matching requirement in surface nonlinear optics allows for the simultaneous generation of multiple nonlinear processes. However, the surface nonlinear interaction strength is generally weak compared to bulk nonlinear optics in for example nonlinear crystals. Therefore, the study of surface nonlinear optics requires focused high-intensity ultrashort laser pulses and sensitive measurement equipment. Nonetheless, the study of nonlinear surface processes is very promising. In particular for applications that require the simultaneous measurement of multiple nonlinear processes, as described in chapter 4. Or to investigate different strategies for enhancing nonlinear surface processes through novel 2D materials (chapter 3 or plasmonic systems (chapter 5). Finally, nonlinear surface optics can also be an excellent spectroscopy tool to probe nano-optical processes, such as plasmon generation.

1.4. TMDC MATERIALS

1.4.1. WS_2 AS A TWO-DIMENSIONAL MATERIAL

Tungsten disulfide (WS_2) is part of the transition metal dichalcogenides (TMDCs) group. The atomic composition of TMDC materials consists of one transition metal atom (e.g. Mo or W) and two chalcogen atoms (e.g. S, Se, or Te). Because of the weak van der Waals forces between the atomic unit cell layers, single monolayer sheets can be separated from the bulk crystal.

Monolayer sheets of TMDCs are atomically flat and have a thickness of only three atoms while they can extend for tens of micrometers. Due to their small thickness compared to the size of the flakes, mono and few-layer TMDCs are often referred to as two-dimensional (2D) materials. A schematic representation of the atomic structure of monolayer WS_2 is displayed in fig. 1.5. Monolayers of TMDC can have totally different mechanical, electrical, and optical properties than their bulk counterparts [23, 24]. In this thesis, we are mostly interested in the optical properties of TMDCs, specifically WS_2.

If we consider at the band diagram of WS_2 we see that for its bulk state WS_2 is a semiconductor with an indirect bandgap. Also few-layer WS_2 experiences an indirect lowest energy bandgap, however going down to a monolayer the band structure of WS_2 changes, forming a direct bandgap in the optical regime with a bandgap energy 1.95 eV (636 nm) [25] and a strong binding energy of 0.71 eV [26]. This bandgap is located at the K and K' points in the Brillouin zone due to C_{3h} crystal symmetry of the WS_2. Furthermore,

1

spin splitting occurs at the K point of the valance band due to the spin-orbit coupling induced by the heavy tungsten atoms.
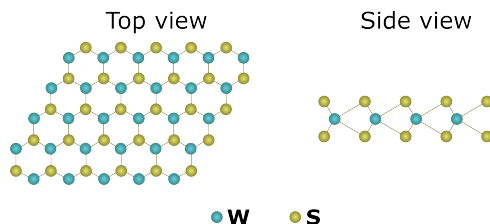

Figure 1.5: Schematic representation of a WS$_2$ monolayer from a top and side view.

1.4.2. PHOTOLUMINESCENCE

Electron-hole pairs, called excitons, can be formed at the bandgap of WS$_2$ when light with a photon energy above the exciton energy is absorbed. The excitons can relax back to the ground state via radiative and non-radiative recombination. In the radiative recombination process, a photon is emitted with a frequency corresponding to the exciton energy, which is lower than the bandgap energy due to the Coulomb interaction between the negative electron and positive hole. This absorption and emission process, illustrated in fig. 1.6, is called photoluminescence (PL).

Linear PL measurements are performed by exciting the WS$_2$ with frequencies that have a higher energy than the exciton energy. The frequency of the initial excitation light is filtered from the collected light to separate the PL contribution from the reflected light. The PL signal can be measured using a spectrometer or a sensitive photodetector. These PL measurements are often used for the identification of monolayers since the PL emission is an order of magnitude higher for monolayers with respect to a few layers. Also, the PL spectrum of multi-layer WS$_2$ shows a signal at lower frequencies originating from the indirect bandgap which is absent in the PL spectra for a monolayer.

Next to linear PL also nonlinear PL processes can occur in 2D TMDC materials. For nonlinear PL the exciton is excited by multiple photons that have an individual photon energy lower than the exciton energy, for example a second harmonic process that is illustrated in fig. 1.6. A nonlinear PL signal only appears in experiments with strong initial beam excitation and has a signal intensity comparable to that of nonlinear processes. Therefore, the nonlinear PL signal is considerably weaker than a linear PL signal. Nonetheless, nonlinear PL is still an important characterization tool for TMDC materials. Because the initial pump frequency is far away from the PL signal a sharp bandpass filter for the initial pump frequency is not required. This also allows for PL experiments where the exciton is generated exactly at the bandgap energy which is impossible for linear PL measurements since the initial pump beam can not be filtered out.
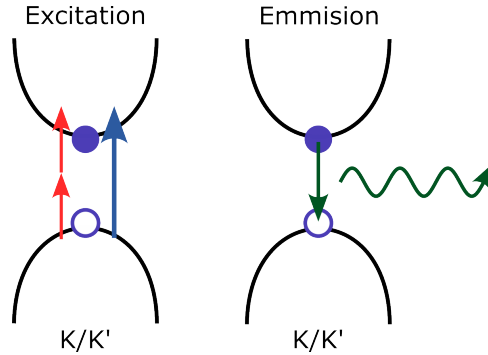
Figure 1.6: Illustration of the photoluminescence process in WS$_2$. Linear (blue arrow) or nonlinear (red arrows) absorption excites excitons at the K and K' points in the Brillouin zone. Light with the frequency corresponding to the exciton energy is emitted via radiative recombination of the exciton.

1.4.3. NONLINEAR INTERACTION

Besides photoluminescence studies, there has been an increased scientific focus on the nonlinear parametric properties of 2D TMDCs. The nonlinear optical response of several 2D TMDCs has been reported to be remarkably large [27, 28]. Several nonlinear processes have been observed in TMDC materials including degenerate processes (SHG, THG) [29, 30], and nondegenerate processes (FWM) [31, 32]. Inversion symmetry breaking and efficient light-matter interaction make TMDCs engaging materials for nonlinear optical experiments and applications.

Nonlinear optics can reveal a great variety of material properties of 2D TMDC crystals. For instance, the intensity of nonlinear signals depends on the relative angle between the polarization of the incoming light to the crystal orientation, as well as on the strain applied to the TMDC crystal [33]. This makes nonlinear optics a sensitive tool to measure the crystal orientation and stress in the crystal. Nonlinear processes also show a different intensity response for a different number of layers [34], which can be helpful for the identification of layer numbers. Finally, the C$_{3h}$ crystal symmetry structure can lead to nonlinear chirality effects, such as nonlinear chiral selection rules [35] or nonlinear sensitivity to valley polarization [36].

The high nonlinear response in combination with the thin dimensions of TMDCs leads to a broad range of application perspectives. For example, 2D TMDCs can be utilized for the electrical modulation of nonlinear signals [37]. Or applications that require simultaneous measurements of nondegenerate nonlinear signals are further discussed in chapter 4.

1.4.4. INTEGRATION OF 2D MATERIALS

The integration of 2D TMDCs in multi-layer systems or with other nanostructures is a very promising area for novel research. Pick-up and stamp techniques allow monolayer or few-layers samples to be transferred to different (pre-patterned) substrates or combined with other 2D materials[24, 38]. The combination of different 2D TMDC materials can lead to many opportunities for new research experiments and nanophotonic devices. For example, hexagonal boron nitride (hBN) - WS$_2$ interfaces can be created where

1

hBN acts as a thin atomically flat dielectric layer or the combination of two TMDCs at a certain twist angle that leads to moire patterns [39].

Furthermore, 2D TMDCs can be combined with other nanostructures such as plasmonic [40] or dielectric waveguides [41]. In this way, the near-field of the confined waveguide mode can interact with the nearby TMDC material to generate nonlinear signals. Another exciting application is to guide the coupling of free-space light to plasmonic modes using TMDC materials [42].

1.5. Outline of this thesis

In chapters 3, 4, 5 and 6 of this thesis, we discuss four nano-optical experiments connected to the key concepts introduced in this chapter. In each experimental chapter we separately elaborate on the different sample fabrication techniques, experimental setups, and further applications of the experiments.

In chapter 2 we give a more detailed description of the experimental techniques and fabrication processes used in this thesis. In chapter 3 and 4 we discuss different nonlinear signals generated by 2D materials. In chapter 5 and 6 we investigate plasmonic systems whereas in chapter 5 we combine plasmonics with nonlinear signals.

- In chapter 2 we discuss the experimental techniques used in this thesis. Including a description of the nanofabrication processes of the samples and the optical setups used in the experiments.

- In chapter 3 we investigate the nondegenerate nonlinear optical power response of a monolayer WS$_2$ including two-photon photoluminescence.

- In chapter 4 we demonstrate a novel FROG technique in a monolayer WS$_2$ to measure the temporal intensity distribution and phase of two different color laser pulses simultaneously using multiple nondegenerate nonlinear signals.

- In chapter 5 we study plasmon enhanced nonlinear signals using a double resonant metallic grating. We demonstrate a large enhancement of nondegenerate nonlinear signals using the double resonant metallic grating.

- In chapter 6 we explore the generation and propagation of the (anti)symmetric plasmonic modes in a two-wire transition line (TWTL) system using a near-field microscope.

- In chapter 7 we draw the conclusions of this thesis.

2

EXPERIMENTAL SETUPS AND NANOFABRICATION TECHNIQUES

In this thesis, we perform optical experiments on a monolayer of WS$_2$ and gold nanostructures. We explore the light-matter interaction of these samples using a nonlinear spectroscopy setup and scanning near-field microscopy setup. Here, we first describe the nonlinear spectroscopy setup and near-field microscopy setup. Secondly, we discuss the fabrication techniques of WS$_2$ monolayer and gold nanostructure samples.

2.1. EXPERIMENTAL SETUPS

2.1.1. NONLINEAR SPECTROSCOPY

The nonlinear optical signals generated in this thesis result from two femtosecond pump laser pulses at different frequencies. The two initial femtosecond pump beams are generated by a three-part laser system consisting of a continuous-wave pump laser (Millennia XsJ, Spectra-Physics), a Ti-sapphire oscillator (Tsunami, Spectra-Physics) system, and an optical parametric oscillator (Opal, Spectra-Physics). The continuous-wave laser generates a laser beam at 532 nm with an output power of 10 W. The continuous-wave laser pumps the Ti:sapphire oscillator that generates femtosecond laser pulses around 150 fs at a central wavelength of 775 nm with an output power of approximately 2 W. The optical parametric oscillator converts the femtosecond laser pulses to a signal and an idler. The wavelength of the signal can be tuned from 1150 nm up to 1300 nm. For our nonlinear experiments, we use pulses from the signal output of the optical parametric oscillator with a wavelength of around 1200 nm and from the residue output with a wavelength of the pump beam at 775 nm. Both beams have an average output power of up to 200 mW.

The two laser pulses follow distinct beam paths to adjust the beam properties individually. We spatially align the beams using beam walking techniques with two mirrors for each path. Using a delay line with a motorized linear translation stage we overlap the laser pulses in time. The power of the individual laser beams can be separately regulated using a combination of a half-wave plate and a polarizing beamsplitter. The angle of the linearly polarized laser beams can be adjusted independently using a final half-wave plate in each beam path. Finally, the beam paths of the two wavelengths are combined using a dichroic mirror.

The combined laser pulses around 775 nm and 1200 nm are used as fundamental pump beams in a nonlinear spectroscopy setup as sketched in fig. 2.1(a). This setup is designed so that it can act as a nonlinear scanning microscope (fig. 2.1(a)) as well as an optical white light microscope (fig. 2.1(b)). In the nonlinear scanning microscope, the nonlinear spectrum is generated through the interaction of the pump beams with the samples and measured using a spectroscope. The two pump beams are directed by a dichroic mirror (Thorlabs DMSP650L) towards a superachromatic objective (Olympus UPlanSApo 40×, NA=.95). Both pump beams fill the aperture of the objective and are focused on the sample. The sample is mounted on a motorized translation stage that is adjustable in three dimensions. The emitted nonlinear spectra are collected by the same objective. The fundamental wavelengths get separated from the emitted light using the dichroic mirror. This dichroic mirror transmits nonlinear signals with a wavelength below 650 nm but reflects the fundamental wavelengths around 775 nm and 1200 nm. A small residue of the reflected fundamental light is filtered by two extra bandpass filters (Thorlabs FESH0750). A lens images the nonlinearly generated light onto either the entrance of a highly sensitive spectrometer) (SpectraPro 2300I) or a CCD camera depending on the position of an additional mirror on a flip mount.
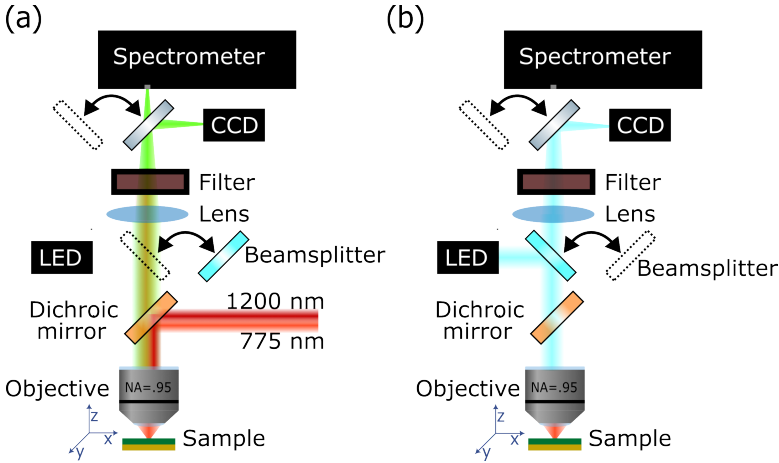
Figure 2.1: Schematic illustration of the optical nonlinear setup. (a) In the nondegenerate nonlinear spectroscopy configuration. (b) In the optical white light microscope configuration to locate WS$_2$ flakes and gold nanostructures.

The same optical microscopy setup can also be utilized as a regular white light microscope, using a LED source depicted in fig. 2.1(b). In this configuration, a 90/10 (transmission/reflection) beamsplitter is inserted in the optical path using a flip mount to direct the LED light toward the objective. The nonlinear microscopy setup remains unchanged while using the LED configuration. Therefore, the nonlinear microscope and the white light microscope can even be operated at the same time. However, simultaneously using the nonlinear and white light microscope has the disadvantage of losing some of the nonlinearly generated light that gets reflected in the beamsplitter after the dichroic mirror that is used to merge the white light source. Using the nonlinear setup simultaneously as a white light microscope allows for identifying the microscopic target on the sample and spatially aligning the pump beams on the target.

2.1.2. Near-field microscope

Next to a collection-type near-field scanning optical microscope (c-NSOM) to probe the propagation of plasmonic modes. This c-NSOM setup is already extensively discussed in the literature [43–46] and will therefore only be briefly discussed here.

The main method of measuring plasmonic modes with a c-NSOM is illustrated in fig. 2.2. The c-NSOM uses an aperture-based probe [47] consisting of a tapered fiber coated with a metallic layer as shown in the inset of fig. 2.2. The probe is brought in close proximity (∼ 20 nm) to the metallic nanostructure. The confined light field of a plasmon can couple to the near-field probe, via evanescent field coupling. Subsequently, the evanescent field is coupled to a light mode in the fiber that can be measured with photodetectors at the end of the fiber. The x- and y-components of the evanescent field can be individually collected by the near-field probe and can be separately measured using a polarizing beamsplitter before the detector [48]. Using a heterodyne detection scheme with lock-in amplifiers, we obtain the local phase of the light where we combine the collected light with a reference branch detuned at 40 kHz [49]. Scanning the probe

over the plasmonic surface with piezo actuators and an electronic feedback loop leads to an experimental map of the local amplitude, polarization, and phase of the plasmonic mode. More information can be found in the review by Rotenberg and Kuipers [46].
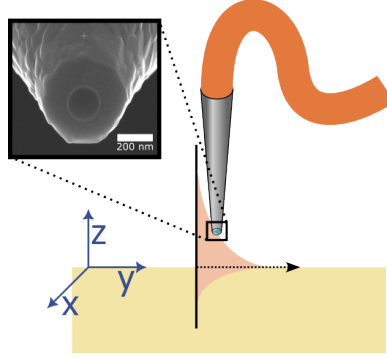
Figure 2.2: Schematic illustration of a collection-type near-field scanning optical microscope probing a plasmonic mode confined to a metallic surface. The inset shows a scanning electron microscope image of a near-field probe.

2.2. Nanofabrication

2.2.1. WS$_2$ monolayers

Two often used fabrication methods for two-dimensional transition metal dichalcogenides (TMDC) materials are mechanical exfoliation [23, 50, 51] and chemical vapor deposition (CVD) [23, 52, 53]. Using mechanical exfoliation single layers can be extracted from the bulk crystal using scotch tape (3M, Magic tape) and placed on a substrate. Using CVD, TMDC materials are grown on a substrate using gas flow through a chemical reaction chamber. Depending on the growth parameters, monolayer structures can be formed as well as more complicated structures such as nanowalls [54], nanopillars [55], and pyramid and flower structures [56, 57].

In this thesis, we use mechanically exfoliated WS$_2$ monolayers on top of a glass substrate. Although many different substrates can be used to mechanically exfoliate WS$_2$ on, such as gold or silicon, we use glass due to its low nonlinear susceptibilities. Therefore, the measured nonlinear signals are solely generated by WS$_2$.

Prior to exfoliating the WS$_2$, the glass substrate is cleaned extensively using an ultrasonic acetone bath and oxygen plasma with a glass flow of 600 ml/min for 2 minutes to improve the yield and quality of the monolayers. Next, layers of WS$_2$ are separated from the bulk crystal using magic tape and stamped onto the glass substrate. Before the tape is removed from the glass substrate, the sample is annealed typically for 2 minutes at 100° Celsius using a laboratory hot plate. The yield of WS$_2$ monolayers as well as their size is strongly dependent on the specific recipe proprieties such as the baking time and cleanness of the substrate [24, 50].

After the exfoliation steps, the glass substrate is covered with thin WS$_2$ layers. A typical microscope image of a WS$_2$ flake with multiple layer thicknesses is displayed in fig. 2.3(a). In the next step, an optical white light microscope is used to generate an overview

map of the WS$_2$ layers and identify potential monolayer flakes. The thickness of the WS$_2$ flakes on a glass substrate is evaluated by their transparency. The flakes become more transparent as they get thinner. The high transparency of the monolayer flakes of WS$_2$ makes it challenging to identify monolayer flakes on a glass substrate and finding them can be a time-intensive task. Finally, photoluminescence measurements are performed to verify that the selected flakes are indeed monolayers. In fig. 2.3(b) we plot the photo-luminescence spectra of a monolayer flake and a bilayer WS$_2$ flake exfoliated on a silicon substrate. The monolayer flake experience a large emission signal from the direct exci-ton at 630 nm. The bilayer flake shows a smaller signal from the direct exciton bandgap at 630 nm and has an additional peak at 700 nm from the indirect bandgap [23, 42, 58].
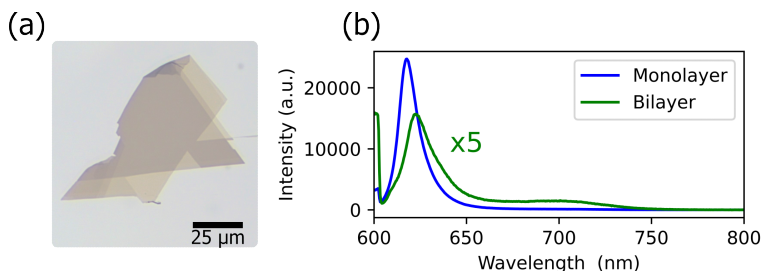
Figure 2.3: (a) Example of a white light microscope image of a WS$_2$ flake exfoliated on glass. (b) Example of linear photoluminescence spectra for a monolayer and a bilayer WS$_2$ exfoliated on a silicon substrate.

2.2.2. GOLD NANOSTRUCTURES

There are two typical techniques for the nanofabrication of gold plasmonic nanostruc-tures relying on focused ion beam (FIB) milling or electron-beam lithography. In this thesis, both methods are used.

In chapter 5 we use FIB milling to pattern a grating structure onto a gold film. This process is illustrated in fig. 2.4. In this process, we start with a cleaned glass substrate. We clean the glass substrate either by immersion in fuming nitric acid or using Tergitol^{TM} soap in combination with ultra-sonic baths of acetone, isopropyl alcohol, and ethanol. Next, we evaporate an adhesion layer of chromium of a few nanometers before we evap-orate a thin layer of gold using e-beam evaporation (Temescal FC-2000). With a focused beam of gallium ions, a pattern is etched into the gold film, where the etching depth depends on the beam intensity and exposure time (Helios, G4 CX DualBeam). Using the same Helios device we can immediately inspect the patterned grating using scan-ning electron microscopy. The last image displayed in fig. 2.4 is a scanning electron mi-croscope image of a nano grating fabricated using focussed ion beam milling. The ion beam milling technique is especially useful for creating structures with different height profiles. The resolution of the FIB patterning is limited by the spot size of the focused gallium ion beam. FIB milling can be used not only for gratings but also for the fabrica-tion of other structures such as nanowires. Recent studies use FIB patterning on single crystalline metallic flakes to obtain nanostructures with very smooth plasmonic inter-faces [13, 14, 59].

The second technique involves electron-beam patterning followed by a lift-off proce-

dure, illustrated in fig. 2.5. We start with a cleaned glass substrate similar to the substrate used for the focussed ion beam milling fabrication technique. Next, we spin coat a positive electron-beam resist (CSAR AR-P6200.04) on top of the glass substrate. On top of the resist, an extra layer of conductive coating (electra-95) is spin-coated as a grounding layer for the electron-beam patterning. Next, the nanostructure shapes are patterned into the resists using a focused electron beam (Raith EBPG5200) with a typical dose of 585 μC/cm^2 and an acceleration voltage of 100 keV. The patterned resist is developed using pentyl acetate for 60 seconds and rinsed using 5 seconds of o-xylene followed by isopropyl alcohol for 60 seconds. In the next step, a gold layer with the desired thickness is deposited using e-beam evaporation (Temescal FC-2000) on top of the patterned resists. Here we use an adhesion layer of titanium instead of chromium because this gives the possibility to coat the final sample with chromium in a later stage for electron microscope imaging and remove it afterward with a chromium etchant. Finally, the resist is chemically removed (AR 600-71) in a lift-off process. We observe that the lift-off process can be stimulated using a low-power ultrasonic bath for a few minutes although it is necessary to use caution in order to avoid breaking the gold nanostructures. After the lift-off processes, only the gold nanostructures remain on the glass substrate. A scanning electron microscope image of a double spiral structure created using this fabrication process can be observed in the last illustration of fig. 2.5.

There are several advantages and disadvantages for both nanofabrication techniques. First, the fabrication cycle is a lot longer for the electron-beam lithography process than for the FIB milling process because there are more cleanroom steps involved in the electron-beam process. The FIB used in this thesis has a built-in electron microscopy tool allowing for direct imaging after the writing of the nanostructures. Using electron-beam lithography the structures can only be inspected with a scanning electron microscope after all the process steps are completed. Furthermore, plasmonic structures can experience charging effects during scanning electron microscope inspection. This can be circumvented by sputtering a thin layer of chromium on top of the sample to ground the structure and remove the metal layer after inspection.

Secondly, the resolution of the gold nanostructures can be smaller using electron-beam lithography due to the smaller spot size of the electron beam with respect to the ion beam. However, for the dimensions of most typical plasmonics systems, the resolution of FIB milling is sufficient.

Thirdly, the writing time of the electron-beam pattering is much faster than the writing time of FIB milling. Therefore, electron-beam lithography is capable of writing many structures in a single fabrication round. This is not only useful for the scientific investigation of many different nanostructure systems but also makes this technique more scalable for future real-world applications.

Finally, electron-beam lithography can be advantageous for the combined nanofabrication of plasmonic systems together with dielectric waveguides or two-dimensional materials since it is a less destructive technique.
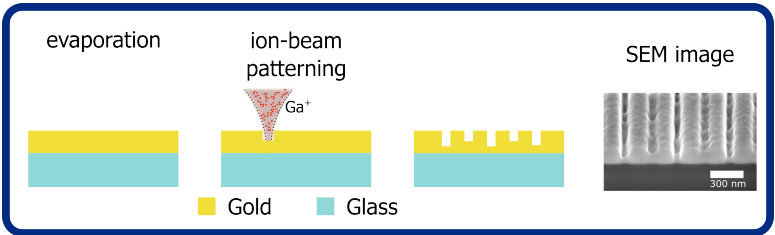
Figure 2.4: Schematic illustrations of the nanofabrication steps using focused ion beam milling to create a nanostructured grating pattern in a gold film. The final illustration shows a scanning electron microscope image of a grating pattern fabricated using focussed ion beam milling.
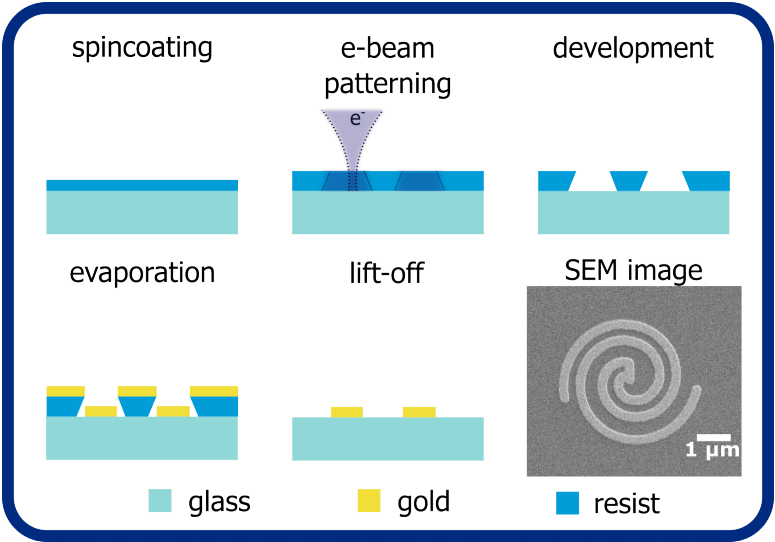
Figure 2.5: Schematic illustrations of the nanofabrication steps using electron-beam lithography and lift-off processes to create gold plasmonic nanostructures. The final illustration shows a scanning electron microscope image of an example of a double spiral structure fabricated using electron-beam lithography and lift-off processes.

II

NONLINEAR RESPONSE OF TWO DIMENSIONAL WS$_2$

3

NONLINEAR SIGNALS AND POWER DEPENDENCY

In this chapter, we investigate the interplay between nonlinear photoluminescence (PL) and several degenerate and nondegenerate nonlinear optical processes of a WS$_2$ monolayer at room temperature. We illuminate the sample using two femtosecond laser pulses at frequencies ω_1 and ω_2 with photon energies below the optical bandgap. As a result, the sample emits light that shows characteristic spectral peaks of the second-harmonic generation, sum-frequency generation and four-wave mixing. In addition, we find that both resonant and off-resonant nonlinear excitation via frequency mixing contributes to the (nonlinear) PL emission at the A-exciton frequency. The PL exhibits a clear correlation with the observed nonlinear effects, which we attribute to the generation of excitons via degenerate and nondegenerate multi-photon absorption. Our work illustrates a further step towards understanding the fundamental relation between parametric and nonparametric nondegenerate optical mechanisms in transition-metal dichalcogenides.

3.1. INTRODUCTION

Upon intense laser illumination transition-metal dichalcogenide (TMDC) materials can generate parametric and non-parametric signals, as further discussed in section 1.4. The parametric nonlinear processes can be divided into degenerate processes, e.g. second-harmonic generation (SHG), and nondegenerate processes, e.g. sum-frequency generation (SFG) and four-wave mixing (FWM). The already extensive range of applications, where degenerate mechanisms are typically employed, would benefit from using non-degenerate nonlinear mechanisms. For example, in materials science and quantum technologies, FWM has been reported to provide a superior way of (i) characterizing the thickness of few-layered TMDCs over second-order nonlinear processes [34, 61] and (ii) creating entangled photon pairs using carbon nanotube films [62]. Therefore, it is relevant to achieve a better fundamental understanding of the relationship between nondegenerate parametric and nonparametric optical mechanisms in TMDCs.

To understand the above-mentioned relationship in TMDCs, it is crucial to consider the role of excitons in parametric processes and their effect on the nth-order nonlinear susceptibility $\chi^{(n)}(\omega)$. In the case of two-dimensional materials, it is more adequate to use the surface conductivity $\sigma^{(n)}$ to describe the nonlinear optical response by relating the sheet current $j^{(n)}(\omega)$ to the electric field $E(\omega)$, where $\sigma^{(n)}$ is a $(n+1)^{th}$-rank tensor that depends strongly on the symmetry of the crystal structure of the medium and its composition.

The contribution of light-induced excitons to the $\sigma^{(n)}$ of TMDCs is particularly relevant as resonances between the laser frequency and excitonic states favor certain multi-photon-based mechanisms. These resonances and the selection rules for one-photon and two-photon PL have been reported in systems with reduced dimensionalities such as carbon nanotubes and TMDC monolayers [28, 63]. For TMDC monolayers the role of excitons is even more relevant than for their multi-layer and bulk counterparts, as the Coulomb interaction between electrons and holes is enhanced due to the quantum confinement and the reduced dielectric screening inherent to an atomically thin system [28]. In turn, this enhancement leads to an increase of radiative transition probabilities and the implication of the presence of excitons on the nonlinear response of monolayers.

Lafrentz et al. recently developed a microscopic theory to explain the role of the symmetries of the wavefunctions of excitons on the nonlinear optical response of ZnO [64]. Later, this theory was used to derive the second-order susceptibility that explains SHG at exciton resonances in WSe$_2$ [28]. However, the generation of excitons via nondegenerate multi-photon absorption, its influence on the nonlinear response of TMDC monolayers and on the PL emission has not been investigated yet.

In this chapter, we report on the nonlinear optical response of a WS$_2$ monolayer upon two-color laser illumination and its relation with the nonlinearly generated exciton PL. We use multi-photon spectroscopy to measure the emission spectra that arise when exciting the sample at room temperature with laser pulses at two different wavelengths λ_1 = 775 nm and λ_2 = 1200 nm that are temporally and spatially overlapped as shown in fig. 3.1(a). We find a strong nonlinear response simultaneously identifying several parametric mechanisms, including SHG, SFG and FWM, as well as nonparametric processes like nonlinear PL. On one hand, we demonstrate the contribution of both degenerate and nondegenerate multi-photon absorption to the generation of excitons that result in

nonlinear PL emission. On the other hand, we observe an enhanced SHG signal around the A-exciton resonance. We discuss these observations taking into account the parametric and nonparametric nature of the involved mechanisms.

3.2. Experiment and Methods

Our sample consists of flakes of WS_2 on a thin glass substrate. We mechanically exfoliate commercially available bulk WS_2 (2D semiconductor) and transfer it onto the glass substrate using tape. The glass substrate is cleaned, before the transfer process, both using chemicals and oxygen plasma. The sample is shortly heated at 100 °C before the removal of the tape (see also [42]). We first inspect the sample using optical microscopy and then identify monolayers by recording their spectral signature with our multi-photon spectroscopy system [65]. Figure 3.1(b) presents a room temperature PL spectrum of a WS_2 monolayer centered at approximately 1.97 eV.

During the experiments, we illuminate the WS_2 monolayer using two linearly polarized ultrashort laser pulses at λ_1 = 775 nm and λ_2 = 1200 nm as shown in fig. 3.1 (a). These laser pulses are delivered by a femtosecond laser oscillator and a tunable optical parametric oscillator (λ_2 = 1100-1300 nm). The laser beam at 775 nm runs via a motorized linear stage to control the time delay Δt between the pulses. The pulses are recombined using a dichroic mirror and then focused at the sample surface by means of a microscope objective (NA = 0.95), thus achieving spatial and temporal overlap. We use an in-situ optical microscope to select specific flakes and to inspect the sample surface during the experiments. The light emitted from the WS_2 flake is collected by the objective and imaged both at the slit of a spectrometer and at the chip of a CCD camera. Note that we use two concatenated low-pass filters (430 nm < λ < 650 nm, FES0650) and a dichroic mirror (cut-on wavelength 650 nm) to filter out the fundamental infrared wavelengths λ_1 and λ_2, while being able to detect the light emitted in the visible/ultra-violet spectral range.
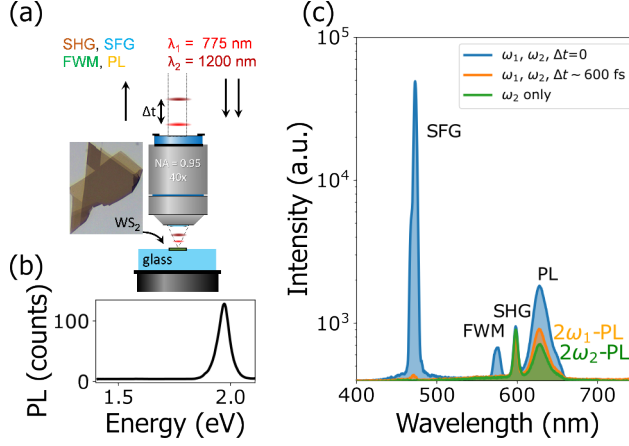
Figure 3.1: (a) Schematic of the experimental setup. Two laser beams at λ_1 and λ_2 are focused onto a WS$_2$ monolayer using an objective lens. The emitted light, including SHG, SFG, FWM and PL, is collected by the same lens and detected using a spectrometer. (b) PL spectrum of the WS$_2$ monolayer. The PL shown here was generated using an excitation laser wavelength of 1180 nm. (c) Emission spectra acquired upon multi-wavelength laser illumination and different time delays. The curves present the spectra collected upon illumination with ω_2-only (green), ω_1 and ω_2 with (blue, $\Delta t = 0$ fs) and without (orange, $\Delta t = 600$ fs) temporal overlap. The average power values of the beams at λ_1 and λ_2 were set to be 53 mW and 21 mW, respectively, at a repetition rate of 82 MHz and with a pulse duration of approximately 230 fs. The polarization angle of the beams is parallel with respect to each other and its angle with respect to the sample was optimized to maximize the FWM signal. The color labels on the right-hand side indicate the different multi-photon mechanisms that lead to PL, *i.e.* 2-photon absorption that leads to PL, $2\omega_1$PL and $2\omega_2$PL.

3.3. RESULTS AND DISCUSSION

3.3.1. RESONANT SECOND-HARMONIC GENERATION

In fig. 3.1(c) we present emission spectra from the excited monolayer for three illumination conditions: ω_2-only (green), ω_1 and ω_2 together without (orange) and with (blue) temporal overlap, respectively. Note that the individual laser pulse energies are kept constant irrespective of the illumination configuration. For the wavelength range under investigation, illumination with ω_2-only leads to SHG and degenerate two-photon PL (green curve). Illumination with ω_1 and ω_2 laser pulses, at a time delay of $\Delta t = 0$, results in four emission peaks generated via SFG, FWM, SHG and PL (blue line). In contrast, the same illumination arrangement, with a $\Delta t = 600$ fs, shows the spectral peaks corresponding to SHG and PL and a highly diminished SFG peak (orange line). The second-order surface conductivity $\sigma^{(2)}$ mediates the generation of nonlinear sheet currents, resulting in SHG and SFG at $2\omega_2$ and $\omega_1+\omega_2$, which we observe around 600 nm and 471 nm, respectively. The third-order surface conductivity $\sigma^{(3)}$ gives rise to FWM at $2\omega_1$-ω_2 and $2\omega_2$-ω_1, as shown at 572 nm (the peak at 2657 nm is not measured). Table 3.1 summarizes the nonlinear processes relevant to this study and the frequencies that we observe experimentally. The equations in Table 3.1 provide a way to distinguish the role and order of different nonlinear processes on the WS$_2$ monolayer [19, 66]. We also measure a broad PL emission peak near the A-exciton frequency ($\lambda_e \approx 625$ nm), which is characteristic of a WS$_2$ monolayer as shown in fig. 3.1(b). The origin of PL here is

Table 3.1: **Nonlinear optical processes at WS$_2$.**

Process	Frequency ω_{NL}	Sheet current
SHG	$2\omega_2$ (600 nm)	$j^{(2)} = \sigma^{(2)} E(\omega_2) E(\omega_2)$
SFG	$\omega_1 + \omega_2$ (471 nm)	$j^{(2)} = \sigma^{(2)} E(\omega_1) E(\omega_2)$
FWM	$2\omega_1 - \omega_2$ (572 nm)	$j^{(3)} = \sigma^{(3)} E(\omega_1) E(\omega_1) E(\omega_2)$

exclusively nonlinear since both of the laser photon energies, $\hbar\omega_1$ = 1.6 eV and $\hbar\omega_2$ = 1.0 eV, are below the optical bandgap ($\approx$ 1.94 eV) [67, 68]. In a nonparametric process like nonlinear PL, multi-photon absorption can lead to excited electrons via degenerate or nondegenerate excitation channels. After laser excitation, the excited electrons undergo a fast non-radiative relaxation to a lower energy state (i.e. excitonic ground state) and subsequently emit a photon that we identify as nonlinear PL in our spectra. We use the data acquired with the three illumination conditions in fig. 3.1(c) to elucidate which of the multi-photon excitation channels presented in the second column of Table 3.1 are responsible for the nonlinear exciton PL.

The PL emission obtained using (i) ω_2-only and (ii) ω_1 and ω_2 with Δt = 600 fs can exclusively be attributed to degenerate two-photon absorption mechanisms. The green-colored area corresponds to PL generated via $2\omega_2$PL (see green label), whereas the orange area that is visible on the graph (see orange label) accounts for the contribution due to $2\omega_1$PL. Consequently, the PL emission peak is more intense when exciting with ω_1, ω_2 and Δt = 600 fs where both $2\omega_1$ and $2\omega_2$ combine to produce two-photon PL (without any degenerate contribution). Interestingly, the blue spectrum illustrates that the PL emission doubles when the time-delay is set to zero, *i.e.* blue area. This increase could tentatively be attributed to the generation of excitons following $\omega_1 + \omega_2$ and $2\omega_1 - \omega_2$ multi-photon absorption pathways. Still, to be able to confirm its precise source and the order of the corresponding nonlinearity, we need to individually investigate the relation between the nonlinear PL emission and the rest of nonlinearities as a function of the laser energy.

We first focus on the nonlinear optical response upon single monochromatic light illumination with ω_2. We show the energy dependence of the SHG intensity ($2\omega_2$) in fig. 3.2(a). The experimental data (blue triangles) illustrate a quadratic response that we confirm by fitting a second-order monomial function similar to the SHG formula in Table 3.1 (solid line). In order to probe the influence of the exciton at 625 nm on the nonlinear response, we also study the SHG and the $2\omega_2$ PL obtained with several independent laser excitation wavelengths. During the experiment, we illuminated the monolayer with one laser beam at a time with wavelengths that range from 1150 nm to 1320 nm, thus the second harmonic ranges from 575 nm to 660 nm as shown by the spectra depicted in fig. 3.2(b). The energy per pulse was set to be the same irrespective of the wavelength. To retrieve the information of the SHG and PL signals, we fit a double Gaussian function (see solid black lines) to the experimental data as illustrated in the inset. The graph in fig. 3.2(c) depicts the peak intensity of the two-photon PL (orange) and SHG (blue) extracted from the fits. We observe a flat response of the two-photon PL signal around the 1s A-exciton, that is slightly larger when λ_{SHG} < 625 nm. On the other hand, both the spectra in fig. 3.2(b) and the graph in fig. 3.2(c) clearly illustrate an enhanced SHG emission
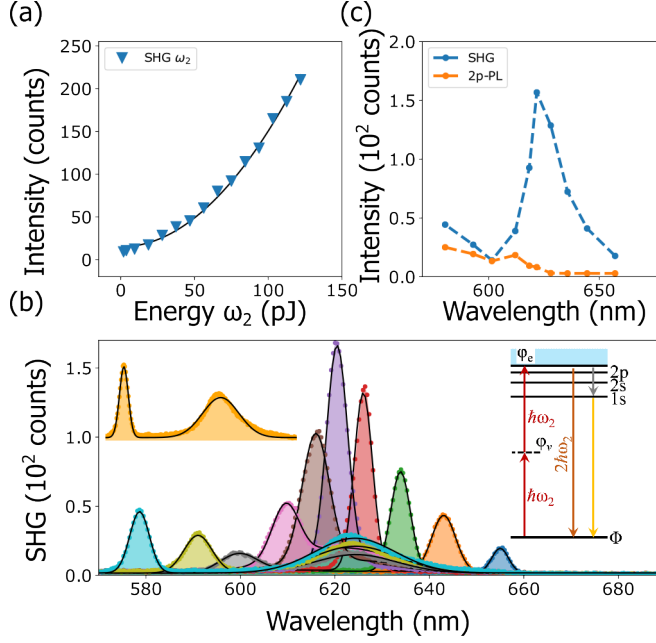
3

Figure 3.2: (a) SHG ($2\omega_2$) at 600 nm as a function of the laser pulse energy with $\lambda_2 = 1200$ nm. (b) Emission spectra obtained upon illumination using several excitation wavelengths, which are shown in the upper x-axis. All spectra in (b) were measured using an average power of 8 mW and a repetition rate of 82 MHz. The inset on the right-hand side of (b) illustrates a schematic of the SHG and $2\omega_2$PL mechanisms using an energy level diagram, where CB and VB corresponds to the conduction band and valence band, respectively. The 1s, 2p and 3p excitonic states correspond to the energies 2.05 eV, 2.28 eV and 2.49 eV computed in reference [69]. (c) SHG and PL intensity as a function of wavelength ($\lambda_2/2$). To disentangle the relative contributions of the SHG and PL, we performed a double Gaussian fit to the spectra in (b) (see black solid lines and inset in (b)) to obtain the data in (c). We kept the same width and central peak for the PL signal while finding the best fit for the width and peak position of the SHG. The solid lines illustrate the fits.

I_{SHG} when the harmonic is in resonance with the A-exciton at 625 nm, leading to an enhancement factor of $\eta = I^{max}/I^{min} \approx 11$ at 625 nm. The origin of this enhancement can be understood by using the microscopic theory mentioned in the introduction that describes the second-order surface conductivity $\sigma^{(2)}$ taking into account the contribution of excitons [28, 64].

To explain the SHG and two-photon PL mechanisms, we use the energy level diagram depicted in the inset of fig. 3.2(b). The states in the diagram correspond to the ground state $|\Phi\rangle$ (*i.e.* top of valence band of WS$_2$), an intermediate virtual state $|\varphi_v\rangle$ and an excitonic state $|\varphi_{ex}\rangle$. According to the schematic, two laser photons with energy $\hbar\omega_2$ interact with the monolayer, and subsequently, either one photon with frequency $2\omega_2$ is emitted via SHG or a photon with frequency ω_e that corresponds to the 1s A-exciton state is emitted (*i.e.* PL at 625 nm). It is important to note here, that SHG is a parametric process whereas $2\omega_2$PL is a nonparametric process where two photons excite an electron, that decays to the exciton ground state and emits a photons via recombination.

3.3.2. NONLINEAR POWER LAWS

Figures 3.3(a) and (b) depict graphs of the intensity of the generated SFG and FWM signals as a function of the laser pulse energy for ω_1 (left) and ω_2 (right). The color markers represent the experimental data and the dashed and solid black lines are fits to linear and quadratic monomial functions, respectively. Figure 3.3(a) confirms the linear dependence of the SFG as a function of the laser energy at both frequencies. Figure 3.3(b) illustrates the quadratic (linear) energy dependence of the FWM intensity for ω_1 (ω_2).

In order to further investigate the role of nonlinear excitation channels (other than SHG) on the nonlinearly generated exciton PL, we now study the energy dependence of PL and its relation with the SFG and FWM signals. We define here the PL* as the PL signal that corresponds to the visible blue area in fig. 3.1(c). This is the result of subtracting the $2\omega_1$PL and $2\omega_2$PL integrated signals (orange and green visible areas in fig. 3.1(c)) from the total PL signal obtained while simultaneously ($\Delta t = 0$) exciting the sample with both photon frequencies. Therefore, PL* accounts exclusively for nondegenerate nonlinear PL, which originates as a result of excitation pathways where ω_1 and/or ω_2 are combined through $\omega_1 + \omega_2$ and $2\omega_1 - \omega_2$ but not via $2\omega_1$ and $2\omega_2$. We depict the PL* intensity as a function of the laser pulse energy for ω_1 (green markers) and ω_2 (red markers) in fig. 3.4(a). The PL* data illustrate a linear dependence with the laser energy, which is indicative of a dominance of the one-photon absorption contribution for each independent frequency or a preferred $\omega_1 + \omega_2$ degenerated excitation route. Moreover, the lack of a PL* quadratic scaling with the energy of the beam at ω_1 suggests a minimal implication of $2\omega_1 - \omega_2$ excitation route on the PL emission.
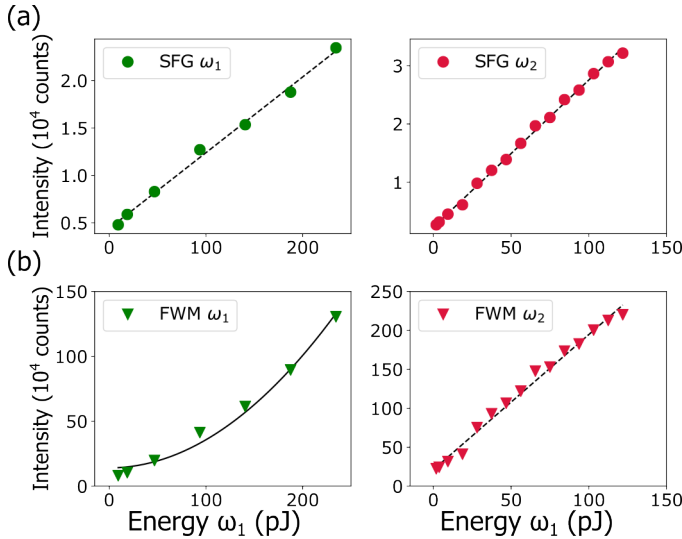
Figure 3.3: (a) SFG and (b) FWM signals as a function of the laser energy per pulse for ω_1 (left) and ω_2 (right). The energies of the beams at ω_1 in (b) and ω_2 in (a) correspond to 328 pJ and 93 pJ at a repetition rate of 82 MHz. The data in the graphs correspond to the peak values extracted from the spectra at each excitation energy.

The graphs in fig. 3.4(b) depict the SFG signal (data in fig. 3.3(a)) against the nonde-
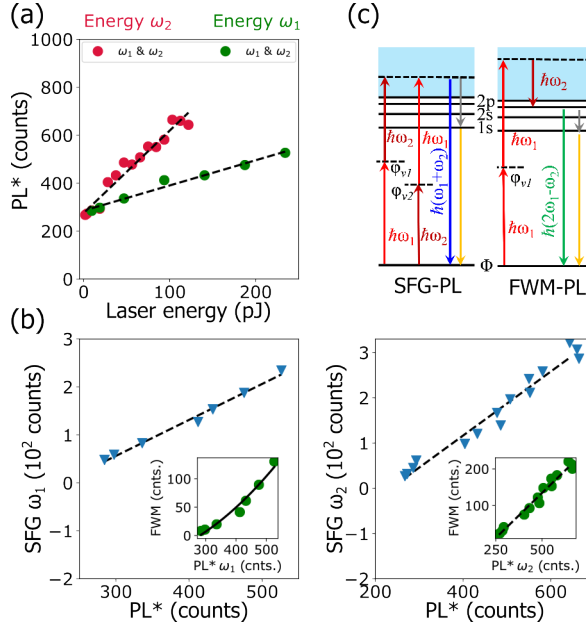
Figure 3.4: (a) Nonlinear PL* intensity as a function of laser energy at ω_1 (green) and ω_2 (red). (b) Graphs of the SFG signal as a function of the PL* signal on a WS$_2$ layers. The insets show the FWM signal as a function of the PL*. Note that the PL* intensity was calculated by subtracting the degenerate two-photon PL to the total PL. Therefore, PL* accounts exclusively for nondegenerate PL. In (a) and (b) the energies of the beams at ω_1 and ω_2 correspond to 328 pJ and 93 pJ at a repetition rate of 82 MHz. (c) Schematics of the energy levels for SFG and FWM processes. CB and VB correspond to the conduction band and valence band and 1s, 2p and 3p excitonic states correspond to the energies 2.05 eV, 2.28 eV and 2.49 eV reported in [69].

generate PL* signal (data in fig. 3.4(a)). The data in fig. 3.4(b) was acquired keeping the energy of the laser beam at ω_2 (ω_1) constant, while increasing the energy of the beam at ω_1 (ω_2). We find a clear linear correlation between PL* and SFG irrespective of the excitation frequency, which suggests that these processes share the same order nonlinearity. Analogously, the insets of fig. 3.4(b) depict the FWM signal (data in 3.3(b)) against the nondegenerate PL* signal (data in fig. 3.4(a)). The FWM versus PL* signals illustrate a quadratic and linear behavior for ω_1 and ω_2, respectively. This indicates that the FWM emission is of the same order nonlinearity as the PL* signal for ω_2 but of a higher order nonlinearity for ω_1. Furthermore, the result of these correlations points out that the nondegenerate PL* signal originates mainly via $\omega_1 + \omega_2$ excitation route. The schematics of the energy levels in fig. 3.4(c) summarize the nonlinear processes and the PL* emission assisted via $\omega_1 + \omega_2$ and $2\omega_1 - \omega_2$ multi-photon absorption. SFG mechanism follows a two-photon excitation route similar to SHG but including two possible intermediate virtual energy levels (*i.e.* nondegenerate process) corresponding to $\hbar\omega_1$ and $\hbar\omega_2$. For the parametric process two photons combine to generate a new photon via SFG. For the nonparametric process, two photons with frequencies $\omega_1 + \omega_2$ excite an electron that decays to the ground excitonic state that subsequently emits a photon as shown in the left diagram in fig. 3.4(c). Analogously, the diagram on the right-hand side in fig. 3.4(c)

shows the FWM mechanism and the $2\omega_1 - \omega_2$ assisted PL. The FWM generates via $2\hbar\omega_1$-$\hbar\omega_2$.

3.4. CONCLUSION

In summary, we have investigated the nonlinear optical response of WS$_2$ monolayers using a multi-wavelength illumination scheme. We observe and discriminate the individual influence of the degenerate and nondegenerate multi-photon absorption routes on the PL emission. We observe and explain the SHG enhancement around the 1s A-exciton of WS$_2$ at room temperature. We confirm the order of the nonlinear mechanisms by measuring the energy dependence of each spectral peak. Moreover, we find a linear and nonlinear correlation between PL and SFG and FWM, respectively. This reveals that $\omega_1 + \omega_2$ corresponds to the preferred nondegenerate excitation pathway of excitons over $2\omega_1 - \omega_2$. Finally, we propose that multi-wavelength-based nonlinear PL, in resonance with individual excitonic states in TMDCs, can be used as a sensitive observable to investigate the fast and ultrafast dynamics of excitons, which serves as an alternative route to Kerr rotation and time-resolved (linear) PL schemes. From an applied point of view, studying the influence of strain on the nonlinear response of TMDC monolayers [70] by monitoring several nonlinear effects has potential for making progress on the fabrication of flexible photonic devices.

3

4

ULTRASHORT PULSE CHARACTERIZATION

In this chapter, we exploit the high, broadband nonlinear optical response of a WS_2 monolayer to simultaneously characterize two ultrashort laser pulses with different frequencies. The relaxed phase-matching conditions in a WS_2 monolayer enable the simultaneous acquisition of the spectra resulting from both four-wave mixing (FWM) and sum-frequency generation (SFG) nonlinear processes, while varying the time delay between the two ultrashort pulses. Next, we introduce an adjusted double-blind FROG algorithm, based on iterative fast Fourier transforms between two FROG traces, to extract the intensity distribution and phase of two ultrashort pulses from the combination of their FWM and SFG FROG traces. Using this algorithm, we find an agreement between the computed and observed FROG traces for both the FWM and SFG processes. Exploiting the broadband nonlinear response of a WS_2 monolayer, we additionally characterize one of the pulses using a second-harmonic generation (SHG) FROG trace, in order to validate the pulse shapes extracted from the combination of the FWM and SFG FROG traces. The retrieved pulse shape from the SHG FROG agrees well with the pulse shape retrieved from our nondegenerate cross-correlation FROG measurement. In addition to the nonlinear parametric processes, we also observe nonlinearly generated photoluminescence signal (PL) emitted from the WS_2 monolayer.

4.1. Introduction

Since the realisation of ultrashort laser pulses there has been much interest in accurately retrieving their temporal intensity distribution. Ultrashort laser systems readily produce pulses with a pulse duration that is too short to be directly measured with even the fastest photodiodes. Therefore, indirect autocorrelation methods are used to estimate the laser pulse duration, where the pulse interacts with itself and the time delay between two copies of the pulse is varied. However, autocorrelation methods intrinsically cannot provide the full pulse information, that is, spectral resolution is needed to retrieve the spectrum and time-dependent phase of the pulse.

One of the most investigated and commonly used techniques to characterize ultrashort laser pulses is frequency-resolved optical gating (FROG) [72, 73]. In a FROG measurement two ultrashort laser pulses are combined in a nonlinear medium. The spectrum of the nonlinear signal, generated via parametric optical processes, is recorded as a function of the time delay between the pulses, resulting in a FROG trace that contains both spectral and temporal information. FROG has been implemented using different optical setups and nonlinear processes including collinear setups, where the laser beam paths overlap, for second-harmonic generation (SHG) [74] and third-harmonic generation (THG) [75] and non-collinear setups [76]. In an autocorrelation FROG measurement two copies of the same pulse are combined inside a nonlinear medium. Alternatively, in a cross-correlation FROG measurement a known reference pulse is combined with an unknown pulse to generate nondegenerate signals such as sum-frequency generation (SFG) or four-wave mixing (FWM) [77–80].

To retrieve the pulse information of two unknown ultrashort pulses at different frequencies, the measurement of a FROG trace based on a single nondegenerate nonlinear process will not contain enough information. Therefore, cross-correlation measurements using nondegenerate nonlinear processes depend on an, a priori, known reference pulse. With this method, a full characterization of two individual pulses still involves two measurements: an autocorrelation FROG measurement to retrieve the intensity distribution and phase of the reference pulse and the actual cross-correlation FROG measurement. The pulse shapes of two independent laser pulses can be retrieved using multiple FROG traces based on different nondegenerate processes that are simultaneously measured [81–83].

The most commonly used nonlinear media in FROG systems are nonlinear crystals, due to their high nonlinear coefficients and broad frequency range of transparency. However, phase-matching requirements have to be satisfied in these nonlinear crystals, which can make experimental implementation difficult and restrict the frequency range of applicability, making simultaneous measurements of different nonlinear processes impractical. Nonlinear surface processes have a shorter interaction length and can overcome these phase-matching requirements. Therefore, nonlinear media with a large nonlinear surface response provide a route to generate and exploit multiple nonlinear processes simultaneously. The nonlinear surface response of plasmonic nano-antennas has been used for ultrashort pulse characterization [83]. Atomically thin transition-metal dichalcogenide (TMDC) materials also show a remarkable high nonlinear surface response [27, 28, 60], along with an increase in absorption for photon energies above the semiconductor bandgap [84]. In addition to the background-free signals and the broad-

band nonlinear response, TMDCs are also very promising materials for ultrashort pulse characterization due to their large atomically flat surface, which allows for easy beam alignment and transmission measurements. Since WS_2 and related TMDC materials have large nonlinear susceptibilities over the whole visible wavelength range, they can be used to characterize laser pulses with a wide variety of wavelengths. Different types of TMDC monolayer or multilayer materials with different bandgap energies such as WSe_2, MoS_2 and $MoSe_2$ could be selected depending on the wavelength of the ultrashort laser pulses and nonlinear processes employed to generate the FROG trace. Furthermore, different combinations of nonlinear FROG signals can be selected depending on the characterization demands at hand, specifically those related to the laser wavelengths. The nonlinear signals generated in WS_2 could be further and selectively enhanced using more complex layered WS_2 structures [85, 86] or combining WS_2 with plasmonic nanostructures [87]. Recently, FROG characterization of a single pulse using the SHG process has been preformed on a WS_2 monolayer [88].

Next to its atomic thickness, WS_2 monolayer has another interesting property as a nonlinear medium that can be exploited for ultrashort pulse retrieval. The nonlinear generation of excitons can be potentially utilized in an autocorrelation measurement as its spectral width remains constant. The radiative recombination of these excitons to the ground state can be observed as a photoluminescence (PL) signal [60].

In this chapter, we exploit the high nonlinear response of a WS_2 monolayer over a broad spectral range to characterize two ultrashort laser pulses by measuring the FROG traces based on the SHG, SFG and FWM nonlinear processes. The spectra of the SFG and FWM processes are simultaneously recorded as a function of the time delay between two pulses with different wavelengths using a collinear optical setup. With a newly developed adaptation of the double-blind FROG algorithm, we precisely retrieve the pulse shapes of the two laser pulses at two different wavelengths, E_1 and E_2, using the experimental FROG traces based on FWM and SFG that were simultaneously measured. We validate the pulse shape of one of the fundamental pulses using a separate SHG FROG measurement and by utilizing autocorrelation traces generated via nonlinear photoluminescence.

4.2. THEORY

In order to retrieve the complex pulse shapes E_1 and E_2 from nondegenerate FROG traces, we use iterative retrieval algorithm based on the common pulse retrieval algorithm (COPRA), recently developed by Geib et al. [89]. The nonlinear process spectra of a measured non-collinear FROG trace can be defined as [90]:

$$I_{\text{FROG}}(\tau,\omega) = |\mathscr{F}\{\mathscr{S}_\tau[E(t,\omega)]\}|^2. \tag{4.1}$$

Here, the frequency, ω, and the time delay, τ, are the parameters over which the measurement trace is evaluated. $E(t,\omega)$ is the electric field of the laser pulse, $\mathscr{S}_\tau$ is the signal operator that depends on the nonlinear process and $\mathscr{F}$ is the Fourier transform operator. Although we use a collinear measurement scheme, the nondegenerate signals are background-free and thus collinear and non-collinear FROG traces are the same and therefore equation 4.1 still holds. The signal operators for the SFG ($\omega_{\text{SFG}} = \omega_1 + \omega_2$) and

FWM ($\omega_{\text{FWM}} = 2\omega_1 - \omega_2$) processes as observed in our experiment, where the delay time of E_2 is varied with respect to E_1, can be derived as:

$$\mathscr{S}_{\tau,\text{SFG}} = E_1(t)E_2(t-\tau) \quad \text{(SFG)} \quad \text{and} \tag{4.2}$$

$$\mathscr{S}_{\tau,\text{FWM}} = E_1(t)E_1(t)E_2^*(t-\tau) \quad \text{(FWM)}. \tag{4.3}$$

The COPRA algorithm optimizes the pulses E_1 and E_2 so that the calculated FROG trace I matches the measured trace, I_{meas}, as a nonlinear least squares problem, further described in Geib *et al.* [89]. For a nondegenerate cross-correlation retrieval algorithm one of the pulses is optimized while the second pulse acts as a reference pulse. In this work, we modified the COPRA retrieval algorithm to optimize the pulse E_1 or E_2 for both experimental traces, $I_{\text{meas, SFG}}$ and $I_{\text{meas, FWM}}$, while the second pulse is acting as the reference pulse, further described in section 4.6.1.

In order to simultaneously retrieve two unknown pulses E_1 and E_2, we utilize an iterative optimization scheme. Here, we start with two Gaussian pulses with central wavelengths λ_1 and λ_2 as our initial guess. Next, we start optimizing E_1 for $I_{\text{meas, SFG}}$ and $I_{\text{meas, FWM}}$, while keeping E_2 as a fixed reference pulse. Since an initial guess of E_2 is used as a reference pulse the pulse retrieval of E_1 is not completed but the retrieved pulse shape of E_1 is still a better approximation than the initial guess. In the next step, the newly retrieved approximation of E_1 is used as a reference pulse in the retrieval of E_2 resulting in a better approximation of E_2. This process is iterated until improvement of the normalized trace error between the measured and the retrieved FROG trace between iterations falls below a predefined value.

4.3. Experiment and methods

In this work, we retrieve the pulse intensity distribution and phase of two femtosecond laser pulses with different central wavelengths. A femtosecond laser oscillator (Spectra-Physics Tsunami) generates pulses with a central wavelength of 775 nm. Part of this laser beam is used as our first laser pulse while a fraction of it is used to pump an optical parametric oscillator (Spectra-Physics, Opal) that delivers the second laser pulse at 1200 nm. The pulse distributions of the 775 nm and 1200 nm laser pulses are retrieved by simultaneously measuring two cross-correlation FROG traces based on SFG and FWM signals using the optical setup sketched in fig. 4.1(a). In addition to the nondegenerate FROG traces, we also measure the SHG FROG trace of the 1200 nm beam, in order to validate the retrieved pulses from the cross-correlation FROG characterization. We measure the SHG signal, generated by two copies of the 1200 nm beam created by a beamsplitter, using a collinear autocorrelation FROG setup, as shown in fig. 4.1(b).

In both optical measurement schemes, motorized delay stages are used to control the time delay between the two laser pulses before focusing the beams on a WS_2 monolayer flake using a microscope objective (Olympus UPlanSapo) with a numerical aperture of 0.95. The WS_2 monolayer is mechanically exfoliated from commercially available bulk WS_2 onto a glass substrate, see also [60] and section 2.2. The emitted nonlinear signals from the WS_2 monolayer are collected by the same objective and pass trough a dichroic mirror and bandpass filters to filter the reflected fundamental light. The spectra of the nonlinear signals have been measured with a high-sensitivity cooled CCD-based
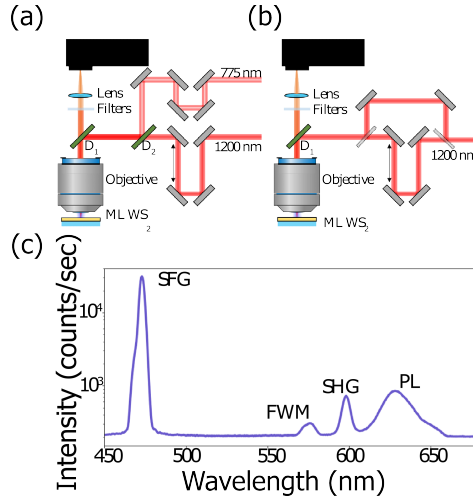
Figure 4.1: (a,b) Schematic representations of the optical setups. In (a) two laser pulses with wavelengths of 775 nm and 1200 nm are combined in a cross-correlation scheme to investigate nondegenerate nonlinear processes. In (b) two pulses with a wavelength of 1200 nm are combined in an autocorrelation scheme to investigate the degenerate nonlinear SHG process. (c) The measured nonlinear spectrum using the cross-correlation optical setup shown in (a) plotted on a logarithmic scale.

spectrometer (SpectraPro 2300I). Figure 4.1(c) depicts a spectrum measured using the cross-correlation setups shown in fig. 4.1(a) at a zero time delay between the fundamental pulses. This spectrum contains the nondegenerate signals of the SFG process around 470 nm, where $\omega_{SFG} = \omega_{775} + \omega_{1200}$, and FWM process around 572 nm, where $\omega_{FWM} = 2\omega_{775} - \omega_{1200}$. In addition, a peak can be seen around 600 nm originating from the second harmonic of the 1200 nm pulse, where $\omega_{SHG} = 2\omega_{1200}$. These nonlinear signals are well studied in WS_2 and other 2D layered materials [27, 60]. Finally, a broader peak around 625 nm is observed, which can be attributed to the PL signal of the WS_2 monolayer. Note that the fundamental laser pulses with wavelengths of 775 nm and 1200 nm have a photon energy that is below the bandgap of a WS_2 monolayer. With these wavelengths the bandgap can only be excited via multi-photon excitation. Therefore, the PL signal observed here is emitted by nonlinearly generated excitons.

The nonlinear spectra are recorded for several time delays between the pulses to obtain the experimental FROG traces with an exposure time of 1 second. Here we use optical powers of 2.4 mW for the 1200 nm laser beam and an optical power of 22.6 mW for the 775 nm beam that are below the damage threshold of the WS_2 monolayer. The power dependency on the nonlinear response is more extensively describe in J. Hernandez-Rueda et al. [60]. For both setups the time delay is created by a motorized delay line in the beam path of the 1200 nm with spatial delay steps of 400 nm, equivalent to ~ 1.3 fs. The spectrometer is calibrated by a rigid shift of the recorded spectrum. To reduce experimental noise, we fit a Gaussian shape over the nonlinear signals and afterwards we interpolated the data onto a 1024 by 1024 matrix for the pulse retrieval algorithm.

The top row of fig. 4.2 displays false colour maps of the experimentally measured

traces based on the FWM, SFG and SHG nonlinear processes. On the x-axis the wavelength of the nonlinear spectrum is plotted and on the y-axis the delay time between the two laser pulses. The top left and middle panels depict the FWM and SFG traces that are simultaneously collected from the same spectrum for each time delay using the optical setup sketched in fig. 4.1(a). For both the experimentally measured FWM and SFG traces an asymmetric pattern over the delay time can be observed. This asymmetric pattern indicates a frequency shift over the duration of at least one of the pulses, also referred to as pulse chirp. Interestingly, a chirped pulse signal can be easily identified using nondegenerate FROG traces because the nonlinear frequency shifts over the delay time, while degenerate FROG traces are symmetric over the delay time and a chirped signal can only be deduced from the time-bandwidth product of the trace. The top right panels in fig. 4.2 depict the measurement trace based on the SHG nonlinear process which is measured independently using the optical setup sketched in fig. 4.1(b). The SHG trace indeed shows a symmetric pattern over time delay.

4.4. Results and discussion

4.4.1. Pulse retrieval

The collected FROG traces of the SFG and FWM processes can now be used to extract the pulse intensity distribution and phase, E_1 and E_2, using the algorithm described in the theory section. We initialize the pulse retrieval routine using two guess pulses with a Gaussian intensity distribution in the frequency domain, with a preset bandwidth of ~ 16.7 nm full width at half maximum (FWHM) and central wavelengths at 775 nm and 1200 nm. We first retrieve E_1 with E_2 as a reference pulse and then retrieve E_2 using E_1 as a reference pulse and iterate these two retrieval algorithms 15 times.

In fig. 4.2, the calculated traces from the retrieved pulse shapes of the FWM and SFG processes are presented below the experimental traces of the same processes. Good qualitative agreement can be observed between the measured and the calculated traces in fig. 4.2. To quantify the error of the retrieved FROG traces, we use the normalized root mean square trace error, R, that can be calculated from the measurement and retrieved traces. This normalized trace error is equivalent to the commonly used FROG error, see [89] for more details.

The retrieved traces have a normalized error of 0.3% for both the FWM and SFG processes. In fig. 4.3 the retrieved complex temporal and spectral distributions of the two initial pulses are plotted. We observe a quadratic spectral phase signal in both the 775 nm and 1200 nm pulse, commonly referred to as chirp. From fig. 4.3 it can be seen that the 775 nm pulse exhibits a more pronounced chirp signal. The chirp in both laser pulses is most likely caused by the various optical elements included in the optical setup and the laser system, i.e. the microscope objective which can be replaced by off-center parabolic mirrors in order to reduce the amount of chirp. We retrieve a longer pulse duration for the 775 nm pulse of 389 fs FWHM compared to the pulse duration of the 1200 nm of 115 fs FWHM.
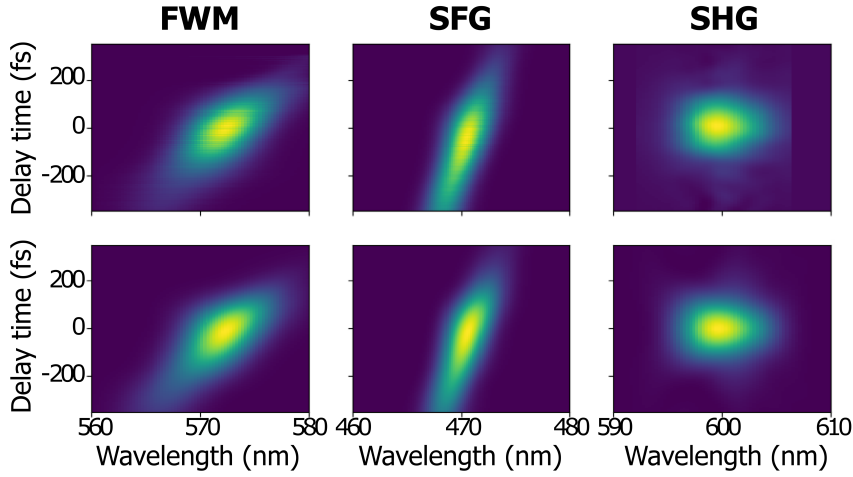
Figure 4.2: The top row displays the experimental FROG traces, where the FWM (left), SFG (middle) and SHG (right) signals are presented as function of wavelength and time delay. The FWM and SFG FROG traces are simultaneously collected using the cross-correlation measurement scheme, shown in fig. 4.1(a). The SHG spectra are collected using an auto-correlation setup, see fig. 4.1(b). The bottom row displays the calculated FROG traces from the retrieved pulse shapes. For the FWM and SFG calculated FROG traces both pulses where retrieved from the FWM and SFG measurement traces using an iterative cross-correlation FROG algorithm. For the SHG calculated FROG trace the 1200 nm pulse is retrieved from the SHG measurement trace using an auto-correlation FROG algorithm.
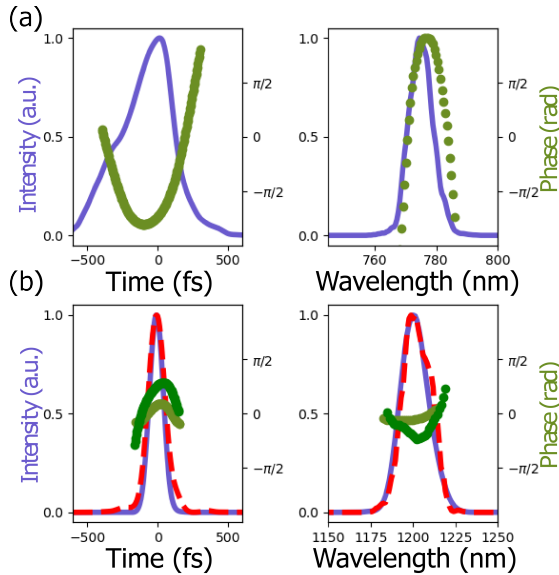
Figure 4.3: Retrieved temporal and spectral intensity distributions and phase of the ultrashort laser pulses at 775 nm (a) and 1200 nm (b). The pulse distributions plotted in purple (intensity) and light green (phase) are retrieved from the FWM and SFG measurement traces using an iterative cross-correlation FROG algorithm. The separately retrieved pulse distribution of the 1200 nm pulse from the SHG measurement trace using an auto-correlation FROG algorithm is plotted as a dashed red line (intensity) and dark green (phase).

To verify the validity of our results, we also measured an SHG FROG trace of the 1200 nm beam separately using the setup described in fig. 4.1(b). The interference between the second harmonic of the two copies of the 1200 nm beams, caused by the collinear setup, is digitally filtered out to retrieve the FROG trace of a non-collinear setup, similar to the method employed by Janische *et al.* [88]. Now, a non-collinear SHG FROG algorithm can be used to retrieve the pulse shape of the 1200 nm pulse. The right most panel of fig. 4.2 depicts the measured and retrieved trace of the SHG process. In the bottom part of fig. 4.3 the temporal and spectral distribution of the intensity and phase of the retrieved 1200 nm pulse are presented. A good resemblance of intensity distribution and phase between the retrieved pulses using SHG and SFG/FWM nonlinear signal can be observed in fig. 4.3b. The retrieved pulse duration of 140 fs FWHM using SHG FROG is also similar to the 115 fs FWHM pulse duration obtained with the nondegenerate FROG measurement. In conclusion, we retrieve the pulse shapes of both laser pulses using the FWM and SFG FROG traces. The pulse shape of the 1200 nm beam determined in this way is reproduced with an independent FROG measurements using the SHG process in monolayer WS_2.

4.4.2. NONLINEAR PHOTOLUMINESCENCE

Nonlinear excitation pathways similar to those in SFG, SHG and FWM mechanisms can mediate the generation of excitons, through non-parametric processes. For frequencies above the bandgap light is absorbed, subsequently the radiative recombination of the A-exciton also causes the characteristic photoluminescence signal at 625 nm, as can be observed in fig. 4.1(c). Note that the bandgap acts as an effective low-pass filter for our technique. The excitons can only be excited by multiphoton absorption (i.e. $2\omega_{1200}$, $2\omega_{775}$, $\omega_{1200}+\omega_{775}$, $2\omega_{775}-\omega_{1200}$) because the photon energies at the fundamental wavelengths are smaller than the exciton bandgap [26, 60, 91]. The intensity of the photoluminescence therefore also changes with the time delay between the laser pulses due to the contribution of nondegenerate multiphoton excitation pathways, allowing for a direct (cross)correlation measurements.

In fig. 4.4(a) the experimental trace of the PL signal is shown which is measured using the nondegenerate cross-correlation layout, where both 775 nm and 1200 nm beams are focused on the WS_2 monolayer sample, illustrated in fig. 4.1(a). Figure 4.4(b) depicts the projection of the measurement trace in fig. 4.4(a) along the wavelength axis. The PL signal at zero time delay can be attributed to the generation of excitons from a combination of degenerate excitation pathways (i.e. $2\omega_{1200}$, $2\omega_{775}$) and nondegenerate excitation pathways (i.e. $\omega_{1200}+\omega_{775}$, $2\omega_{775}-\omega_{1200}$). For long time-delays, for which the individual pulses do not overlap in time, the PL signal is solely generated by degenerate multiphoton absorption mechanisms.

Figures 4.4(c) and (d) present the PL measurement trace using the setup sketched in 4.1(b) and its integration over wavelength, where two sub-pulses of the 1200 nm beam are used. Because of the collinear setup, the SHG measurement trace exhibits interference fringes and since the excitons are now generated solely by the nonlinear processes the fringes are also present in the PL signal, see fig. 4.4(d). The period of these fringes agrees well with the 1200 nm wavelength of the initial laser beam. The DC component of the photoluminescence signal generated by the two photon absorption is plotted as a

red line in fig. 4.4(d) and can be understood as an effective SHG autocorrelation signal of the 1200 nm laser pulse. From the DC component, we extract a FWHM value, $\Delta\tau_A^{\mathrm{FWHM}}$, of 227 fs. This corresponds to pulse duration, $\Delta\tau_p^{\mathrm{FWHM}}$, of 161 fs assuming a Gaussian pulse distribution of the 1200 nm pulse. This pulse duration is in close agreement with the pulse duration extracted from the nondegenerate FROG method and the SHG FROG method.
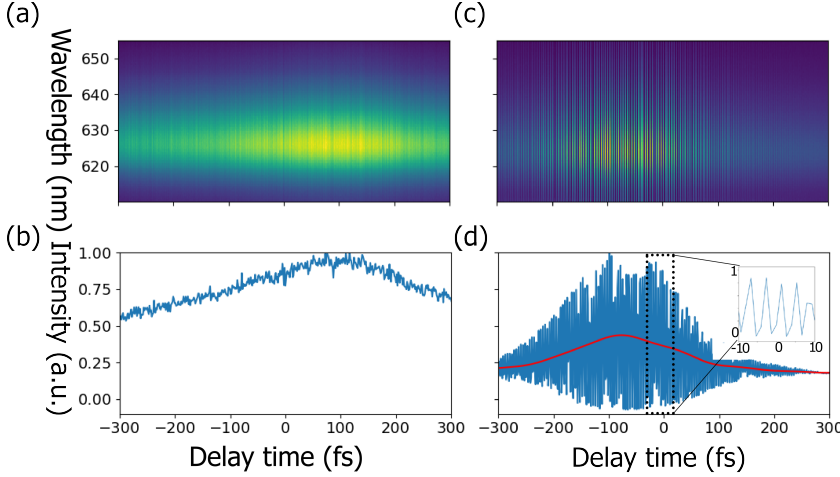

Figure 4.4: Experimental traces based on photoluminescence signals, where the PL signal is recorded using a nondegenerate measurement scheme (a), see fig. 4.1(a) and degenerate measurement scheme (c), see fig. 4.1(b). In (b) and (d) the projections over the wavelength axis are plotted for the measurement traces in (a) and (b), respectively. In (d) the interference pattern between the two 1200 nm beams is visible where in red the DC component of the PL signal is plotted.

4.5. CONCLUSIONS

We have exploited the broadband nonlinear response of an atomically thin WS_2 monolayer due to its relaxed phase matching conditions for ultrashort pulse characterization. Using a collinear optical setup, we measure both degenerate (SHG) and nondegenerate (FWM, SFG) nonlinear signals simultaneously by illuminating monolayer WS_2 with ultrashort laser pulses at two different wavelengths. We measure the nondegenerate nonlinear signals as a function of the time delay between the laser pulses to preform collinear (cross-)correlation FROG measurements. Using a novel adaptation of the FROG algorithm we retrieve the complex pulse distribution of both laser pulses. Agreement is found between the retrieved pulses from the degenerate and nondegenerate FROG retrieval methods. We demonstrate the advantages of simultaneous measurement of multiple nonlinear processes for ultashort pulse characterization facilitated in 2D materials. In addition to the nonlinear parametric signals, we also measure the nonlinearly generated PL signal from the WS_2 monolayer. The high nonlinear surface response over a broad range of wavelengths on an atomically thin layer allows for the implementation of novel retrieval methods simultaneously using multiple (non)degenerate nonlinear sig-

nals and PL emission, i.e. by also recording the spatial chirp of the nonlinear spectrum [92].

4.6. Supplementary information

4.6.1. Nondegenerate gradients

In the manuscript we use the common pulse retrieval algorithm (COPRA) algorithm developed by Geib et al. [89] to retrieve the fundamental pulse shapes from the FROG traces based on sum-frequency generation (SFG) and four-wave mixing (FWM). We extended the algorithm to also work with nondegenerate nonlinear signals and optimize for the SFG and FWM traces simultaneously. Here, we elaborate on the modification made with respect to the work of Geib et al. [89]. For simplicity, we use the same formulation as the original paper. Here, $\tilde{E}_n(\omega)$ is the complex valued pulse envelope of the 775 nm and 1200 nm beams and $E_k(t)$ is its temporal counterpart. The time shifted 1200 nm pulse by the delay time τ is defined as,

$$A_{k,1200} = \mathscr{F}^{-1}[e^{i\tau\omega_{n,1200}}\tilde{E}_{n,1200}]. \tag{4.4}$$

The spectral and temporal pulse shapes are related by following discrete Fourier transforms (DFT):

$$\tilde{E}_n = \mathscr{F}(E_k) \equiv \sum_k D_{nk}E_k \quad \text{with} \quad D_{nk} = \frac{\Delta t}{2\pi}e^{i\omega_n t_k} \tag{4.5}$$

$$E_k = \mathscr{F}^{-1}(E_n) \equiv \sum_n D_{kn}^{-1}\tilde{E}_n \quad \text{with} \quad D_{kn}^{-1} = \Delta\omega e^{-i\omega_n t_k}. \tag{4.6}$$

where Δt and $\Delta\omega$ are the time and frequency spacing respectively. Furthermore, the following relation between the DFT matrices is used:

$$D_{kn}^{-1} = \frac{2\pi\Delta\omega}{\Delta t}[D_{nk}]^*. \tag{4.7}$$

The COPRA retrieval algorithm calculates for each iteration the distance,

$$Z = |S^{'} - S(\tilde{E})|^2 \tag{4.8}$$

Where $S^{'}$ is the experimental FROG trace and $S(\tilde{E})$ is the calculated trace from the current solution $\tilde{E}$. $S(\tilde{E})$ for the nondegenerate nonlinear processes can be calculated in a similar way as degenerate noncollinear FROG traces (even if the a collinear setup is used).

$$\mathscr{S}_k(\tilde{E}) = A_{k,1200}E_{k,775} = \mathscr{F}^{-1}[e^{i\tau\omega_{1200}}\tilde{E}_{n,1200}]\mathscr{F}^{-1}[\tilde{E}_{n,775}] \quad \text{(SFG)} \tag{4.9}$$

$$\mathscr{S}_k(\tilde{E}) = A_{k,1200}E_{k,775}E_{k,775} = \mathscr{F}^{-1}[e^{i\tau\omega_{1200}}\tilde{E}_{n,1200}]\mathscr{F}^{-1}[\tilde{E}_{n,775}]\mathscr{F}^{-1}[\tilde{E}_{n,775}] \quad \text{(FWM)} \tag{4.10}$$

Now, to retrieve the next iteration complex electric field a single-gradient descent step is performed. In our case we want to optimize for the both the FWM and the SFG measurement trace.

$$\nabla Z_{total} = \nabla(Z_{FWM} + Z_{SFG}) \tag{4.11}$$

$$\nabla Z_{total} = \nabla Z_{FWM} + \nabla Z_{SFG} \tag{4.12}$$

As discussed in section 3 of the supplement information of [89] the derivation of ∇Z goes as,

$$\nabla Z = 2 \frac{\partial Z}{\partial \tilde{E}_n^*} \tag{4.13}$$

$$\nabla Z = -2 \sum_k \Delta S_k^* \frac{\partial S_k}{\partial \tilde{E}_n^*} + \Delta S (\frac{\partial S}{\partial \tilde{E}_n})^*. \tag{4.14}$$

Here $\Delta S_k = S_k' - S_k(\tilde{E})$. Using the above formulas, we will derive the gradient steps for the SFG and FWM nonlinear processes. Note that we need to evaluate the gradient step for the two cases where we optimize the 1200 nm with the 775 nm as a reference and visa versa separately. So in total we derive four gradient steps: ∇Z_{SFG} for optimization of the 1200 nm pulse, ∇Z_{SFG} for optimization of the 775 nm pulse, ∇Z_{FWM} for optimization of the 1200 nm pulse and ∇Z_{FWM} for optimization of the 775 nm pulse.

∇Z_{SFG} FOR OPTIMIZING 1200 NM BEAM
Combining equations 4.6 and 4.9 to calculate the partial derivatives of equation 4.14.

$$\frac{\partial S_k}{\partial \tilde{E}_{n,1200}^*} = 0 \tag{4.15}$$

$$\frac{\partial S_k}{\partial \tilde{E}_{n,1200}} = \frac{\partial}{\partial \tilde{E}_{n,1200}} A_{k,1200} E_{k,775}$$

$$\frac{\partial S_k}{\partial \tilde{E}_{n,1200}} = E_{k,775} \frac{\partial}{\partial \tilde{E}_{n,1200}} \sum_l D_{kl}^{-1} e^{i\tau\omega_{l,1200}} \tilde{E}_{l,1200}$$

$$\frac{\partial S_k}{\partial \tilde{E}_{n,1200}} = D_{kn}^{-1} e^{i\tau\omega_{n,1200}} E_{k,775} \tag{4.16}$$

Now we substitute equations 4.15 and 4.16 in equation 4.14,

$$\nabla Z_{\text{SFG}} = -2 \sum_k \Delta S_k [D_{kn}^{-1} e^{i\tau\omega_{n,1200}} E_{k,775}]^*$$

$$\nabla Z_{\text{SFG}} = -\frac{4\pi\Delta\omega}{\Delta t} e^{-i\tau\omega_{n,1200}} \sum_k D_{nk} \Delta S_{\tau,k} E_{k,775}^*$$

$$\boxed{\nabla Z_{\text{SFG}} = -\frac{4\pi\Delta\omega}{\Delta t} e^{-i\tau\omega_{n,1200}} \mathscr{F}[\Delta S_{\tau,k} E_{k,775}^*]} \tag{4.17}$$

∇Z_{SFG} FOR OPTIMIZING 775 NM BEAM
Combining equations 4.6 and 4.9 to calculate the partial derivatives of equation 4.14.

$$\frac{\partial S_k}{\partial \tilde{E}_{n,775}^*} = 0 \tag{4.18}$$

$$\frac{\partial S_k}{\partial \tilde{E}_{n,775}} = \frac{\partial}{\partial \tilde{E}_{n,775}} A_{k,1200} E_{k,775}$$

$$\frac{\partial S_k}{\partial \tilde{E}_{n,775}} = A_{k,1200} \frac{\partial}{\partial \tilde{E}_{n,775}} \sum_l D_{kl}^{-1} \tilde{E}_{l,775}$$

$$\frac{\partial S_k}{\partial E_{n,775}} = D_{kn}^{-1} A_{k,1200} \tag{4.19}$$

Now we substitute equations 4.18 and 4.19 in equation 4.14,

$$\nabla Z_{\text{SFG}} = -2 \sum_k \Delta S_k [D_{kn}^{-1} A_{k,1200}]^*$$

$$\nabla Z_{\text{SFG}} = -\frac{4\pi \Delta \omega}{\Delta t} \sum_k D_{nk} \Delta S_k A_{k,1200}^*$$

$$\boxed{\nabla Z_{\text{SFG}} = -\frac{4\pi \Delta \omega}{\Delta t} \mathscr{F}[\Delta S_k A_{k,1200}^*]} \tag{4.20}$$

∇Z_{FWM} FOR OPTIMIZING 1200 NM BEAM
Combining equations 4.6 and 4.10 to calculate the partial derivatives of equation 4.14.

$$\frac{\partial S_k}{\partial \tilde{E}_{n,1200}} = 0 \tag{4.21}$$

$$\frac{\partial S_k}{\partial \tilde{E}_{n,1200}^*} = \frac{\partial}{\partial \tilde{E}_{n,1200}^*} A_{k,1200}^* E_{k,775} E_{k,775}$$

$$\frac{\partial S_k}{\partial \tilde{E}_{n,1200}} = \frac{\partial}{\partial \tilde{E}_{n,1200}} \sum_l D_{kl}^{-1*} e^{-i\tau\omega_{l,1200}} \tilde{E}_{l,1200}^* E_{k,775} E_{k,775}$$

$$\frac{\partial S_k}{\partial \tilde{E}_{n,1200}} = D_{kn}^{-1*} e^{-i\tau\omega_{n,1200}} E_{k,775} E_{k,775} \tag{4.22}$$

Now we substitute equations 4.21 and 4.22 in equation 4.14,

$$\nabla Z_{\text{FWM}} = -2 \sum_k \Delta S_k^* [D_{kn}^{-1*} e^{-i\tau\omega_{n,1200}} E_{k,775} E_{k,775}]$$

$$\nabla Z_{\text{FWM}} = -\frac{4\pi \Delta \omega}{\Delta t} e^{-i\tau\omega_{n,1200}} \sum_k D_{nk} \Delta S_k^* E_{k,775} E_{k,775}$$

$$\boxed{\nabla Z_{\text{FWM}} = -\frac{4\pi \Delta \omega}{\Delta t} e^{-i\tau\omega_{n,1200}} \mathscr{F}[\Delta S_k^* E_{k,775} E_{k,775}]} \tag{4.23}$$

∇Z_{FWM} FOR OPTIMIZING 775 NM BEAM
Combining equations 4.6 and 4.10 to calculate the partial derivatives of equation 4.14.

$$\frac{\partial S_k}{\partial \tilde{E}_{n,775}^*} = 0 \tag{4.24}$$

$$\frac{\partial S_k}{\partial \tilde{E}_{n,775}} = \frac{\partial}{\partial \tilde{E}_{n,775}} A_{k,1200}^* E_{k,775} E_{k,775}$$

$$\frac{\partial S_k}{\partial \tilde{E}_{n,775}} = \frac{\partial}{\partial \tilde{E}_{n,775}} A_{k,1200}^* \sum_l D_{kl}^{-1} \tilde{E}_{l,775} \sum_j D_{kj}^{-1} \tilde{E}_{j,775}$$

$$\frac{\partial S_k}{\partial \tilde{E}_{n,775}} = 2 D_{kn}^{-1} A_{k,1200}^* E_{k,775} \tag{4.25}$$

Now we substitute equations 4.24 and 4.25 in equation 4.14,

$$\nabla Z_{\text{FWM}} = -4 \sum_k \Delta S_k [D_{kn}^{-1} A_{k,1200}^* E_{k,775}]^*$$

$$\nabla Z_{\text{FWM}} = -\frac{8\pi \Delta \omega}{\Delta t} \sum_k D_{nk} \Delta S_k A_{k,1200} E_{k,775}^*$$

$$\boxed{\nabla Z_{\text{FWM}} = -\frac{8\pi \Delta \omega}{\Delta t} \mathscr{F}[\Delta S_{\tau,k} A_{k,1200} E_{k,775}^*]} \tag{4.26}$$

4

III

PLASMONIC MODES

5

PLASMON-INDUCED ENHANCEMENT OF NONLINEAR PROCESSES IN A DOUBLE-RESONANT GRATING

Nanostructured gratings in a metal surface can highly enhance nonlinear optical processes. The geometrical parameters that characterize a grating can be optimized to achieve intense near-fields, which in turn enhance the nonlinear optical signals. For a nonlinear process that involves multiple frequencies, like four-wave mixing (FWM), the optimization of grating parameters necessary to enhance the radiation incoupling for both frequencies is not trivial. Here we propose, compute and experimentally demonstrate a grating design that is resonant to two excitation frequencies and thus enhances the frequency mixing processes more efficiently. Second- and third-order nonlinear mechanisms are studied using two spatially and temporally overlapped laser pulses with different frequencies. Using our grating design we achieve an unprecedented nonlinear FWM enhancement factor of 7×10^3.

5.1. INTRODUCTION

The optical response of metal/dielectric interfaces has attracted attention in the field of nonlinear optics [93]. The limited penetration depth of light through a metal highly reduces the nonlinear interaction length and typically leads to a lower nonlinear optical response. However, the nonlinear optical signals from a metal/dielectric interface can be greatly enhanced by employing nanostructures such as periodic arrays of cavities [94–96] or gratings [97, 98] on a metal surface. When the geometrical parameters of such nanostructures match the wavelength of the incoming light plasmonic resonances can greatly enhance the local electric field near the surface increasing the nonlinear response [2, 99]. Due to the sensitivity of the nonlinear signal on the geometric properties nonlinear optics on a surface can be functionalized to probe nanoparticles [100, 101] or can be used for biosensing applications [102].

Various nonlinear optical effects that occur on a nanostructured gold film as a result of illuminating it with incident laser beams at two frequencies ω_1 and ω_2 include: SHG, $2\omega_1$ and $2\omega_2$, sum-frequency generation (SFG), $\omega_1 + \omega_2$, third harmonic generation (THG), $3\omega_1$ and $3\omega_2$ and FWM, $2\omega_1 - \omega_2$ and $2\omega_2 - \omega_1$. These nonlinear processes are further described in section 1.3.2. The nonlinear signals scale with incoming electric fields depending on the nonlinear process, e.g. the SHG nonlinear signal scales quadratically with the incoming electric field, while the FWM nonlinear signal depends on electric fields with two different frequencies and scales quadratically with one of them and linearly with the other.

The efficiency of nonlinear optical processes will increase strongly by enhancing the local electric field near the surface. Surface plasmons, exhibit high local electric fields near the interface. Therefore, coupling the incident light to surface plasmons will strongly enhance the electric near-field close to the metal surface [4]. A grating can be used to couple the incident laser light into different kinds of plasmons: localized surface plasmons (LSPs) and surface plasmon polaritons (SPPs) [103, 104]. First, we consider the coupling of the incoming laser light into LSP taking into account the geometry of an individual slit of the grating. The slits can be treated as a metal-insulator-metal cavity where the resonance condition depends on the depth and the width of the slits. Secondly, the coupling into the SPPs can be enhanced by optimizing the grating period. The coupling of the incident laser light into plasmon modes that results of illuminating a grating with laser light depends on the depth (d) and the width (w) of the individual slits and the grating period (Λ_g). Gratings that induce resonances have shown large enhanced FWM [98] and SHG [105] signals, when compared to the response of a flat metal interface.

The fact that the FWM generation efficiency depends on two laser frequencies makes the optimization of the grating parameters more intricate than for single-frequency based processes. Double-resonant enhancement of FWM processes have been shown in gold nano-antennas, which are resonant to the two frequencies of the incoming beams [106]. Also, double-resonant nanostructures have been demonstrated to enhance SHG, where the nanostructures are simultaneously resonant to the frequency of the incoming light and the frequency of the second harmonic [105, 107, 108]. The nanostructured gratings in the above-mentioned works were based on a geometry where individual grating slits were simultaneously resonant to two different wavelengths. Next to experimental demonstrations of double-resonant structures also theoretical simulations of nonlinear

optics in multi-resonant structures using 2D materials such as graphene shows promising results [109].

In this chapter, we numerically compute and experimentally demonstrate a double-resonant plasmonic coupling via the enhancement of the FWM nonlinear optical process using a double-resonant nanostructure design where two gratings individually resonant to a single frequencies are combined, as depicted in fig. 5.1(a). With finite-difference time-domain simulations (FDTD) simulations we study the near-field induced around the gratings using both laser frequencies. Using the simulations, we select optimal grating parameters to obtain a reliable nanostructure design that is fabricated with focused ion beam milling. We measure the nonlinear optical response of several gratings by using two laser pulses with different frequencies and observe FWM, SFG, SHG and THG nonlinear optical signals. We demonstrate the superior performance of the double-resonant grating on Au, reaching FWM yields three orders of magnitude larger than those measured at a flat air/Au interface. The FWM signals are readily observed by the naked eye.

5.2. Experiment and methods

For the experiments performed in this chapter, the samples were made using focused ion beam milling, further discussed in section 2.2.2. For each sample a 200 nm gold layer was deposited on a glass slide using e-beam evaporation. The gratings are then etched into the thin gold film using focused ion beam milling (Helios, G4 CX DualBeam). A scanning electron microscope image of a machined sample is presented in fig. 5.1(b) where the slits of alternating depth are clearly visible.

The optical nonlinear response of the nanostructured gratings is studied using the setup schematically depicted in fig. 5.1(c). We use a femtosecond laser oscillator (Spectra-Physics, Tsunami) that generates pulses at a wavelength of 775 nm. With a pulse duration of roughly 150 fs and an optical parametric oscillator (Spectra-Physics, Opal) that delivers pulses at 1200 nm. A delay line is used to synchronize both beams before focusing onto the samples using an objective lens (Olympus UPlanSApo) to near-diffraction limited spot sizes of approximately 2 μm. The same objective lens is used to collect the generated nonlinear light. Due to a finite numerical aperture of the objective lens (NA = 0.95) the nonlinear light is detected up to a maximum angle (72°). To filter out the fundamental wavelengths while transmitting the nonlinear light, we use a dichroic mirror and two band-pass filters (Thorlabs, FGB37M). The spectra of the nonlinear light is recorded with a high-sensitivity cooled CCD-based spectrometer (SpectraPro 2300I).
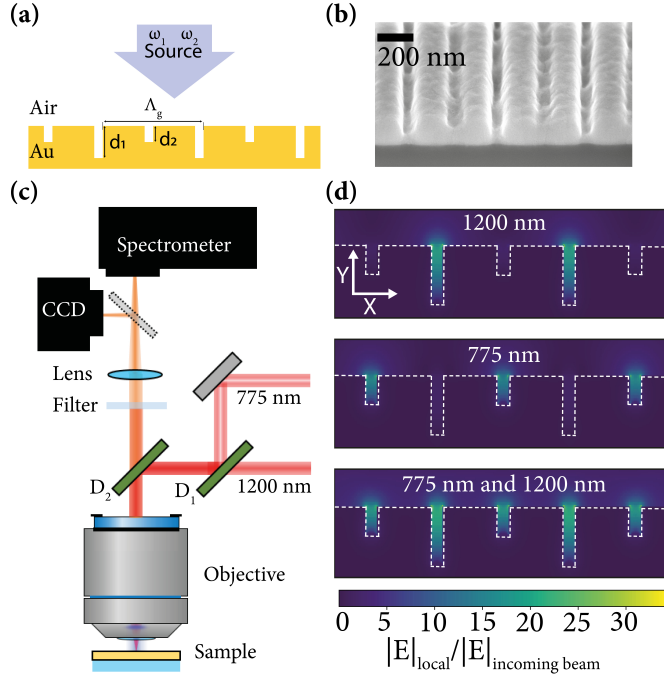
Figure 5.1: (a) Illustration of the double-resonant grating nanostructures gold sample. (b) Scanning electron microscope image of a cross-cut of the double grating nanostructure taken at an angle of 52°. (c) Schematic of the optical setup. (d) Finite-difference time-domain simulations of the electric field, normalized to the electric field of the incoming beams. In the top map the double resonant grating structure is illuminated with a wavelength of 1200 nm and probed at 1200 nm. In the middle map the grating structure is illuminated with a wavelength of 775 nm and probed at 775 nm. In the bottom map we illuminated the grating with both the 775 nm and 1200 nm beams, the local field is evaluated separately at both wavelengths afterwards these two images are merged together.

5.3. Results and Discussion

5.3.1. Numerical simulations of the electric near-field

Our double-resonant grating design combines two single-resonant gratings that are resonant for different frequencies. In order to find the optimal single-resonant grating parameters, w, d and Λ_g for which the individual gratings are resonant, we simulate the electric field around the grating using FDTD simulation [98]. First, we find only a minute dependence on the slit width for all frequencies with a decaying local field enhancement for larger slit widths. Therefore, the slit width is chosen to be $w = 40$ nm for both single-resonant gratings, the smallest slit width that can be fabricated in a reproducible manner. Secondly, we optimize the grating period and slit depth to maximize the near-field intensity as function of the frequency of the incoming light. The grating period is set to be equal for both single-resonant gratings to avoid some slits to overlap when the two gratings are combined. The grating period of $\Lambda_g = 470$ nm for both single-resonant gratings, is found to yield the optimal near-field enhancement upon 775 nm illumination.

We choose the optimal value for the beam at 775 nm since its contribution to the FWM intensity scales quadratically with the laser intensity, while it scales linearly for the laser intensity at 1200 nm. Lastly, we optimize the slits depth where the simulations show a large influence on the near-field intensity for different laser frequencies. Due to this strong near-field dependence on the grating depth, the depth of the slits is set differently for the two overlapping gratings. One grating has a depth of $d_1 = 75$ nm optimized for field enhancement at 775 nm and the other grating has a depth of $d_2 = 155$ nm optimized for field enhancement at 1200 nm.

After the optimization of the grating parameters of the single-resonant gratings for different wavelengths, we simulate the near-field around the double-resonant grating, which is the result of overlapping the single-resonant gratings optimized for a wavelength of 1200 nm and 775 nm. Figure 5.1(d) presents false color maps of the near-field enhancement factor, $\frac{|E|_{local}}{|E|_{incoming}}$, around the nanostructured gratings that we simulate using the FDTD method. When the double-resonant grating is illuminated only with the 1200 nm wavelength light source, we observe a local field enhancement (30×) in the 155 nm slits. For illumination with 775 nm, the local field enhancement (30×) occurs in the 75 nm slits. It should be noted that the off-resonant slits do not influence the local field enhancement of the resonant slits upon single wavelength excitation in the FDTD simulations. For example, when illuminating the double-resonant grating with only the 1200 nm light the local field enhancement in the resonant slits of $d_1 = 155$ nm is the same when the $d_2 = 75$ nm slits are not present. Finally, when both beams illuminate the hybrid grating structure, the simulations show local field enhancement in both slits. This indicates that the designed grating can be used to optimize the in-coupling of both wavelengths in order to enhance the nonlinear response.

While the double-resonant grating is optimized for the coupling to LSPs it also couples the incident light into SPPs. A grating couples light into SPP's when, $k_{SPP} = k_{inc} + mG$. Here, $k_{inc} = k_0 sin(\theta)$ is the wavevector component of the incident light parallel to the electric field. $k_0 = \omega/c$ is the wavevector in vacuum and θ is the angle of the incident beam. $k_{SPP} = k_0\sqrt{\epsilon_m(\omega)/(\epsilon_m(\omega)+1)}$ is the wavevector of the SPPs, where $\epsilon_m(\omega)$ is the real part of the dielectric constant of gold. m is an integer and $G = 2\pi/\Lambda_g$ is the wavevector of the grating. With $\Lambda_g = 470$ nm we calculate an angle of incidence of -38.7° for an incoming wavelength of 775 nm, well below the maximum angle of our objective (72°). For an incoming wavelength of 1200 nm there is no real angle for which the wavevector equation holds. This means we can only excite SPPs of 775 nm wavelength with the double-resonant grating given the NA of the objective used. fig. 5.2(a) presents false color map of the real part of the x component of the local electric field around the nanostructured grating that we simulate using the FDTD method. The grating is excited with 775 nm wavelength at an angle of -40°. This map illustrate the SSPs traveling on the gold surface when the double-resonant grating is illuminated under a -40° angle. In fig. 5.2(b) we used a FDTD simulation varying the angle of the incident beam and probing the local electric field 5 nm below the surface, 7.2μm away from the grating. The simulation in fig. 5.2(b) shows a peak at -40° for a 775 nm wavelength excitation and no peak for a 1200 nm wavelength excitation which is in good agreement with the calculated angles.
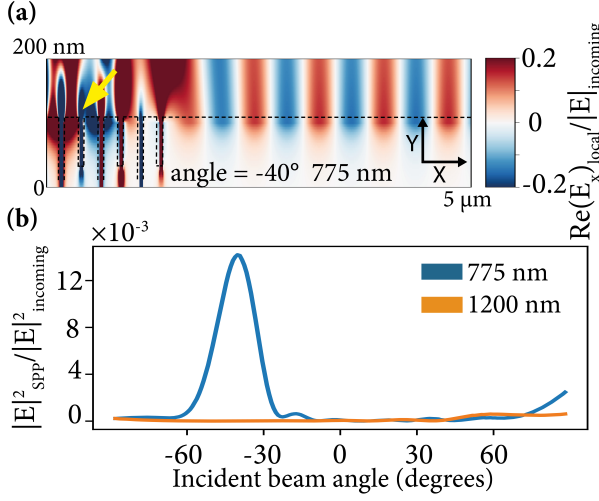
(a)

(b)

Figure 5.2: (a) Finite-difference time-domain simulation of the real part of the x component of the electric field, normalized to the electric field of the incoming beam. The grating is excited with a wavelength of 775 nm at a -40° angle (indicated with an arrow). (b) Normalized electric field as a function of incidence angle, determined 5 nm below the flat Au surface at 7.2μm from the edge of the grating at two incident wavelengths of 775 nm (blue line) and 1200 nm (orange line) respectively.

5.3.2. MEASUREMENT OF THE NONLINEAR PROCESSES AND THE ENHANCEMENT FACTORS

Figure 5.3(a) depicts the spectra collected from plain gold and the double-resonant grating (note that the intensity is measured in electrical counts of the spectrometer). The peaks in the spectra can be assigned to the nonlinear optical signals corresponding to FWM (572 nm), SFG (472 nm), $SHG_{775\,nm}$ (388 nm) and $THG_{1200\,nm}$ (400 nm). These spectra demonstrate a clear enhancement of all nonlinear processes on the designed grating when compared to that of the flat gold surface. Figure 5.3(b) presents the different signals as a function of the time-averaged (CW) power of the incident beams. The fact that in fig. 5.3(b), we use a double logarithmic scale makes monomial functions appear as straight lines in the plot. The slopes of these lines correspond to the power order. To further illustrate that the different nonlinear effects scales with the same power as predicted the nonlinear processes we fitted the data with monomial functions of the first (orange lines), second (blue lines) and third (pink line) order. We observe a linear behaviour of the SFG signal and a quadratic behaviour of the FWM and $SHG_{775\,nm}$ signals as a function of the power of the 775 nm beam. Similarly, a linear behaviour of the FWM and SFG signals and a cubic behaviour of the $THG_{1200\,nm}$ signal are observed as a function of the power of the 1200 nm beam.

We investigate the nonlinear enhancements of both the single- and double-resonant gratings as depicted in the inset of fig. 5.4. The spectra are presented in fig. 5.4. The enhancement factors of the nonlinear processes are obtained by dividing the peak intensities by the one measured on a flat gold interface. These factors are listed in Table 5.1. The single-resonant gratings exhibit FWM enhancement factors up to 1138 ($d_1 = 155$

(a)

(b)
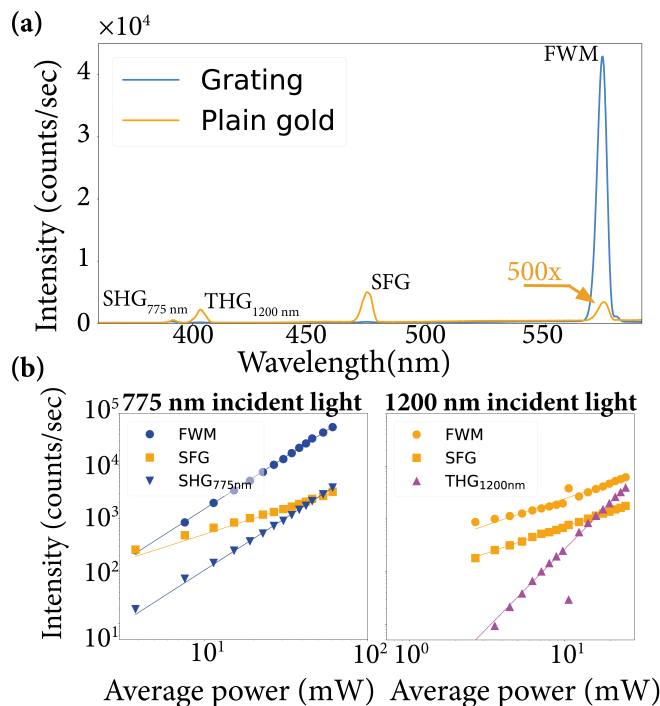
Figure 5.3: (a) Spectra of the generated signal on a gold surface (orange) and the double nanostructure grating etched in gold (blue). $SHG_{775\,nm}$, $THG_{1200\,nm}$, SFG and FWM are observed on plain gold and the nanostructure. (b) Double logarithmic plot of the intensity of the nonlinear signals in gold as a function of the power of the incoming beams. The power functions of the nonlinear effects appear as straight lines on the double logarithmic scale where the slope corresponds to the power order of the nonlinear effect. Linear (orange), quadratic (blue) and cubic (pink) monomial functions are fitted through the data points.
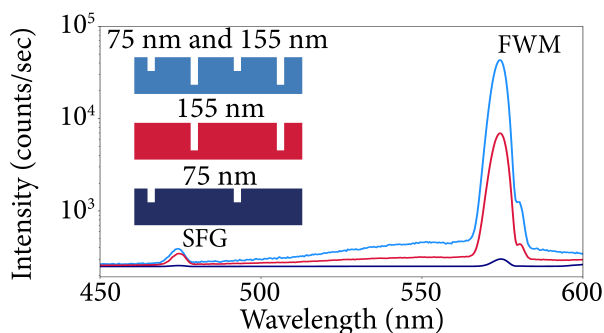
Figure 5.4: Semi-log plot of the spectra for the double grating nanostructure and the individual gratings. The inset shows an illustration of the measured gratings.

Enhancement	$d = 75$ nm and 155 nm	$d = 155$ nm	$d = 75$ nm
FWM	7302	1138	8.5
SFG	12	8.7	0.6

Table 5.1: Nonlinear optical enhancement of FWM and SFG nonlinear optical processes for the double grating and individual gratings.

nm) and 8.5 ($d_2 = 75$ nm). The double-resonant grating exhibits a remarkable enhancement factor of 7×10^3 for the FWM emission and an enhancement factor of 12 for the SFG emission. The observed enhancement in Table 1 demonstrates the superior performance of the double-resonant grating over the single-resonant gratings, as was expected from the near-field simulations using the FDTD method.

Furthermore, we measured the enhancement factors of the nonlinear processes depending on a single frequency i.e., $SHG_{775 nm}$ and $THG_{1200 nm}$, which are respectively 234 and 13 for the hybrid grating. Interestingly, these nonlinear processes also exhibit a higher enhancement using the hybrid grating. We also measured lower nonlinear enhancements in gratings with half of the period ($\Lambda_g = 235$ nm) and single slit depths (data not shown) to confirm that the large enhancement of the double-resonant grating is indeed not caused by the different grating period.

In contrast with previously studied double-resonant structures, our double-resonant grating enhances the incoming electric field at different spatial positions for the different frequencies. As a result, the overlap of the locally enhanced electric fields for the different frequencies is small. It is therefore not straightforward why the FWM and SFG nonlinear signals get enhanced by the double-resonant grating structure. Our results indicate an increased coupling to SPPs when the grating slits are resonant with the incoming wavelengths and that the nonlinear processes depending on two frequencies are mediated by the SPPs. Therefore the nonlinear enhancement of our double resonant grating structure is due generation of SPPs as well as LSPs. We will refer to the combination of LSPs as SPPs as surface plasmons.

5.3.3. EFFECTS FROM THE LINEAR POLARIZATION ANGLE

To further illustrate and test the effect of the grating on the nonlinear processes we investigate the dependency of the FWM and SFG enhancement on the angle between the linear polarization vectors of the beams. Maximum enhancement is obtained when all incident polarization directions are perpendicular to the grooves. To underpin the plasmon-mediated nature of the nonlinear processes, we measure the FWM and SFG for different angles between the polarization direction of the incident beams, see fig. 5.5(a) and (b). Figures 5.5(c) and (d) depict the FWM spectra collected from plain gold and from the double-resonant grating, respectively. Analogously, fig. 5.5(e) and (f) depict SFG spectra measured at the plain gold interface and at the double-resonant grating, respectively. The spectra are acquired for parallel (blue lines) or perpendicular (red lines) polarization directions. When illuminating plain gold with a perpendicular orientation between polarizations the resultant FWM signal is only a small fraction of the signal generated with a parallel orientation between polarizations as depicted in fig. 5.5(c). However, for the double-resonant grating the nonlinear signal of the perpendicular orientation between
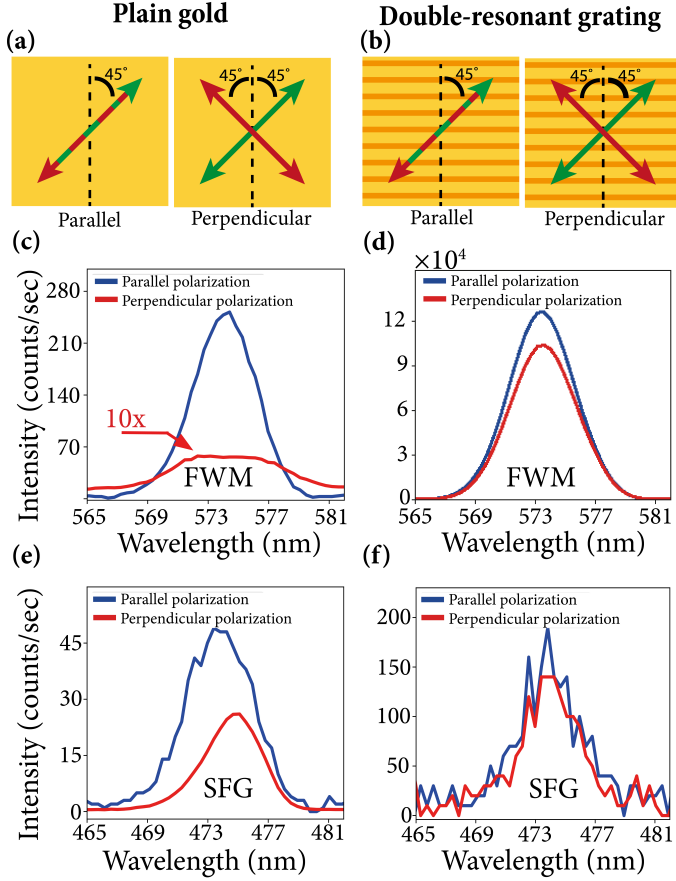
Figure 5.5: Nonlinear optical responses of FWM and SFG where the polarization angles of the incident beams are parallel and perpendicular aligned. The polarization angles used for the parallel and perpendicular alignments are depicted in (a) on plain gold and in (b) on the double resonant grating. The green arrow depicts the polarization angle of the 775 nm incident light and the red arrow the polarization angle of the 1200 nm incident light. In (c) and (d) the FWM nonlinear signal is plotted when illuminating the plain gold and the double-resonant grating, respectively. In (e) and (g) the SFG nonlinear signal is plotted when illuminating the plain gold and the double-resonant grating, respectively.

polarizations is almost the same as for the parallel orientation between polarizations, see fig. 5.5(d). The same amount of incident light is coupled into surface plasmons via the double-resonant grating because the electric field component perpendicular to the grating axis is the same for both polarization orientations. Therefore, the nonlinear signal generated by the surface plasmons do not decrease. The SFG on plain gold generated using the perpendicular orientation between polarizations illustrates that the nonlinear signal is roughly half of the nonlinear signal using the parallel orientation between polarizations, see fig. 5.5(e). Because of the centrosymmetry of the gold, the second-order nonlinear processes generated by the transverse component of the focused laser beams are very weak. Therefore, the second-order nonlinear signal generated by the longitudinal component of the tightly focused laser beams, directed out of the gold film, is more dominant than the transverse component. The longitudinal component is not affected by the orientation between the polarizations of the incoming beams. Therefore, the SFG nonlinear signal is not affected as much as the FWM signal by the orientation between polarizations of the incoming beams. On the double-resonant grating the SFG nonlinear optical signal behaves the same way as the FWM signal for parallel and perpendicular orientation between polarizations alignments.

5.4. CONCLUSION

In conclusion we demonstrate enhancements of second- and third-order nonlinear effects depending on multiple frequencies using a double-resonant grating design. In this double-resonant grating two gratings with different slit depths optimized for two different frequencies are combined. Local electric field enhancements generated in the double-resonant grating induce surface plasmons that generate second- and third-order nonlinear enhancements of several orders of magnitude. For the FWM nonlinear signal depending on two different incoming frequencies we observe an enhancement of 7×10^3 in the double-resonant grating.

6

DOUBLE NANOWIRE SYSTEM

Surface plasmon polariton modes propagating through a two-wire transmission line (TWTL) are promising for nanophotonic circuit applications due to their high spatial confinement. In this chapter, we investigate the near-field characteristics of the symmetric and anti-symmetric mode in a TWTL system using a phase-, amplitude-, and polarization-resolved near-field scanning optical microscope (NSOM). The measured field symmetries and intensity profiles closely resemble the calculated mode patterns. Furthermore, we observe selective wire excitation generated by a superposition of the symmetric and anti-symmetric modes. Finally, we experimentally observe the two plasmonic modes propagating through a TWTL filter design and Mach-Zehnder interferometer structure.

6.1. INTRODUCTION

Surface plasmon polaritons (SPPs) are promising information carriers to be applied in nanophotonic circuitry due to their high spatial confinement. At visible and telecom frequencies the main challenges of SPP-based circuits are the short plasmonic propagation lengths and the large wavevector mismatch with free-space light. Nonetheless, promising advances toward SPP-based nanophotonic circuit devices have been made in recent years [42, 59, 110–113]. Although, the function of most plasmonic devices is demonstrated in far-field experiments their function is determined by the local near-field characteristics of these plasmonic systems.

An interesting candidate for an SPP-based nanophotonic circuit is a two-wire transmission lines (TWTL) system. Such a TWTL system consists of two parallel metallic nanowires close together. While a single nanowire only has one Sommerfeld-like mode [114], in a TWTL the two single nanowire modes hybridize into two eigenmodes with a symmetric and anti-symmetric charge distribution. The symmetric and anti-symmetric plasmonic modes have been experimentally demonstrated at near-infrared [13] and visible [14] frequencies in a TWTL using far-field microscope techniques with an extended antenna to selectively couple the plasmonic modes back to far-field light at different spatial positions.

A TWTL system can be functionalized by implementing multiple nanocircuitry elements. Antennas at the ends of a TWTL can be designed to greatly improve the coupling to a superposition of the symmetric and anti-symmetric plasmonic modes. Depending on the linear polarization angle of the far-field light, θ, the plasmonic mode intensity can be steered in only one of the two arms of a TWTL using an antenna [115]. Different types of antennas have been proposed and demonstrated [13, 115–120]. A mode filter can be designed to selectively transmit only one of the modes. A Mach-Zehnder interferometer can be used to transform one mode into the other mode [12, 121, 122]. Besides pure optical schemes, recent studies show promising electro-optical effects in a TWTL system including electric excitation [123], modulation, [124, 125] and detection [126].

Near-field microscope techniques offer the opportunity to directly monitor and characterize the plasmonic modes. A near-field scanning optical microscope (NSOM) uses a sub-wavelength probe in close proximity to a plasmonic structure to locally couple the evanescent field of the plasmonic mode to the far field. Scattering NSOMs use a metallic probe to scatter predominately the out-of-plane electric component of the plasmonic mode to a far-field mode in air. These microscopes have been used to observe the near-infrared frequency excitation of the anti-symmetric mode [11, 127, 128] of a TWTL as well as the plasmonic mode in a metallic slot waveguide [15]. Collection NSOM uses a tapered fiber probe to couple the in-plane components of the plasmonic mode to polarized modes in the fiber. The near field of a single nanowire plasmonic mode at the telecom frequency has been carefully studied using an NSOM. [114, 129, 130].

In this chapter, we experimentally map the in-plane polarization-resolved optical near field of the plasmonic symmetric and anti-symmetric modes in a TWTL system with a collection NSOM. We characterize the properties of the local electric field of the symmetric and anti-symmetric modes. The measured near-field can also be used to explore the confined plasmonic mode behavior in nanocircuitry elements. Therefore, we study the local electric field of both plasmonic modes in three different nanocircuitry el-

ements: a coupling antenna, a mode filter, and a mode shifter. From the observations of the near field around the TWTL systems we extract useful insights into the design principles of nanophotonic TWTL systems.

6.2. Experiment and methods

The gold TWTL systems are fabricated on top of a glass substrate with an electron beam lithography-based lift-off process. A thin layer of 100 nm positive e-beam resist (AR-P6200.04) is spin-coated on top of a glass slide after which an extra layer of conductive coating (AR-PC 5090.02) is spin-coated. With e-beam lithography steps (Raith EBPG5200) the TWTL structures are etched into the resist layer. In the next step, 5 nm titanium, for adhesion purposes, and 50 nm gold are evaporated (Temescal FC2000) to the substrate and finally, the resist is removed during a liftoff process. The nanostructures are inspected using a scanning electron microscope (SEM). A thin layer (4 nm) of chromium is sputtered on top of the sample as a conductive layer for the SEM inspection and is subsequently removed before the optical experiments by a selective chromium etchant. Figure 6.1(a) displays an SEM image of a fabricated TWTL structure.

A schematic overview of the aperture-based phase- and polarization-resolved near-field optical microscope (NSOM), is displayed in fig. 6.1(b). The linear polarization of a telecom laser (1550 nm) is controlled by a half-wave plate and the laser beam is weakly focused on the TWTL structures from the glass side using a microscope objective (NA = .65) to couple light to plasmonic modes of the TWTL. A small fraction of the evanescent near field of the confined plasmonic modes is collected by an aperture-based probe, approximately 20 nm from the surface, at the air side of the TWTL structures. The perpendicular electric field components collected from the fiber are split using a polarizing beamsplitter and measured with detectors 1 and 2 each resulting in the lock-in signals L_1 and L_2 [46]. L_1 and L_2 result from the interference between the signal and reference branch and can be written as $L_{1,2} = A_{1,2} e^{i\phi_{1,2}}$, where A is the local amplitude and ϕ is the phase difference between the signal and reference branch obtained by combing the information of the output channels of the lock-in amplifiers. Scanning the NSOM probe over the sample we obtain the local electric field distribution of the plasmonic modes in the TWTL system. Using digital Fourier filtering, free-space light contributions can be removed and the backward and forward propagating mode can also be separated [131].
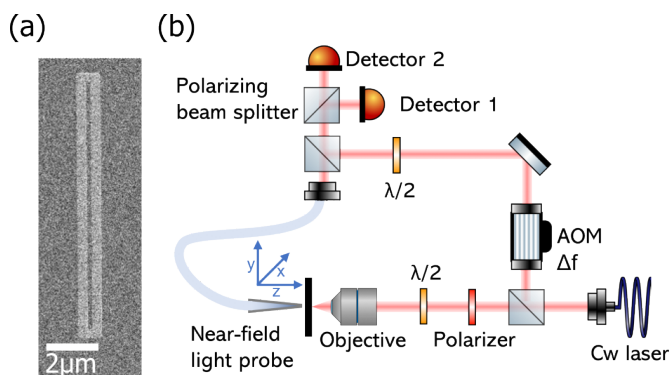
6

Figure 6.1: (a) Scanning electron microscope image of the fabricated TWTL devices. (b) Schematic overview of the experimental near-field scanning optical microscope setup.

6

6.3. RESULTS AND DISCUSSION

6.3.1. THE NEAR-FIELD OF THE (ANTI-)SYMMETRIC PLASMONIC MODES

Figure 6.2(a) displays the real part of the measured lock-in signals L_1 and L_2. The TWTL structure is excited at the top, where the wires are connected to serve as an antenna. For the top and bottom images in fig. 6.2(a) the TWTL is excited with a y- and x- polarization, respectively, generating the symmetric and anti-symmetric plasmonic mode, respectively. The measured signals are filtered in Fourier space $k_0 < k_y < 9.4 \ \mu m^{-1}$, where k_0 is the wavevector in vacuum, to select only the propagating plasmonic mode in the downward y-direction. From the real part of L_1 and L_2 in fig. 6.2(a) the oscillating signals along the TWTL are the plasmonic modes. Using a Fourier transform we extract an effective index of 1.50(0.03) for the symmetric mode and 1.53(0.03) for the anti-symmetric mode, close to the simulated effective index of 1.521 (symmetric mode) and 1.524 (anti-symmetric mode).

To further investigate the mode profiles of the measured L_1 and L_2 signals we calculate the local electric field of the symmetric and anti-symmetric plasmonic eigenmodes using eigenmode expansion simulation (Lumerical). The real part of the calculated x- and y-components of the electric field are displayed in fig. 6.2(b) for the symmetric mode and in fig. 6.2(c) for the anti-symmetric mode. When the symmetric mode is excited, the measured L_1 signal shows a higher mode intensity at the outsides of the two wires and the sign of the phase of the field changes between the left and right wire, as shown in the top left image of fig. 6.2(a). This closely resembles the x-component of the calculated local electric field for the symmetric mode. The measured data for the L_2 signal when the symmetric mode is generated shows the same phase for the left and right wires with a mode intensity mostly located directly above the wires, as shown in the top right image of fig. 6.2(a). This observation is in good correspondence with the calculated y-component of the symmetric mode. For the calculated anti-symmetric mode the phase symmetries are opposite to the symmetric mode. Here, the x-component has a symmetric field pattern located at the inside of the TWTL and the y-component has an anti-symmetric field pattern located on top of the wires, similar to the measured L_1 and L_2 signals when the anti-symmetric mode is excited, as shown in the bottom row of fig. 6.2(a). In summary, the distribution of the local field intensity and the phase symmetry differs between the symmetric and anti-symmetric modes and between the x- and y-component of the electric field. The symmetries and mode intensity locations of the calculated symmetric and anti-symmetric mode match well with the measured L_1 signal for the x-component of the field and the L_2 signal for the y-component.

Notice that the signal of L_2 with respect to L_1 is surprisingly large since the E_x contribution is notably larger than the E_y contributions for the symmetric and anti-symmetric mode in a TWTL system. We note that the NSOM probe has an additional pick-up of magnetic fields that contributes to the L_1 and L_2 signals, as described by Kabakova et al. for a single plasmonic wire [130]. The simulated magnetic mode profiles of the TWTL structure are provided in the supplementary information (fig. 6.6).

6
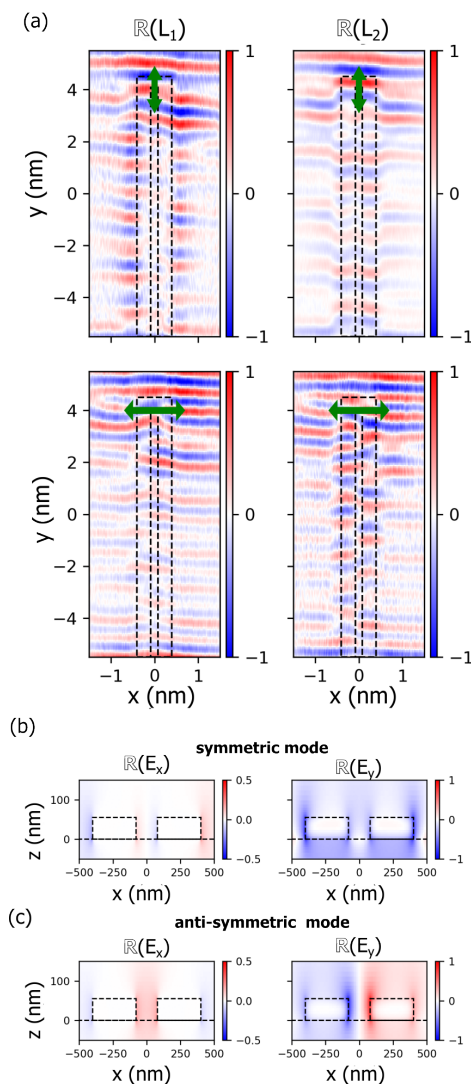
Figure 6.2: A false-color plot of the normalized real parts of the measured lock-in signals L_1 (left) and L_2 (right) measured of the symmetric (top) and anti-symmetric (bottom) plasmonic modes in a TWTL structure. The TWTL is excited at the top of the structure where the linear polarization direction is indicated by green arrows. The black dashed lines indicate the position of the TWTL structure. (b-c) The simulated real part of the x- and y-component of the local electric field for the symmetric (b) and anti-symmetric (c) mode profiles in a TWTL.
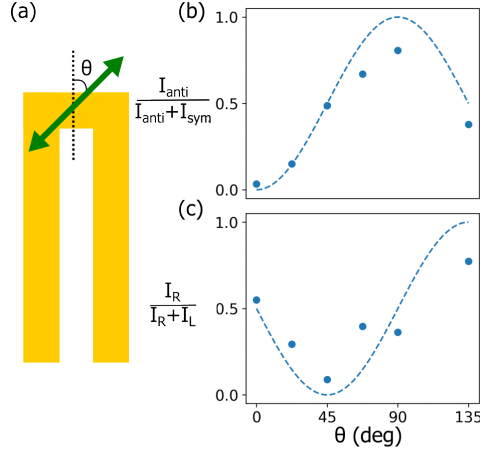
Figure 6.3: (a) Sketch of the TWTL antenna indicating the linear polarization angle θ. Normalized intensity of the anti-symmetric mode (b) and normalized intensity in the right wire (c) as a function of θ. The dashed lines indicate the expected intensities.

6.3.2. NEAR-FIELD CHARACTERIZATION OF OTHER TWTL SYSTEMS

Next, we inspect three elements of a plasmonic nanocircuitry system: an antenna element that couples the free-space light into the plasmonic modes, a filter element that filters one of the modes, and an interferometer design that shifts between the two modes.

First, we study the coupling from free-space light to the confined plasmonic modes using an antenna element that can excite a superposition between the symmetric and anti-symmetric mode by changing the far-field linear polarization angle θ, depicted in fig. 6.3(a). A superposition of the symmetric and anti-symmetric modes can then lead to a selective coupling of the plasmonic mode intensity to a single arm of the TWTL. However, the symmetric and anti-symmetric modes are still the proper eigenmodes of the TWTL system with different wavenumbers. Therefore, the effective plasmonic light intensity will oscillate between the right and left wire during propagation in the TWTL. With our near-field light probe, we can now directly map the generated spatial field distribution after the antenna and do not rely on the physical separation of the wires to measure the mode intensity of the single wires.

We measure the plasmonic near field in the TWTL for different incident linear polarization angles. The L_2 signal is used to calculate the normalized anti-symmetric mode intensity, $\frac{I_{\text{anti}}}{I_{\text{sym}} + I_{\text{anti}}}$ and the normalized intensity in the right wire, $\frac{I_R}{I_L + I_R}$. To separate the symmetric and anti-symmetric mode contributions we calculate the intensities of the odd and even contributions: $I_{\text{sym}} = |E_{\text{even}}|^2 = |(L_2 + L_{2,\text{mirr}})/2|^2$ and $I_{\text{anti}} = |E_{\text{odd}}|^2 = |(L_2 - L_{2,\text{mirr}})/2|^2$ [132]. Where L_{mirr} is the mirrored signal at the central axis along the TWTL. The intensity contribution of the left(right) wire is derived by calculating the average intensity on the area on top of the left (right) wire: $I_L = |L_{2,\text{left}}|^2$ and $I_R = |L_{2,\text{right}}|^2$.

The normalized anti-symmetric mode intensities are plotted in fig. 6.3(b) as function of θ. The plasmonic mode intensity varies between the symmetric and anti-symmetric

mode distribution where at $\theta = 0°$ mostly the symmetric mode is excited and the maximum excitation of the anti-symmetric mode is at $\theta = 90°$. The normalized mode intensities in the right wire are plotted in fig. 6.3(c) as function of θ. Again we observe an intensity fluctuation, but now the intensity maxima in the left and right wire appear at $\theta = 45°$ and $\theta = 135°$. At these far-field polarization angles, a superposition between symmetric and anti-symmetric modes is generated. This superposition causes constructive interference in one wire and destructive interference in the other wire. The expected mode intensity dependence on θ for an ideal antenna is plotted with the dashed line in fig. 6.3b and c. Deviations from the expected dependence on θ can be caused by the antenna properties η and δ. Here, η is the coupling efficiency ratio between the symmetric and anti-symmetric modes. This ratio shifts the polarization angle for which the symmetric mode and anti-symmetric mode have equal intensities. δ is the difference in temporal phase between the two excited modes. δ determines the maximum difference between the normalized intensities in the right and left wires, see also fig. 6.7 in the supplementary information. Comparing the data points in fig. 6.3(b) and (c) with the predicted curves, we conclude that the antenna experiences only a small η since the minima and maxima are close to $\theta = 45°$ and $\theta = 90°$. Furthermore, the antenna shows a small δ causing a not fully right and left normalized mode intensity at $\theta = 45°$ and $\theta = 90°$. The relationship between the normalized generated intensities as a function of θ and the antenna parameters η and δ is further explored in the supplementary information. Note that the normalized intensities can also be slightly influenced by cross-talk between the x- and y- field components in the measurement probe or by a small background signal causing deviations at $\theta = 0°$ and $\theta = 90°$ that do not depend on η and δ. Therefore, in order to remove more background signal from our data we use slightly stricter Fourier filtering restrictions where 5.03 $\mu m^{-1} < k_y < 7.54 \ \mu m^{-1}$. In summary, by changing the polarization angle and analyzing the near-field data of the generated modes, we observe good coupling control to the plasmonic modes and recognize a small dependence on the antenna properties.

In the next section, we will investigate another passive element, that is designed to selectively filter either the symmetric or the anti-symmetric mode. Such a mode filter element can be a useful component for plasmonic nanophotonic circuitry. In fig. 6.2 we observe that most of the symmetric mode intensity is located at the outside of the TWTL while most of the anti-symmetric mode intensity is located in between the wires. Therefore, we design two different wire structures to block either the exterior or the interior of the TWTL, sketched with white dashed lines in fig. 6.4. Both filter elements are placed 4 μm along the TWTL away from the antenna and extend for 1 μm. For the exterior filter, gold is placed at the outside of the TWTL for 3 μm, whereas for the interior filter gold is placed in between the wires.

In fig. 6.4 the absolute square of L_2 is plotted around TWTL filter systems, corresponding to the y-component of the electric field that is mostly located on top of the wires. Measurements performed on the exterior filter are plotted on the left and measurements on the interior filter are plotted on the right. We excite the TWTLs at an antenna at the top of the TWTL with the symmetric mode (top images) and the anti-symmetric mode (bottom images). In the plots of fig. 6.4, we digitally filter only the even and odd signals for the symmetric and anti-symmetric modes, respectively using

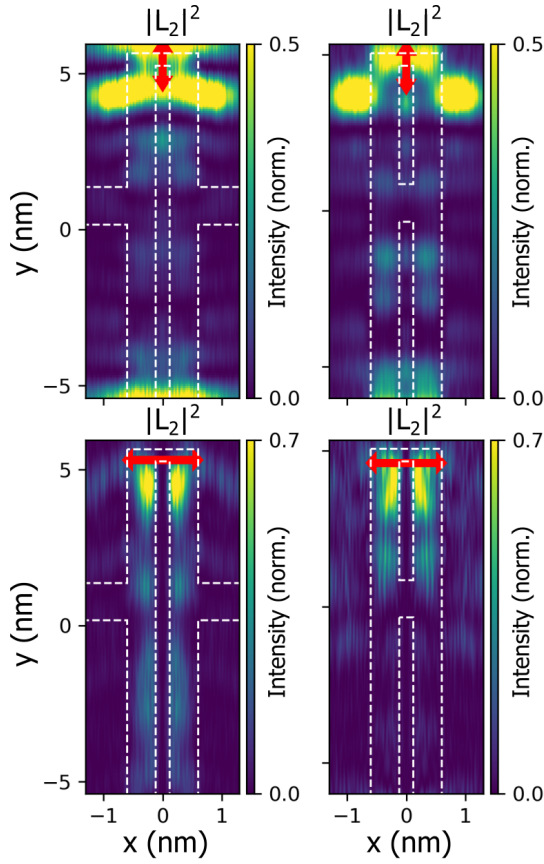Figure 6.4: False-color plot mode intensities measured by L_2 in a TWTL filter structure. Light is coupled at the top of the structure to the symmetric (top) and anti-symmetric (bottom) modes. The even and odd signals are digitally selected for the symmetric and anti-symmetric modes, respectively. The outlines of the outside (left) and inside (right) TWTL filter structures are indicated with a white dashed line.

the same method as we analyzed the odd and even modes in fig. 6.3. Selecting only the even or odd modes allows us to make clearer plots to investigate the function of the filter elements, the unfiltered plots can be found in the supplementary information (fig. 6.8a). Please note that the false-color scale of fig. 6.4 has been saturated on purpose to help visualize the plasmonic modes more clearly.

We calculate the efficiencies of the filter by dividing the average mode intensity 2 μm after the filter element by the average mode intensity 2 μm before the filter element. The intensity of the symmetric mode is at 52% after the exterior filter (top left image), indicating that the exterior filter only filters part of the symmetric mode. However, the symmetric mode, surprisingly, increases in intensity after the interior filter element (top right) (222%). For the anti-symmetric mode, a more clear filtering behavior can be observed. 86% of the anti-symmetric mode is transmitted through the exterior filter element (bottom left) but the anti-symmetric mode is depleted to 15% by the interior filter element (bottom right). Interestingly, from the backward propagating signal obtained by Fourier filtering, we observe mode intensity for the anti-symmetric mode, see supplementary information (fig. 6.8b). This observation indicates that some of the anti-symmetric mode is back reflected into a plasmonic mode with the opposite direction by the inside filter element or at the antenna at the end of the TWTL. The ratio between forward and backward propagating modes is determined at .3. To sum up, we observe quantitative filtering of the anti-symmetric mode by the interior filter design, where the mode is partially back-reflected. For the exterior filter design, we observe less effective filtering of the symmetric mode.

Finally, we investigate a plasmonic Mach-Zehnder interferometer design. In this TWTL system, after exiting the symmetric or anti-symmetric mode using an antenna, the two wires separate spatially. After a detour of one wire, the wires are approached again to form a TWTL, see the white dashed line in fig. 6.5.

To observe plasmonic mode shifting in this TWTL interferometer design, in fig. 6.5(a) the real part of L_1 is plotted from a near-field measurement around the TWTL interferometer. In the measurement plotted in 6.5(a) we excite the symmetric mode. Before the splitting of the two wires, an anti-symmetric pattern of the $Re(L_1)$ signal can be observed on the outside of the TWTL, corresponding to the x-component of the field of the symmetric mode. In the section where the two nanowires are separated, a single nanowire mode signal is measured, where the field pattern is anti-symmetric around the center of the right wire. When the two wires are recombined, a symmetric signal around the TWTL center can be observed, corresponding to the x-component of the anti-symmetric mode. Accordingly, fig. 6.5(a) presents a direct observation of how the symmetric mode of the two-wire system transitions into the eigenmode of the single-wire system and back. Such transitions allow for the design of a plasmonic Mach-Zehnder interferometer that can be used as a passive mode switching element in a TWTL system.

Now we have shown the mode conversion from the symmetric mode to the anti-symmetric mode, we look at the mode intensity transmissions through the interferometer TWTL system for the symmetric and anti-symmetric modes. In fig. 6.5(b) the absolute squares of L_1 (left) and L_2 (right) are plotted for symmetric (top) and anti-symmetric (bottom) mode excitation. From the top images of fig. 6.5(b) we see that the symmetric mode is transmitted through the interferometer system. However, for the anti-
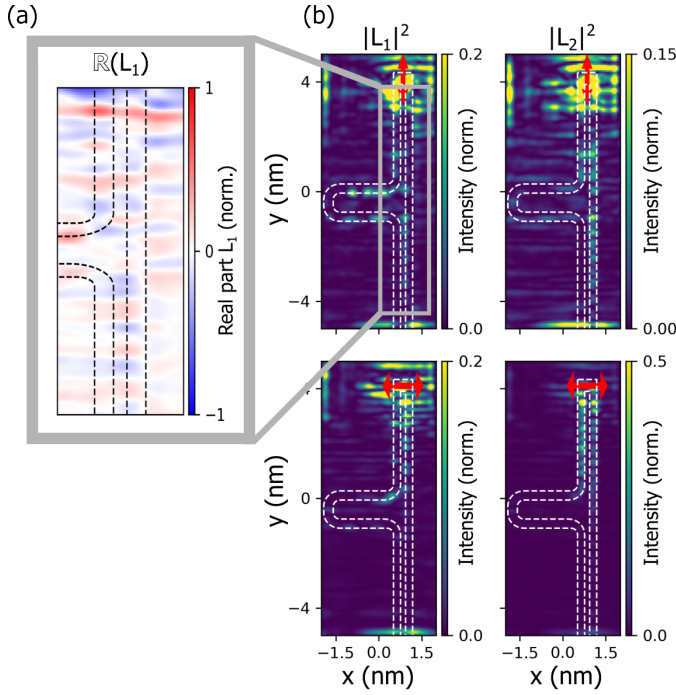
Figure 6.5: (a) False-color plot of the real part of the measured signal L_1 in a plasmonic mode shifter system. (b) Plasmonic field intensities of L_1 (left) and L_2 (right) in the same mode shifter system are indicated by the white dashed line. Light is coupled at the top of the structure to the symmetric (top) and anti-symmetric (bottom) modes.

symmetric mode shown in the bottom images of fig. 6.5(b), we observe almost no transmission through the interferometer system when the wires of the TWTL are separated. While it is possible to shift between the two TWTL modes using a plasmonic interferometer design our data suggest that the efficiency of switching from the anti-symmetric mode to the symmetric mode is lower than the other way around. This is mainly caused by the different coupling strengths from the two-wire modes to the one-wire mode. Since in the interferometer TWTL system the plasmonic modes also propagate in the x direction we filter the plasmonic mode in Fourier space using: $k_0 < \sqrt{k_y^2 + k_x^2}$ combined with k_y and $k_x < 15.7\mu m^{-1}$

In conclusion, we directly measure the local mode amplitude and phase evolution of the symmetric and anti-symmetric modes in various TWTL systems. The near-field measurements of both modes are used to study three nanocircuitry elements: an antenna, a mode filter, and a mode shifter. We find good control of coupling to the two plasmonic modes by changing the far-field polarization. By changing the polarization angle we identify small effects from the antenna properties involving the coupling efficiency ratio and temporal phase difference. For the plasmonic mode filter, we observe good filtering of the anti-symmetric mode using the interior filter element. While the exterior

mode filter is less successful in filtering the symmetric mode. Using a Mach-Zehnder interferometer design, we observe a mode shift from the symmetric to the anti-symmetric mode. These findings experimentally show the near-field behavior of the symmetric and anti-symmetric modes in TWTL systems.

6

6.4. SUPPLEMANTARY INFORMATION

6.4.1. SIMULATED MAGNETIC FIELDS OF THE SYMMETRIC AND ANTI-SYMMETRIC MODE IN A TWTL SYSTEM

In fig. 6.6 the normalized calculated magnetic fields are displayed around the TWTL system for the anti-symmetric and symmetric modes. Figure 6.6 is plotted from the same simulation that is used in the main text for calculating the electric field of the anti-symmetric and symmetric modes, displayed in fig. 6.2.
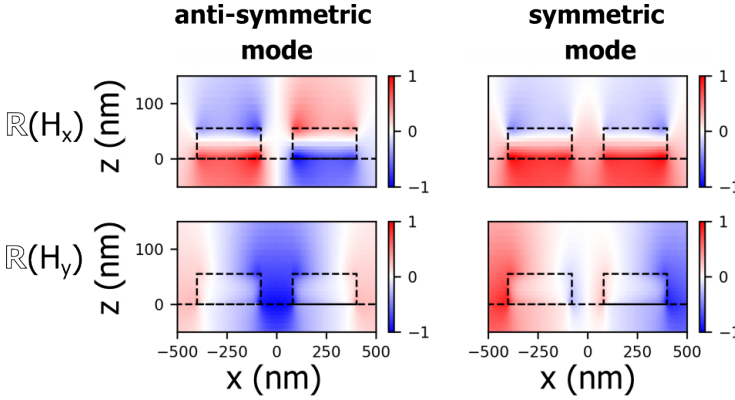

Figure 6.6: The simulated real part of the x- and y-component of the local magnetic field for the symmetric and anti-symmetric mode profiles in a TWTL.

6.4.2. RELATIONSHIP BETWEEN THE NORMALIZED GENERATED INTENSITIES AND THE ANTENNA PARAMETERS

Here, we elaborate on the effect that the antenna properties η and δ have on the generated mode distribution in a TWTL. $|\eta|^2 = \frac{I_{\text{anti}}}{I_{\text{sym}}}$ is the coupling efficiency ratio between the symmetric and anti-symmetric mode and δ is the difference in phase between two modes that they pick up during the coupling from free-space light [115]. Because the symmetric and anti-symmetric modes are the eigenmodes of the TWTL system and they have a slightly different wavevector, a superposition of these two modes will result in an intensity profile that will fluctuate between the left and right wire along the propagation direction.

The intensity of the symmetric and anti-symmetric modes is given by:

$$I_{\text{sym}} = |E_{\text{sym}}|^2 = C_1|cos(\theta)|^2 \quad \text{and} \quad I_{\text{anti}} = |E_{\text{anti}}|^2 = C_1|\eta sin(\theta)e^{i\delta}|^2, \qquad (6.1)$$

where C_1 is a constant equal for both eigenmodes. Here θ is the linear polarization angle as discussed in the main text. Now, by superposition of the symmetric and anti-symmetric mode, the plasmonic mode intensity in the right and left wire can be derived to be:

$$I_{\text{R}} = |\frac{E_{\text{sym}} - E_{\text{anti}}}{\sqrt{2}}|^2 \quad \text{and} \quad I_{\text{L}} = |\frac{E_{\text{sym}} + E_{\text{anti}}}{\sqrt{2}}|^2. \qquad (6.2)$$

From equations 6.1 and 6.2 the mode intensity profiles can be calculated as a function of θ for different values of $|\eta|^2$ and δ. In figure 6.7 we plot the normalized plasmonic intensity in the anti-symmetric mode and in the right wire.
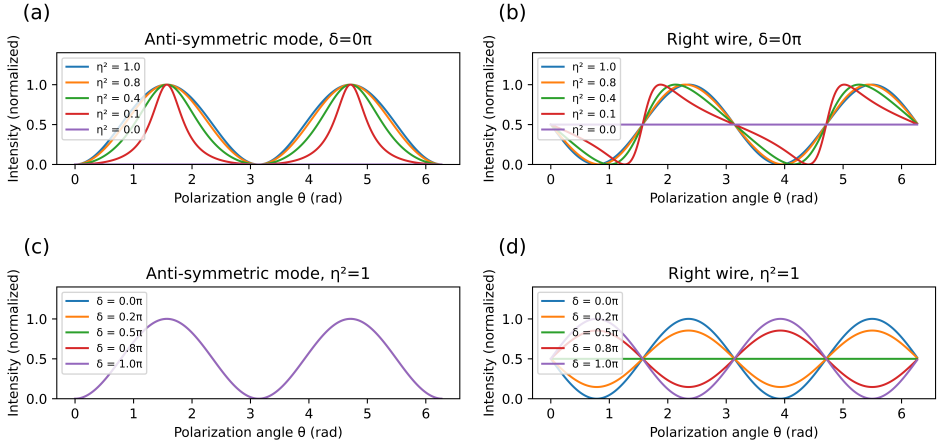
Figure 6.7: Normalized intensities of the anti-symmetric mode and in the right wire, generated by an antenna element in a TWTL system as a function of the polarization angle θ. At (a) and (b) δ is kept constant at 0π and the normalized intensity is plotted for different η^2 between 0 and 1. At (c) and (d) η^2 is kept constant at 1 and the normalized intensity is plotted for different δ between 0π and π.

From fig. 6.7(a) it can be observed that the anti-symmetric normalized mode intensity at $\theta = \frac{\pi}{2}$ and $\theta = \frac{3\pi}{2}$ is 1 for every η^2. However for lower η^2 the shape of the curve

gets narrower around $\theta = \frac{\pi}{2}$ and $\theta = \frac{3\pi}{2}$. From fig. 6.7(b) it follows that the peak positions shifts for the normalized intensity of the right wire to a different θ as function of η^2. Because if η^2 is not 1, an equal superposition between the left and right wire is generated at a different θ. From fig. 6.7(c) it can be observed that the normalized anti-symmetric mode intensity does not depend on δ because for different phases the same excitation of symmetric and anti-symmetric mode occurs. However, for the normalized intensity on the right wire the maximum difference is lowered by adding a phase shift, δ, as seen in fig. 6.7(d). When the symmetric and anti-symmetric modes are generated entirely out of phase the intensity difference between the left and right wire can not be modulated anymore by changing the polarization angle θ, see the green line in fig. 6.7(d).

6

6.4.3. NEAR-FIELD MEASUREMENTS OF FILTER SYSTEMS WITH DIFFERENT MODE FILTERING

Figure 6.8(a) displays the measured near-field intensity around the TWTL filters. Here, the same data is plotted as in fig. 6.4. However, fig. 6.8(a) shows the unfiltered data where the odd and even parts of the fields are not separately selected for the anti-symmetric and symmetric modes. Figure 6.8(b) displays the measured near-field intensity for the back-propagating fields around the TWTL filters. Here the back-propagating fields are selected using the opposite Fourier filtering limits with respect to the forward-propagating fields. In fig. 6.8(b) light intensity can be observed before the interior filter element when the anti-symmetric mode is excited (bottom right image).
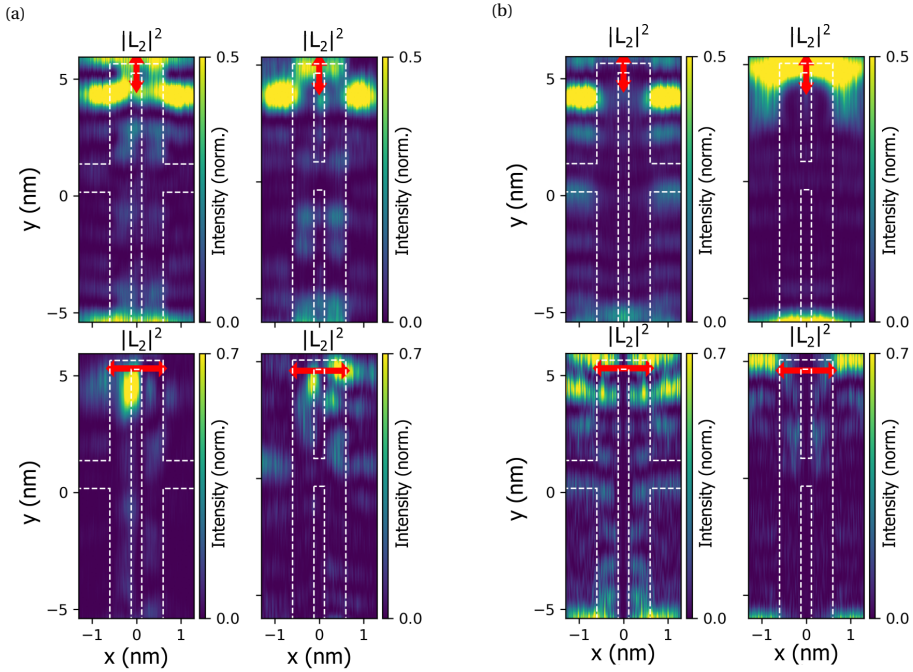
Figure 6.8: (a) Measured near-field intensity around the TWTL filters where the odd and even parts of the fields are not separately selected for the anti-symmetric and symmetric modes. (b) Measured near-field intensity around the TWTL filters where the back-propagating fields are selected using Fourier filtering methods.

IV

CONCLUSIONS AND OUTLOOK

7

CONCLUSION AND OUTLOOK

Here, we reflect on the investigations that are conducted in this thesis. We summarize the obtained results and place them in a broader context within the research field. In addition, we provide suggestions for further research directions toward new discoveries and the implementation of potential applications.

In this thesis, we investigate the interaction between light and either a monolayer of WS$_2$ (chapters 3 and 4) or metallic nanostructures (chapters 5 and 6). In the introduction, we discuss the intriguing behavior of light when it interacts with these structures at the nanoscale. In particular, we elaborate on the optical behaviour of plasmonic nanostructures, nonlinear processes, and transition metal dichalcogenide materials (TMDCs). The interaction of light with a monolayer of WS$_2$ is mainly governed by the presence of the exciton. In our metallic nanostructures, the light interaction is mainly controlled by plasmons. We observe the nonlinear optical interaction of our nanostructures using intense laser pulses in chapters 3,4, and 5. Additionally, we use a near-field optical microscope in chapter 6 to inspect plasmonic modes in a two-wire transmission line (TWTL). In the remainder of this chapter, we place the findings obtained in this thesis in a broader perspective within the research field and discuss ideas for future investigation.

The experiments performed in this thesis demonstrate direct applications of nonlinear optical processes. We especially explore nondegenerate nonlinear processes, generated by two different frequencies. For example, in chapter 5 we use a double resonant plasmonic grating for the frequency conversion of multiple near-infrared laser pulses. Using this double resonant grating we show that we can not only enhance degenerate nonlinear optical processes but also nondegenerate nonlinear processes. We demonstrate that TMDCs such as monolayer WS$_2$ are also especially useful for nondegenerate frequency conversion applications due to their high nonlinear response over a large bandwidth. The nonlinear emission of TMDCs can even be further enhanced in certain geometries [54, 55, 85]. It would be interesting to further investigate the origin of the enhancements of nonlinear (non)degenerate signals at different types of TMDC nanostructures. Finally, the simultaneous characterization of two ultra-short pulses using multiple nonlinear nondegenerate frequency-resolved optical gating (FROG) traces described in chapter 4 is another direct application example of nondegenerate nonlinear optics. In conclusion, frequency conversion and ultra-short pulse characterization are promising applications of the high nonlinear nondegenerate optical response in two-dimensional TMDCs and plasmonic nanostructures.

In addition to direct applications, we also use nonlinear optics as a tool to probe nano-optical phenomena. In the experiments with monolayer WS$_2$ we probe photoluminescence signals generated by nonlinear processes in chapters 3 and 4. We find that nondegenerate nonlinear processes also induce photoluminescence and characterize the power laws of this nondegenerate nonlinear pumping in chapter 3. We note that the nonlinear generated photoluminescence signal is surprisingly large and of the same order of magnitude as the nonlinear parametric signals. During normal photoluminescence measurements, an exciton is excited using a frequency slightly higher than its own frequency and to separate the photoluminescence signal from the residual excitation light, a narrow bandpass filter is used exploiting the stokes shift. However, with nonlinear excitation, there is a large frequency separation between the exciting light and the photoluminescence signal. This allows for the measurement of the full photoluminescence spectrum, even when the exciton is excited with exactly its own frequency through a nonlinear process. Nonlinear excited photoluminescence experiments could be further exploited in for example resonantly pumped nondegenerate nonlinear valley polarization measurements similar to the work of Cheng et al. [35]. Another interesting appli-

cation of nonlinear excited photoluminescence could be an all-optical injection of spin and valley currents [133]. To probe the underlying optical behavior at the nanoscale in plasmonic systems and devices we use nonlinear optical processes as well as near-field measurements. The enormous nonlinear enhancements generated by the double resonant grating in chapter 5 show that nonlinear optics can act as a sensitive probe for the generation of plasmons.

In chapter 6 we use near-field measurements to probe the symmetric and anti-symmetric mode in a two-wire transition line plasmonic system. Furthermore, we explore the plasmonic behavior in two-wire system elements, such as an antenna, filter, and mode converter. Direct investigation of confined plasmonic modes can also help to design novel nanophotonic devices. Recent advances in nanofabrication techniques in combination with the development of robust and versatile commercial finite-difference time-domain (FDTD) simulation software make it possible to develop novel nanostructure devices. But despite the abundance of promising suggestions to implement plasmonics in real-world applications, many plasmonic-based devices have yet to be realized. The confined nature of plasmons makes it particularly hard to design and characterize plasmonic devices. Although plasmonic devices can be used with linear optical measurements using nanophotonic elements that couples free-space light to plasmons and vice versa, it is hard to directly probe the plasmonic behavior. Therefore, other optical techniques can be useful to probe the plasmonic modes. In this thesis, we show examples of how nonlinear and near-field microscopes can characterize plasmonic mode behavior. We observe amplified nonlinear signals that indicate plasmon generation and study plasmonic mode propagation of the symmetric and anti-symmetric modes through multiple TWTL system elements. Further research direction can be focussed on exciting a TWTL system at the antenna with an ultrashort pump beam. An additional probe beam softly focused at the TWTL together with the plasmonic modes can be used to generate nondegenerate nonlinear processes. The plasmonic modes characteristic can be probed from inspection of the nondegenerate signals in real and Fourier space in a similar method as demonstrated by Freschwasser et al. for surface plasmons [134].

Nonlinear and near-field microscopy techniques can also be used to complement theory and FDTD simulations. For example, most simulations take into account a perfectly flat metal/dielectric interface. However, nanofabrication techniques inevitably produce a certain amount of surface roughness. Recent experimental studies show improved performance in plasmonic nanowire structures created from single crystalline gold flakes [13]. Nonlinear studies and near-field microscopic studies can offer an excellent opportunity to study the effect of this surface roughness on plasmonic propagation. A better understanding of the effect of surface roughness on plasmonic propagation can lead to the realization of nanowire systems devices with the performance of single crystalline fabrication but with the scalability of the e-beam and lift-off fabrication.

Two frequency ranges that are particularly promising for further investigation into propagating plasmonic devices are the telecom frequency range, around a free-space wavelength of 1550 nm, and the visible frequency range around a free-space wavelength of 600 nm. In the telecom frequency, range plasmons experience relatively long propagation lengths and can be used for high bandwidth electrical and optical modulation. In the visible frequency range, it is more difficult to design deterministic plasmonic devices

due to the high absorption losses and large k-vector mismatch. Propagating plasmonic systems that are carefully designed to operate at the visible spectrum are suitable for combining with other materials. For example, plasmonic systems can be coupled with TMDC flakes for electro-optical modulation purposes [135] or coupling circular polarized light to specific plasmonic modes [42].

We demonstrated in this thesis a high nonlinear surface response from a plasmonic grating structure as well as from a monolayer of WS_2. An interesting next step would be to integrate a monolayer WS_2 with plasmonic structures to enhance nonlinear optical signals for example for frequency conversion applications. In this way, the high, local electric field amplification originating from the plasmons can be combined with the high nonlinear susceptibilities of the monolayer WS_2. However, an increase in the local electric field also causes more absorption in the WS_2 lowering the effective damage threshold. We found that laser ablation of WS_2 flakes plays an important role in nonlinear experiments. Here, the damage threshold is not only dependent on the average power of the laser beams but also on the peak power of the laser pulses. In our opinion, a more fruitful approach is to investigate the light-matter interaction between propagating plasmonic modes and TMDC material such as WS_2. Properly designed plasmonic devices for the visible range can then be combined with monolayer flakes to improve nonlinear effects generated by propagating plasmons or electrical optical modulation induced by the TMDC sheet.

Throughout this thesis we demonstrated the fascinating behavior of interacting light fields in nanoscale systems such as a monolayer WS_2 and plasmonic structures. Exploring these interacting light fields using nonlinear and near-field microscopy techniques has been shown to help unravel the dynamics of light at the nanoscale. Further investigations in monolayer WS_2, plasmonic structures, and especially a combination of the two is expected to open up many exciting opportunities for fundamental scientific understanding as well as real-world applications.

7

BIBLIOGRAPHY

[1] A. M. Shrivastav, U. Cvelbar, and I. Abdulhalim, "A comprehensive review on plasmonic-based biosensors used in viral diagnostics", Communications biology **4**, 1–12 (2021).

[2] M. Kauranen and A. V. Zayats, "Nonlinear plasmonics", Nature photonics **6**, 737–748 (2012).

[3] T. J. Davis, D. E. Gómez, and A. Roberts, "Plasmonic circuits for manipulating optical information", Nanophotonics **6**, 543–559 (2017).

[4] L. Novotny and B. Hecht, *Principles of nano-optics* (Cambridge university press, 2012).

[5] P. B. Johnson and R. W. Christy, "Optical constants of the noble metals", Physical review B **6**, 4370 (1972).

[6] A. Otto, "Excitation of nonradiative surface plasma waves in silver by the method of frustrated total reflection", Zeitschrift für Physik A Hadrons and nuclei **216**, 398–410 (1968).

[7] E. Kretschmann, "Die bestimmung optischer konstanten von metallen durch anregung von oberflächenplasmaschwingungen", Zeitschrift für Physik A Hadrons and nuclei **241**, 313–324 (1971).

[8] P. Bharadwaj, B. Deutsch, and L. Novotny, "Optical antennas", Advances in Optics and Photonics **1**, 438–483 (2009).

[9] E. D. Palik, *Handbook of optical constants of solids*, Vol. 3 (Academic press, 1998).

[10] A. Sommerfeld, "Ueber die fortpflanzung elektrodynamischer wellen längs eines drahtes", Annalen der Physik **303**, 233–290 (1899).

[11] M. Schnell, P. Alonso-Gonzalez, L. Arzubiaga, F. Casanova, L. E. Hueso, A. Chuvilin, and R. Hillenbrand, "Nanofocusing of mid-infrared energy with tapered transmission lines", Nature photonics **5**, 283–287 (2011).

[12] S. Sun, H.-T. Chen, W.-J. Zheng, and G.-Y. Guo, "Dispersion relation, propagation length and mode conversion of surface plasmon polaritons in silver double-nanowire systems", Optics express **21**, 14591–14605 (2013).

[13] P. Geisler, G. Razinskas, E. Krauss, X.-F. Wu, C. Rewitz, P. Tuchscherer, S. Goetz, C.-B. Huang, T. Brixner, and B. Hecht, "Multimode plasmon excitation and in situ analysis in top-down fabricated nanocircuits", Physical Review Letters **111**, 183901 (2013).

[14] C. Schörner, S. Adhikari, and M. Lippitz, "A single-crystalline silver plasmonic circuit for visible quantum emitters", Nano Letters **19**, 3238–3243 (2019).

[15] M. Prämassing, M. Liebtrau, H. Schill, S. Irsen, and S. Linden, "Interferometric near-field characterization of plasmonic slot waveguides in single-and poly-crystalline gold films", Optics Express **28**, 12998–13007 (2020).

[16]G. Veronis and S. Fan, "Modes of subwavelength plasmonic slot waveguides", Journal of Lightwave Technology **25**, 2511–2521 (2007).

[17]P. A. Franken, A. E. Hill, C. Peters, and G. Weinreich, "Generation of Optical Harmonics", Phys. Rev. Lett. **7**, 118–120 (1961).

[18]T. H. Maiman, "Stimulated optical radiation in ruby", Nature **187**, 493–494 (1960).

[19]R. W. Boyd, *Nonlinear optics* (Academic press, 2008).

[20]Y. R. Shen, *The principles of nonlinear optics* (Wiley-Interscience, 1984).

[21]Y. Li, Y. Rao, K. F. Mak, Y. You, S. Wang, C. R. Dean, and T. F. Heinz, "Probing symmetry properties of few-layer mos2 and h-bn by optical second-harmonic generation", Nano letters **13**, 3329–3333 (2013).

[22]M. Zhao, Z. Ye, R. Suzuki, Y. Ye, H. Zhu, J. Xiao, Y. Wang, Y. Iwasa, and X. Zhang, "Atomically phase-matched second-harmonic generation in a 2D crystal", Light: Science & Applications **5**, e16131 (2016).

[23]I. Komen, "The interaction of light with ws_2 nanostructures", PhD thesis (Delft University of Technology, Delft, Dec. 2021).

[24]N. Papadopoulos, "Mesoscopic transport in 2d materials and heterostructures", PhD thesis (Delft University of Technology, Delft, July 2019).

[25]J. Zeng, M. Yuan, W. Yuan, Q. Dai, H. Fan, S. Lan, and S. Tie, "Enhanced second harmonic generation of mos 2 layers on a thin gold film", Nanoscale **7**, 13547–13553 (2015).

[26]B. Zhu, X. Chen, and X. Cui, "Exciton binding energy of monolayer ws2", Scientific reports **5**, 1–5 (2015).

[27]A. Autere, H. Jussila, Y. Dai, Y. Wang, H. Lipsanen, and Z. Sun, "Nonlinear optics with 2d layered materials", Advanced Materials **30**, 1705963 (2018).

[28]G. Wang, X. Marie, I. Gerber, T. Amand, D. Lagarde, L. Bouet, M. Vidal, A. Balocchi, and B. Urbaszek, "Giant enhancement of the optical second-harmonic emission of wse 2 monolayers by laser excitation at exciton resonances", Physical review letters **114**, 097403 (2015).

[29]A. Autere, H. Jussila, A. Marini, J. Saavedra, Y. Dai, A. Säynätjoki, L. Karvonen, H. Yang, B. Amirsolaimani, R. A. Norwood, et al., "Optical harmonic generation in monolayer group-vi transition metal dichalcogenides", Physical Review B **98**, 115426 (2018).

[30]C. Janisch, Y. Wang, D. Ma, N. Mehta, A. L. Elias, N. Perea-López, M. Terrones, V. Crespi, and Z. Liu, "Extraordinary second harmonic generation in tungsten disulfide monolayers", Scientific reports **4**, 1–5 (2014).

[31]K. Hao, G. Moody, F. Wu, C. K. Dass, L. Xu, C.-H. Chen, L. Sun, M.-Y. Li, L.-J. Li, A. H. MacDonald, et al., "Direct measurement of exciton valley coherence in monolayer wse2", Nature Physics **12**, 677–682 (2016).

[32]T. Jakubczyk, K. Nogajewski, M. R. Molas, M. Bartos, W. Langbein, M. Potemski, and J. Kasprzak, "Impact of environment on dynamics of exciton complexes in a ws2 monolayer", 2D Materials **5**, 031007 (2018).

7

[33] H. Ma, J. Liang, H. Hong, K. Liu, D. Zou, M. Wu, and K. Liu, "Rich information on 2d materials revealed by optical second harmonic generation", Nanoscale **12**, 22891–22903 (2020).

[34] D. Li, W. Xiong, L. Jiang, Z. Xiao, H. Rabiee Golgir, M. Wang, X. Huang, Y. Zhou, Z. Lin, J. Song, et al., "Multimodal nonlinear optical imaging of mos2 and mos2-based van der waals heterostructures", ACS nano **10**, 3766–3775 (2016).

[35] J. Cheng, D. Huang, T. Jiang, Y. Shan, Y. Li, S. Wu, and W.-T. Liu, "Chiral selection rules for multi-photon processes in two-dimensional honeycomb materials", Optics letters **44**, 2141–2144 (2019).

[36] Y. W. Ho, H. G. Rosa, I. Verzhbitskiy, M. J. Rodrigues, T. Taniguchi, K. Watanabe, G. Eda, V. M. Pereira, and J. C. Viana-Gomes, "Measuring valley polarization in two-dimensional materials with second-harmonic spectroscopy", ACS Photonics **7**, 925–931 (2020).

[37] K. L. Seyler, J. R. Schaibley, P. Gong, P. Rivera, A. M. Jones, S. Wu, J. Yan, D. G. Mandrus, W. Yao, and X. Xu, "Electrical control of second-harmonic generation in a wse 2 monolayer transistor", Nature nanotechnology **10**, 407–411 (2015).

[38] A. Castellanos-Gomez, M. Buscema, R. Molenaar, V. Singh, L. Janssen, H. S. Van Der Zant, and G. A. Steele, "Deterministic transfer of two-dimensional materials by all-dry viscoelastic stamping", 2D Materials **1**, 011002 (2014).

[39] Y. Bai, L. Zhou, J. Wang, W. Wu, L. J. McGilly, D. Halbertal, C. F. B. Lo, F. Liu, J. Ardelean, P. Rivera, et al., "Excitons in strain-induced one-dimensional moiré potentials at transition metal dichalcogenide heterojunctions", Nature Materials **19**, 1068–1073 (2020).

[40] Y. Li, M. Kang, J. Shi, K. Wu, S. Zhang, and H. Xu, "Transversely divergent second harmonic generation by surface plasmon polaritons on single metallic nanowires", Nano letters **17**, 7803–7808 (2017).

[41] C. Errando-Herranz, E. Scholl, R. Picard, M. Laini, S. Gyger, A. W. Elshaari, A. Branny, U. Wennberg, S. Barbat, T. Renaud, et al., "Resonance fluorescence from waveguide-coupled, strain-localized, two-dimensional quantum emitters", ACS photonics **8**, 1069–1076 (2021).

[42] S.-H. Gong, F. Alpeggiani, B. Sciacca, E. C. Garnett, and L. Kuipers, "Nanoscale chiral valley-photon interface through optical spin-orbit coupling", Science **359**, 443–447 (2018).

[43] B. L. Feber, "Nanoscale electric and magnetic optical vector fields: mapping & injection", PhD thesis (University of Twente, Enschede, Jan. 2015).

[44] A. de Hoogh, "Optical singularities and nonlinear effects near plasmonic nanostructures", PhD thesis (Delft University of Technology, Delft, Dec. 2016).

[45] L. D. Angelis, "The singular optics of random light", PhD thesis (Delft University of Technology, Mekelweg 5, 2628 CD Delft, Dec. 2018).

[46] N. Rotenberg and L. Kuipers, "Mapping nanoscale light fields", Nature Photonics **8**, 919–926 (2014).

7

[47] J. Veerman, A. Otter, L. Kuipers, and N. Van Hulst, "High definition aperture probes for near-field optical microscopy fabricated by focused ion beam milling", Applied Physics Letters **72**, 3115–3117 (1998).

[48] M. Burresi, R. Engelen, A. Opheij, D. van Oosten, D. Mori, T. Baba, and L. Kuipers, "Observation of polarization singularities at the nanoscale", Physical review letters **102**, 033902 (2009).

[49] M. Balistreri, J. P. Korterik, L. Kuipers, and N. Van Hulst, "Local observations of phase singularities in optical fields in waveguide structures", Physical review letters **85**, 294 (2000).

[50] Y. Huang, E. Sutter, N. N. Shi, J. Zheng, T. Yang, D. Englund, H.-J. Gao, and P. Sutter, "Reliable exfoliation of large-area high-quality flakes of graphene and other two-dimensional materials", ACS nano **9**, 10612–10620 (2015).

[51] S.-H. Gong, I. Komen, F. Alpeggiani, and L. Kuipers, "Nanoscale optical addressing of valley pseudospins through transverse optical spin", Nano letters **20**, 4410–4415 (2020).

[52] P. Liu, T. Luo, J. Xing, H. Xu, H. Hao, H. Liu, and J. Dong, "Large-area ws2 film with big single domains grown by chemical vapor deposition", Nanoscale research letters **12**, 1–10 (2017).

[53] C. Cong, J. Shang, X. Wu, B. Cao, N. Peimyoo, C. Qiu, L. Sun, and T. Yu, "Synthesis and optical properties of large-area single-crystalline 2d semiconductor ws2 monolayer from chemical vapor deposition", Advanced Optical Materials **2**, 131–136 (2014).

[54] M. Bolhuis, J. Hernandez-Rueda, S. van Heijst, M. T. Rivas, L. Kuipers, and S. Conesa-Boj, "Vertically-oriented mos 2 nanosheets for nonlinear optical devices", Nanoscale **12**, 10491–10497 (2020).

[55] L. Maduro, M. Noordam, M. Bolhuis, L. Kuipers, and S. Conesa-Boj, "Position-controlled fabrication of vertically aligned mo/mos2 core–shell nanopillar arrays", Advanced Functional Materials **32**, 2107880 (2022).

[56] I. Komen, S. E. van Heijst, S. Conesa-Boj, and L. Kuipers, "Morphology-induced spectral modification of self-assembled ws 2 pyramids", Nanoscale advances **3**, 6427–6437 (2021).

[57] I. Komen, S. E. van Heijst, M. Caldarola, S. Conesa-Boj, and L. Kuipers, "Revealing the nanogeometry of ws2 nanoflowers by polarization-resolved raman spectroscopy", Journal of Applied Physics **132**, 173103 (2022).

[58] W. Zhao, Z. Ghorannevis, L. Chu, M. Toh, C. Kloc, P.-H. Tan, and G. Eda, "Evolution of electronic structure in atomically thin sheets of ws2 and wse2", ACS nano **7**, 791–797 (2013).

[59] J.-S. Huang, V. Callegari, P. Geisler, C. Brüning, J. Kern, J. C. Prangsma, X. Wu, T. Feichtner, J. Ziegler, P. Weinmann, et al., "Atomically flat single-crystalline gold nanostructures for plasmonic nanocircuitry", Nature communications **1**, 1–8 (2010).

[60] J. Hernandez-Rueda, M. L. Noordam, I. Komen, and L. Kuipers, "Nonlinear optical response of a ws2 monolayer at room temperature upon multicolor laser excitation", ACS photonics **8**, 550–556 (2021).

[61] A. Säynätjoki, L. Karvonen, H. Rostami, A. Autere, S. Mehravar, A. Lombardo, R. A. Norwood, T. Hasan, N. Peyghambarian, H. Lipsanen, et al., "Ultra-strong nonlinear optical processes and trigonal warping in mos 2 layers", Nature communications **8**, 1–8 (2017).

[62] K. F. Lee, Y. Tian, H. Yang, K. Mustonen, A. Martinez, Q. Dai, E. I. Kauppinen, J. Malowicki, P. Kumar, and Z. Sun, "Photon-pair generation with a 100 nm thick carbon nanotube film", Advanced Materials **29**, 1605978 (2017).

[63] F. Wang, G. Dukovic, L. E. Brus, and T. F. Heinz, "The optical resonances in carbon nanotubes arise from excitons", Science **308**, 838–841 (2005).

[64] M. Lafrentz, D. Brunne, A. Rodina, V. Pavlov, R. Pisarev, D. Yakovlev, A. Bakin, and M. Bayer, "Second-harmonic generation spectroscopy of excitons in zno", Physical Review B **88**, 235207 (2013).

[65] M. Noordam, J. Hernandez-Rueda, L. Talsma, and L. Kuipers, "Plasmon-induced enhancement of nonlinear optical processes in a double-resonant metallic nanostructure grating", Applied Physics Letters **116**, 101101 (2020).

[66] E. Hendry, P. J. Hale, J. Moger, A. Savchenko, and S. A. Mikhailov, "Coherent nonlinear optical response of graphene", Physical review letters **105**, 097401 (2010).

[67] H. Zeng, G.-B. Liu, J. Dai, Y. Yan, B. Zhu, R. He, L. Xie, S. Xu, X. Chen, W. Yao, et al., "Optical signature of symmetry variations and spin-valley coupling in atomically thin tungsten dichalcogenides", Scientific reports **3**, 1–5 (2013).

[68] A. Berkdemir, H. R. Gutiérrez, A. R. Botello-Méndez, N. Perea-López, A. L. Elias, C.-I. Chia, B. Wang, V. H. Crespi, F. López-Urı́eas, J.-C. Charlier, et al., "Identification of individual and few layers of ws2 using raman spectroscopy", Scientific reports **3**, 1–8 (2013).

[69] Z. Ye, T. Cao, K. O'brien, H. Zhu, X. Yin, Y. Wang, S. G. Louie, and X. Zhang, "Probing excitonic dark states in single-layer tungsten disulphide", Nature **513**, 214–218 (2014).

[70] L. Mennel, M. M. Furchi, S. Wachter, M. Paur, D. K. Polyushkin, and T. Mueller, "Optical imaging of strain in two-dimensional crystals", Nature communications **9**, 516 (2018).

[71] M. L. Noordam, J. Hernandez-Rueda, and L. Kuipers, "Simultaneous characterization of two ultrashort optical pulses at different frequencies using a ws2 monolayer", ACS photonics **9**, 1902–1907 (2022).

[72] R. Trebino, K. W. DeLong, D. N. Fittinghoff, J. N. Sweetser, M. A. Krumbügel, B. A. Richman, and D. J. Kane, "Measuring ultrashort laser pulses in the time-frequency domain using frequency-resolved optical gating", Review of Scientific Instruments **68**, 3277–3295 (1997).

[73] D. J. Kane and R. Trebino, "Characterization of arbitrary femtosecond pulses using frequency-resolved optical gating", IEEE Journal of Quantum Electronics **29**, 571–579 (1993).

[74] I. Amat-Roldán, I. G. Cormack, P. Loza-Alvarez, E. J. Gualda, and D. Artigas, "Ultrashort pulse characterisation with shg collinear-frog", Optics express **12**, 1169–1178 (2004).

7

[75] J. Hyyti, E. Escoto, and G. Steinmeyer, "Third-harmonic interferometric frequency-resolved optical gating", JOSA B **34**, 2367–2375 (2017).

[76] A. S. Johnson, E. B. Amuah, C. Brahms, and S. Wall, "Measurement of 10 fs pulses across the entire visible to near-infrared spectral range", Scientific Reports **10**, 1–7 (2020).

[77] A. Lanin, A. Fedotov, and A. Zheltikov, "Ultrabroadband xfrog of few-cycle mid-infrared pulses by four-wave mixing in a gas", JOSA B **31**, 1901–1905 (2014).

[78] Y. Nakano and T. Imasaka, "Cross-correlation frequency-resolved optical gating for characterization of an ultrashort optical pulse train", Applied Physics B **123**, 1–7 (2017).

[79] B. Tsermaa, B.-K. Yang, M.-W. Kim, and J.-S. Kim, "Characterization of supercontinuum and ultraviolet pulses by using xfrog", Journal of the Optical Society of Korea **13**, 158–165 (2009).

[80] R. Weigand, J. Mendonca, and H. M. Crespo, "Cascaded nondegenerate four-wave-mixing technique for high-power single-cycle pulse synthesis in the visible and ultraviolet ranges", Physical Review A **79**, 063838 (2009).

[81] T. C. Wong, J. Ratner, V. Chauhan, J. Cohen, P. M. Vaughan, L. Xu, A. Consoli, and R. Trebino, "Simultaneously measuring two ultrashort laser pulses on a single-shot using double-blind frequency-resolved optical gating", JOSA B **29**, 1237–1244 (2012).

[82] T. C. Wong, J. Ratner, and R. Trebino, "Simultaneous measurement of two different-color ultrashort pulses on a single shot", JOSA B **29**, 1889–1893 (2012).

[83] S. D. Gennaro, Y. Li, S. A. Maier, and R. F. Oulton, "Double blind ultrafast pulse characterization by mixed frequency generation in a gold antenna", ACS Photonics **5**, 3166–3171 (2018).

[84] J. Khurgin, "Graphene—a rather ordinary nonlinear optical material", Applied Physics Letters **104**, 161116 (2014).

[85] X. Lin, Y. Liu, K. Wang, C. Wei, W. Zhang, Y. Yan, Y. J. Li, J. Yao, and Y. S. Zhao, "Two-dimensional pyramid-like ws2 layered structures for highly efficient edge second-harmonic generation", ACS nano **12**, 689–696 (2018).

[86] X. Fan, Y. Jiang, X. Zhuang, H. Liu, T. Xu, W. Zheng, P. Fan, H. Li, X. Wu, X. Zhu, et al., "Broken symmetry induced strong nonlinear optical effects in spiral ws2 nanosheets", ACS nano **11**, 4892–4898 (2017).

[87] J. Shi, W.-Y. Liang, S. S. Raja, Y. Sang, X.-Q. Zhang, C.-A. Chen, Y. Wang, X. Yang, Y.-H. Lee, H. Ahn, et al., "Plasmonic enhancement and manipulation of optical nonlinearity in monolayer tungsten disulfide", Laser & Photonics Reviews **12**, 1800188 (2018).

[88] C. Janisch, N. Mehta, D. Ma, A. L. Elias, N. Perea-López, M. Terrones, and Z. Liu, "Ultrashort optical pulse characterization using ws 2 monolayers", Optics letters **39**, 383–385 (2014).

[89] N. C. Geib, M. Zilk, T. Pertsch, and F. Eilenberger, "Common pulse retrieval algorithm: a fast and universal method to retrieve ultrashort pulses", Optica **6**, 495–505 (2019).

[90] R. Trebino, *Frequency-resolved optical gating: the measurement of ultrashort laser pulses: the measurement of ultrashort laser pulses* (Springer Science & Business Media, 2000).

7

[91] J. Hyyti, M. Perestjuk, F. Mahler, R. Grunwald, F. Güell, C. Gray, E. McGlynn, and G. Steinmeyer, "Field enhancement of multiphoton induced luminescence processes in zno nanorods", Journal of Physics D: Applied Physics **51**, 105306 (2018).

[92] S. Akturk, M. Kimmel, P. O'Shea, and R. Trebino, "Measuring pulse-front tilt in ultrashort pulses using grenouille", Optics Express **11**, 491–501 (2003).

[93] Y. Shen, "Surface properties probed by second-harmonic and sum-frequency generation", Nature **337**, 519–525 (1989).

[94] J. Van Nieuwstadt, M. Sandtke, R. Harmsen, F. B. Segerink, J. Prangsma, S. Enoch, and L. Kuipers, "Strong modification of the nonlinear optical response of metallic subwavelength hole arrays", Physical review letters **97**, 146102 (2006).

[95] E. Almeida and Y. Prior, "Rational design of metallic nanocavities for resonantly enhanced four-wave mixing", Scientific reports **5**, 1–10 (2015).

[96] R. Kolkowski, J. Szeszko, B. Dwir, E. Kapon, and J. Zyss, "Non-centrosymmetric plasmonic crystals for second-harmonic generation with controlled anisotropy and enhancement", Laser & Photonics Reviews **10**, 287–298 (2016).

[97] J. Renger, R. Quidant, N. Van Hulst, and L. Novotny, "Surface-enhanced nonlinear four-wave mixing", Physical review letters **104**, 046803 (2010).

[98] P. Genevet, J.-P. Tetienne, E. Gatzogiannis, R. Blanchard, M. A. Kats, M. O. Scully, and F. Capasso, "Large enhancement of nonlinear optical phenomena by plasmonic nanocavity gratings", Nano letters **10**, 4880–4883 (2010).

[99] N. C. Panoiu, W. E. Sha, D. Lei, and G. Li, "Nonlinear optics in plasmonic nanostructures", Journal of Optics **20**, 083001 (2018).

[100] Y. Jung, H. Chen, L. Tong, and J.-X. Cheng, "Imaging gold nanorods by plasmon-resonance-enhanced four wave mixing", The Journal of Physical Chemistry C **113**, 2657–2663 (2009).

[101] Y. Zhang, N. K. Grady, C. Ayala-Orozco, and N. J. Halas, "Three-dimensional nanostructures as highly efficient generators of second harmonic light", Nano letters **11**, 5519–5523 (2011).

[102] H. Aouani, O. Mahboub, N. Bonod, E. Devaux, E. Popov, H. Rigneault, T. W. Ebbesen, and J. Wenger, "Bright unidirectional fluorescence emission of molecules in a nanoaperture with plasmonic corrugations", Nano letters **11**, 637–644 (2011).

[103] H. Hagman, O. Bäcke, J. Kiskis, F. Svedberg, M. P. Jonsson, F. Höök, and A. Enejder, "Plasmon-enhanced four-wave mixing by nanoholes in thin gold films", Optics Letters **39**, 1001–1004 (2014).

[104] Y. Blechman, E. Almeida, B. Sain, and Y. Prior, "Optimizing the nonlinear optical response of plasmonic metasurfaces", Nano letters **19**, 261–268 (2018).

[105] C.-Y. Wang, H.-Y. Chen, L. Sun, W.-L. Chen, Y.-M. Chang, H. Ahn, X. Li, and S. Gwo, "Giant colloidal silver crystals for low-loss linear and nonlinear plasmonics", Nature communications **6**, 1–7 (2015).

7

[106] H. Harutyunyan, G. Volpe, R. Quidant, and L. Novotny, "Enhancing the nonlinear optical response using multifrequency gold-nanowire antennas", Physical review letters **108**, 217403 (2012).

[107] Z. Zhu, B. Bai, H. Duan, H. Zhang, M. Zhang, O. You, Q. Li, Q. Tan, J. Wang, S. Fan, et al., "M-shaped grating by nanoimprinting: a replicable, large-area, highly active plasmonic surface-enhanced raman scattering substrate with nanogaps", Small **10**, 1603–1611 (2014).

[108] S. Park, J. W. Hahn, and J. Y. Lee, "Doubly resonant metallic nanostructure for high conversion efficiency of second harmonic generation", Optics express **20**, 4856–4870 (2012).

[109] M. Weismann and N. C. Panoiu, "Theoretical and computational analysis of second- and third-harmonic generation in periodically patterned graphene and transition-metal dichalcogenide monolayers", Physical Review B **94**, 035435 (2016).

[110] H. Wei, D. Pan, S. Zhang, Z. Li, Q. Li, N. Liu, W. Wang, and H. Xu, "Plasmon waveguiding in nanowires", Chemical reviews **118**, 2882–2926 (2018).

[111] M. Thomaschewski and S. Bozhevolnyi, "Pockels modulation in integrated nanophotonics", Applied Physics Reviews **9**, 021311 (2022).

[112] S. I. Bozhevolnyi, "Plasmonic nano-guides and circuits", in Plasmonics and metamaterials (Optica Publishing Group, 2008), MWD3.

[113] A. Tuniz, O. Bickerton, F. J. Diaz, T. Käsebier, E.-B. Kley, S. Kroker, S. Palomba, and C. M. de Sterke, "Modular nonlinear hybrid plasmonic circuit", Nature communications **11**, 1–8 (2020).

[114] E. Verhagen, M. Spasenović, A. Polman, and L. K. Kuipers, "Nanowire plasmon excitation by adiabatic mode transformation", Physical review letters **102**, 203904 (2009).

[115] T.-Y. Chen, D. Tyagi, Y.-C. Chang, and C.-B. Huang, "A polarization-actuated plasmonic circulator", Nano Letters **20**, 7543–7549 (2020).

[116] T. Feichtner, O. Selig, M. Kiunke, and B. Hecht, "Evolutionary optimization of optical antennas", Physical review letters **109**, 127701 (2012).

[117] E. Krauss, G. Razinskas, D. Köck, S. Grossmann, and B. Hecht, "Reversible mapping and sorting the spin of photons on the nanoscale: a spin-optical nanodevice", Nano letters **19**, 3364–3369 (2019).

[118] Y. Kan, S. Kumar, F. Ding, C. Zhao, and S. I. Bozhevolnyi, "Spin–orbit controlled excitation of quantum emitters in hybrid plasmonic nanocircuits", Advanced Optical Materials **8**, 2000854 (2020).

[119] A. Afridi and Ş. E. Kocabaş, "Beam steering and impedance matching of plasmonic horn nanoantennas", Optics express **24**, 25647–25652 (2016).

[120] C. Rewitz, G. Razinskas, P. Geisler, E. Krauss, S. Goetz, M. Pawłowska, B. Hecht, and T. Brixner, "Coherent control of plasmon propagation in a nanocircuit", Physical Review Applied **1**, 014007 (2014).

[121] Y.-T. Hung, C.-B. Huang, and J.-S. Huang, "Plasmonic mode converter for controlling optical impedance and nanoscale light-matter interaction", Optics express **20**, 20342–20355 (2012).

[122] W.-H. Dai, F.-C. Lin, C.-B. Huang, and J.-S. Huang, "Mode conversion in high-definition plasmonic optical nanocircuits", Nano letters **14**, 3881–3886 (2014).

[123] M. Ochs, L. Zurak, E. Krauss, J. Meier, M. Emmerling, R. Kullock, and B. Hecht, "Nanoscale electrical excitation of distinct modes in plasmonic waveguides", Nano Letters **21**, 4225–4230 (2021).

[124] M. Thomaschewski, V. A. Zenin, C. Wolff, and S. I. Bozhevolnyi, "Plasmonic monolithic lithium niobate directional coupler switches", Nature communications **11**, 1–6 (2020).

[125] M. Thomaschewski, C. Wolff, and S. I. Bozhevolnyi, "High-speed plasmonic electro-optic beam deflectors", Nano Letters **21**, 4051–4056 (2021).

[126] M. Thomaschewski, Y. Yang, C. Wolff, A. S. Roberts, and S. I. Bozhevolnyi, "On-chip detection of optical spin–orbit interactions in plasmonic nanocircuits", Nano Letters **19**, 1166–1171 (2019).

[127] P. Sarriugarte, M. Schnell, A. Chuvilin, and R. Hillenbrand, "Polarization-resolved near-field characterization of nanoscale infrared modes in transmission lines fabricated by gallium and helium ion beam milling", Acs Photonics **1**, 604–611 (2014).

[128] P. M. Krenz, R. L. Olmon, B. A. Lail, M. B. Raschke, and G. D. Boreman, "Near-field measurement of infrared coplanar strip transmission line attenuation and propagation constants", Optics express **18**, 21678–21686 (2010).

[129] M. Wulf, A. de Hoogh, N. Rotenberg, and L. Kuipers, "Ultrafast plasmonics on gold nanowires: confinement, dispersion, and pulse propagation", ACS Photonics **1**, 1173–1180 (2014).

[130] I. V. Kabakova, A. De Hoogh, R. E. Van Der Wel, M. Wulf, B. Le Feber, and L. Kuipers, "Imaging of electric and magnetic fields near plasmonic nanowires", Scientific Reports **6**, 1–9 (2016).

[131] S. Arora, T. Bauer, R. Barczyk, E. Verhagen, and L. Kuipers, "Direct quantification of topological protection in symmetry-protected photonic edge states at telecom wavelengths", Light: Science & Applications **10**, 1–7 (2021).

[132] B. le Feber, N. Rotenberg, D. Van Oosten, and L. Kuipers, "Modal symmetries at the nanoscale: a route toward a complete vectorial near-field mapping", Optics Letters **39**, 2802–2805 (2014).

[133] R. A. Muniz and J. Sipe, "All-optical injection of charge, spin, and valley currents in monolayer transition-metal dichalcogenides", Physical Review B **91**, 085404 (2015).

[134] K. Frischwasser, K. Cohen, J. Kher-Alden, S. Dolev, S. Tsesses, and G. Bartal, "Real-time sub-wavelength imaging of surface waves with nonlinear near-field optical microscopy", Nature Photonics **15**, 442–448 (2021).

[135] J. van de Groep, J.-H. Song, U. Celano, Q. Li, P. G. Kik, and M. L. Brongersma, "Exciton resonance tuning of an atomically thin lens", Nature Photonics **14**, 426–430 (2020).

7

ACKNOWLEDGEMENTS

The acknowledgments section is often referred to as the most read section of a thesis, suggesting that a PhD project is about people more than anything else. In this regard, my PhD journey was no exception. The work in this thesis could only be possible due to the intelligent, enthusiastic, and loving people surrounding me during my PhD project. I am deeply grateful for all the interesting people I had the opportunity to meet during my PhD. In the following section, I would like to express my gratitude to some of the individuals that played a large role during my PhD.

First of all, I would like to thank my promoter **Kobus**. From our very first meeting onwards I had the feeling we understand each other well. I appreciate that I could talk openly about all the different kinds of challenges that I encountered during my PhD. And I have fond memories of all the times I walked out of your office still laughing about a stupid joke or a discussion that spiraled out of control at the end of our meetings. I admire your passion (and deep understanding!) for physics and your skill to explain a difficult topic on different levels of knowledge. **Herre**, thank you for being my co-promotor, I appreciated your feedback during the yearly meetings coming from many years of experience in the scientific world. Especially, your suggestion to visit the winter school in Kirchbergen.

During my PhD, the NanoOptics group underwent changes in both size and composition, but I experienced their relentless support throughout the entire time I spend within the group. **Javi**, we joined the group around the same time and started together the nonlinear optics project. Although we have worked together in the lab for only a year it certainly feels much longer. Our joint effort gave my PhD a big kick-start and together we achieved much more than I could ever do on my own. I greatly appreciate your endless enthusiasm while introducing me to the world of lasers, building optical setups, and Spanish swear words. Your approach to teaching was very effective for me and I envy all the future students that will be under your guidance. **Fillipe**, your interesting perspectives during the lunch conversations showed that there is more than one way to approach science, a PhD, and life in general. **Aron**, I admit I had to bluff my way through our first discussions about the technical details of the setup. But due to your practical approach and thorough explanations, we overcame many challenges during my PhD, from writing with "class objects" in python to plumbing the cooling system of the laser. Your curious mindset goes a long way (from fixing ultrashort laser systems to mixing different types of alcohol)! **Martin**, I had a lot of fun being introduced to your setup and working together for a short time. Hidden behind (some) complaining, I observed the great amount of pure dedication and carefulness you put into constructing your setup. **Thomas**, you seem to have found a list of specific topics in life you care deeply about and you also like to share those as much as possible with the people around you. Luckily for me, this list contains chocolate, gin, and also physics. Although we mostly worked on different projects you were always interested in my projects and could help me with

your deep knowledge of nano optics. **Irina**, your straightforward and clear way of communication where often a welcome relief in a group that tends to make matters more complicated than they have to be. I enjoyed our morning coffee discussions and the cryogenic experiments we did together using the other expresso machine. Believe it or not, I even suggested lab cleaning myself when you left the group. **Thijs**, I always enjoyed your company, at the Friday evening borrels and especially at NFO. In Canada, we went from (very rewarding) power hour presentation practice sessions via an interesting conference dinner to relaxing strolls in a botanic garden and along the seashore. **Sonakshi**, together we grew from two ambitious PhD students working on different projects to partners in crime wrapping up their PhDs. During our time together in the lab, you have taught me a lot. Outside of the lab I really appreciate our friendship which has grown over the last four years. Between boarding the early train back from Lunteren (we are not all winners) and taking the Thalys to Paris to present (and applaud) our scientific talks, we had a fun ride. **Daniel**, I found it very enjoyable to show you around the lab during the last months of my PhD. Although I find it quite worrisome that you converted to a Feyenoord supporter only a few months after living in Rotterdam, I believe you will have an amazing time during the remainder of your PhD. **Lars** and **Thomas** you were both very bright students and involved in your projects. Thanks for passing down the student vibes along the way.

I would also like to thank the Quantum Nanoscience department. I look pleasantly back on all the enjoyable lunch conversations that I had with many people from our department. Especially I want to thank the QM3 teaching crew, **Andrea**, **Sander**, **Marios**, **Jorrit**, **Rasa**, and **Patrick**. I learned more during our teaching sessions than I did during my quantum mechanics courses as a student. **Luigi** and **Sonia**, it has been a pleasure to work with you on a research project outside my own group. It is inspiring to see the amount of creativity and dedication with which you fabricate novel TMDC nanostructures. **Kars**, I was thrilled to hear that after doing the Bachelor's together in Amsterdam you would come to Delft to do a PhD in the same department (even though it is a theory project). Playing games together was a perfect stress release, from losing chess to you during a coffee break to late-night sessions of repeatedly crashing cars on a deserted island. **Tino**, thanks for your technical support and advice for anything that had to do with the lab. **Heleen** and **Etty**, I appreciate all the advice and support I got from you from the moment I started my PhD. Including the 12x4 remainder emails, you had to send me about registering my monthly hours. I want to thank everyone from the cleanroom staff for their help in fabricating the samples in the cleanroom. I was blessed that I could benefit from a cleanroom with so much expertise and state-of-the-art equipment.

Finally, I would like to thank my friends and family for their unfailing support. Your intentional, and maybe even more often unintentional, help and encouragement over the past four years made me grow as a person and as a scientist. Without it, I would not have been able to achieve the thesis. **Papa**, I was very fortunate with someone so close to me, that could listen to and understand all my new endeavors in the field of physics and even could inspire me with stories of your own experiments. I cherish the moments we discussed my PhD and I am grateful to make a contribution to your book. **Mama**, thanks for keeping our family gatherings free from work discussions (which can be a hard thing with a father, a husband, and now also a son involved in physics). I always felt

your unconditional support and care, no matter what was going on in my life and PhD. **Fieke**, your practical goal-getter attitude gave me a refreshing and helpful perspective during my PhD. I value the amount of joyful energy you have throughout our countless conversations, from dividing the ice cream cake into fair shares to deciding whether or not to do a PhD. **Jessie**, who would have believed 12 years (3PhDs!) ago you would be still at my side today when I am defending my PhD. You supported me through all the ups and downs of my PhD but more importantly, you showed me all the other experiences life has to offer. I can not wait for the next adventures we will have together.

7

Curriculum Vitæ

Marcus Lambertus Noordam

29-07-1994   Born in Amsterdam, the Netherlands.

Education

2007–2013   Highschool
             Eerste Christelijk Lyceum, Haarlem

2013–2016   Bachelor Bèta-gamma major Physics
             Universiteit van Amsterdam
             Thesis: Metallic micro-droplet propulsion as a sensitive
                           probe of plasma pressure
             Supervisor: dr. O. Versolato

2016–2018   Master Applied Physics
             Delft University of Technology
             Thesis: Single shot dispersive gate readout of a Sin-
                           glet/Triplet spin state in Si/SiGe
             Supervisor: Prof. dr. ir. L. M. K. Vandersypen

2018–2023   PhD in Physics
             Delft University of Technology
             Thesis: Interacting light fields in monolayer WS_2 and plas-
                           monic systems
             Promotor: Prof. dr. L. Kuipers

LIST OF PUBLICATIONS

6. **M. L. Noordam** and L. Kuipers, *Propagating plasmonic modes in a two-wire system*, In submission

5. **M. L. Noordam**, J. Hernandez-Rueda, and L. Kuipers, *Simultaneous Characterization of Two Ultrashort Optical Pulses at Different Frequencies Using a WS2 Monolayer*, ACS Photonics **9**, 6 (2022)

4. L. Maduro, **M. L. Noordam**, M. Bolhuis, L. Kuipers, and S. Conesa-Boj, *Position-Controlled Fabrication of Vertically Aligned Mo/MoS2 Core–Shell Nanopillar Arrays*, Advanced Functional Materials **32**, 5 (2022)

3. J. Hernandez-Rueda, **M. L. Noordam**, I. Komen, and L. Kuipers, *Nonlinear Optical Response of a WS_2 Monolayer at Room Temperature upon Multicolor Laser Excitation*, ACS Photonics **8**, 2 (2021)

2. **M. L. Noordam**, J. Hernandez-Rueda, L. Y. Talsma and L. Kuipers, *Plasmon-induced enhancement of nonlinear optical processes in a double-resonant metallic nanostructure grating*, Applied Physics Letters **116**, 10 (2020)

1. G. Zheng, N. Samkharadze, **M. L. Noordam**, N. Kalhor D. Brousse, A. Sammak, G. Scappucci, and L. M. K. Vandersypen, *Rapid gate-based spin read-out in silicon using an on-chip resonator*, Nature nanotechnology **14**, 8 (2019).